AB INITIO INVESTIGATIONS OF LOW Z MATERIALS UNDER EXTREME CONDITIONS

BY

RAYMOND CONRAD CLAY, III

DISSERTATION

Submitted in partial fulfillment of the requirements
for the degree of Doctor of Philosophy in Physics
in the Graduate College of the
University of Illinois at Urbana-Champaign, 2016

Urbana, Illinois

Doctoral Committee:

Professor Smitha Vishveshwara, Chair
Professor David M. Ceperley, Director of Research
Professor James N. Eckstein
Professor George D. Gollin

Abstract

Low Z elements, particularly hydrogen and helium, make up the vast majority of matter in the universe. These elements are observed to exist over the widest known ranges of pressures and temperatures, from interstellar plasmas to the cores of stars. In modeling Jovian planets or inertial confinement fusion, the pressures and temperatures of hydrogen and helium can even vary by orders of magnitude within a single system. Thus, understanding these systems requires an accurate phase diagram over a large range of thermodynamic conditions, particularly at high pressures.

Attaining this level of accuracy has been an ongoing challenge for experimentalists and theorists since the phase diagrams of low Z elements exhibit surprising complexity. Experimentally, static compression experiments are frustrated by the high reactivity of lithium and hydrogen, which greatly limits the pressure ranges that can be accurately characterized. Additionally, determining the relevant crystal structures of interesting phases can be very difficult for various reasons. Theoretically, most *ab initio* based methods that can treat bulk systems have to treat electron correlation and nuclear quantum effects approximately. In hydrogen and lithium, the errors introduced by these approximations are comparable to the enthalpy differences between competing phases, giving inaccurate phase boundaries.

We believe that several outstanding questions in low Z phase diagrams can be resolved through a careful and systematic application of *ab initio* methods, particularly quantum Monte Carlo. Quantum Monte Carlo is well suited for the study of high-pressure low Z elements, as it is possible to treat all electrons quantum mechanically and with few uncontrolled approximations. This level of accuracy is suitable not only for direct applications of QMC to problems of interest, but also to benchmark and establish confidence in widely used density functional theory (DFT) calculations.

The purpose of my thesis will be two-fold: to use *ab initio* methods like quantum Monte Carlo to shed light on the phase diagram of bulk low Z elements, and to use these systems as a test bed for new QMC methods which make use of forces. The first part of this thesis will cover the necessary theoretical background, including our work on force and stress estimators. Then we will discuss our QMC based benchmarking method in both hydrogen and helium. The results of these benchmarking studies are then

used in an attempt to resolve some major issues in the phase diagrams of hydrogen and hydrogen-helium mixtures. Lastly, we will present our results for the melting line and solid phase diagram for dense lithium.

To my friends and family.

Acknowledgments

I would not be where I am today without the support of my mentors and collaborators. I would like to first thank my advisor, Dr. Ceperley, not only for his help and guidance in conducting this research, but also for his good-heartedness. While I had a lot of freedom to conduct research, I always felt like I had his support. I also greatly appreciate that he took the time to connect me with some of his active collaborations. From this collaboration, I would like to thank Carlo Pierleoni and Markus Holzmann for their enthusiastic willingness to discuss QMC and electronic structure theory with a graduate student. I would also like to thank the QMCPACK collaboration, especially Jeognim Kim.

I thank my LLNL mentor, Miguel Morales, who oversaw much of the research presented here. I spent hours talking with him about myriads of topics, ranging from pure theory to the nuances of code snippets in the far flung reaches of electronic structure codes. I admire his "jack-of-all-trades" approach to electronic structure theory, which inspired me to greatly broaden my horizons. Beyond research, his frank and honest answers to my questions about life in the national lab environment helped me chart out my desired career path.

I would also like to thank Jeremy McMinis and his family. When I was starting out in Dr. Ceperley's group, Jeremy showed me the ropes of code development and electronic structure calculations. Later, their hospitality and friendship made tough times more navigable.

Lastly, I would like to thank the funding agencies that allowed me to conduct my research. I was supported by the Predictive Theory and Modeling for Materials and Chemical Science program by the Basic Energy Science (BES) by DOE Grant No. DE-NA0001789. I am also indebted to the Lawrence Graduate Scholar Program which in addition to financial support, allowed me the opportunity research at LLNL.

Table of Contents

List of Tables

List of Figures

List of Abbreviations

QMC	Quantum Monte Carlo
VMC	Variational Monte Carlo.
DMC	Diffusion Monte Carlo.
RMC	Reptation Monte Carlo.
p-QMC	Projector quantum Monte Carlo.
QMD	Quantum molecular dynamics.
PIMD	Path-integral molecular dynamics.
DFT	Density functional theory.
CEIMC	Coupled electron-ion Monte Carlo.
RPA	Random phase approximation.
AIRSS	*Ab initio* random structure searching.

List of Symbols

Unless otherwise specified, all quantities and equations are in Hartree atomic units: $\hbar = 1, e = 1, m_e = 1$

a_0	Bohr radius.
N	Total number of particles.
N_e, $N_{\uparrow(\downarrow)}$, N_α	. Number of electrons, number of up(down) electrons, number of ions of species α.
m_e, m_α	Mass of electrons and ions of species α.
$\mathbf{r}$,$\mathbf{r}_i$	$3N_e$ dimensional vector of all electronic coordinates and 3D coordinates of electron i.
$\mathbf{R}$,$\mathbf{R}_i$	$3N$ dimensional vector of all ionic coordinates and 3D coordinates of ion i. The latter will also be used to denote a particular set of ionic coordinates. This will be clear from context.
$\mathbf{F}$,$\mathbf{f}_i$	$3N$ dimensional vector of all ionic forces and the force on ion i.
$S_N^{\alpha\beta}(\mathbf{k})$	Charge-charge structure factor for particle species α and β for a system with N particles.
ρ,ρ_α	Density of particles, and density of type α particles.
Ω	Total volume of system.
k_c, r_c	Magnitude of k-space and r-space cutoffs respectively.
E,H,F,G	Energy, enthalpy, Helmholtz free energy, and Gibbs' free energies.
$\hat{H}$	Hamiltonian operator.
$\hat{L}$	Importance sampled Hamiltonian operator.
$\|\Phi_i\rangle$	Eigenstate i of $\hat{H}$. $i = 0$ is the ground state.
$\|\Psi_T\rangle$	Trial wavefunction.
M	Slater matrix.
ϕ_i	Single particle orbital.

Chapter 1

Introduction

1.1 Motivation

Achieving inertial confinement fusion in a controlled fashion is one of the most exacting scientific challenges of this generation. While the concept of initiating controlled fusion through the implosion of a fuel capsule is easily understood, the achieved gain (ratio of energy produced by fusion to energy expended) depends heavily on the design of the fuel capsule [2]. Materials must be chosen for the casing, the target liner, and fuel source. Then, the geometry of the assembly must be engineered to within micron level precision. Optimizing the design of the fuel capsule requires a detailed understanding of the properties of bulk materials, their interfaces, and how they respond under pressure and temperature gradients that can range over 8 orders of magnitude within the target capsule–all on nanosecond timescales and sub-micron length scales. The current approach to grappling with this extreme multi-scale problem on a theoretical level is to use hydrodynamic models. All relevant physics at the atomic level is included in hydrodynamic models through an equation of state, which expresses the energy of any material in terms of its density and temperature.

As much of the extreme pressure and temperature conditions relevant for this problem are either experimentally inaccessible or difficult to characterize, the burden of constraining the equations of state for these materials has rested on theory. Most theoretical work used to treat these systems relies on various approximations to electronic structure, nuclear quantum effects, and free energies. Unfortunately, the National Ignition Campaign discovered large discrepancies between experiments at the National Ignition Facility (NIF) and currently used models for low Z materials at extreme conditions [3]. It is currently estimated that the difference between the observed and predicted pressures at densities relevant for fusion is as large as a factor of two. This discrepancy needs to be resolved since accurate equations of state are integral in determining whether or not an engineering solution can be attained within current inertial confinement fusion proposals, specifically with Sandia's magnetic liner inertial fusion concept or the polar-drive ignition concept at NIF [4].

Accurate equations of state for low Z materials at extreme conditions are also required by the planetary

physics community. Jovian planets and brown dwarfs are over 90% hydrogen and helium by mass. Temperatures and pressures begin at less than 100K at a near vacuum in the upper atmosphere, but can reach tens of millions of atmospheres and tens of thousands of degrees near the core. To reproduce the measured magnetic field strength, luminosity, gravitational moments, and upper atmosphere composition requires knowing not just what phases exist, but where the phase boundaries are located and the equations of state within each phase to an accuracy of about 1% [5]. For example, small variations in the predicted insulator-to-metal transition in dense hydrogen-helium mixtures can change the estimated size of the conducting region of Jovian planets by hundreds of kilometers [6], which in turn affects the predicted magnetic field strengths and gravitational moments.

1.2 *Ab Initio* Benchmarking

This thesis will primarily focus on understanding and correcting the sources of inaccuracies in *ab initio* equation of state calculations. These errors are rooted in the fact that while equations of state describe matter in the thermodynamic limit, *ab initio* methods almost always treat a finite number of particles. Simulations should therefore be large enough to allow approximations of the thermodynamic limit. Unfortunately, assuming that the non-relativistic Schrödinger equation describes all relevant physics, the computational cost of solving Schrödinger's equation exactly scales exponentially with the number of particles in the system, making simulations of more than a few particles impractical. We then have to employ a sequence of uncontrolled approximations to simulate larger and larger system sizes. For example, imposing the fixed-node approximation in ground state quantum Monte Carlo allows us to move up from exactly solving first-row atoms to simulating systems with upwards of several thousand electrons on modern supercomputers. Treating electronic correlations within mean field approximations like density functional theory allows one to treat systems with well upwards of 10,000 electrons. The unfortunate consequences of these approximations is that they introduce trade-offs between the size of the system we can treat and the accuracy at which we can treat it.

At ambient conditions, researchers have traditionally used experimental data to establish whether or not a certain level of theory is accurate enough for specific quantities of interest. Unfortunately, the experimental data is significantly sparser when we consider materials under extreme conditions, precluding this approach in most cases. In this thesis, we propose that we can still benchmark certain approximate theories, provided we do it self-consistently against more accurate levels of theory. For instance, the errors incurred by approximating electronic correlation effects at the mean field level can be benchmarked against

more expensive but more accurate explicitly correlated methods. This is done by generating large sets of ionic configurations from first principles and establishing reference values using some reference theory. With this test set in hand, we can perform rigorous error quantification of more approximate theories on this test set. We will show that our approach, which we call "*ab initio* benchmarking", can be used to significantly improve the accuracy of equation of state calculations at a much reduced computational cost compared with using either an accurate theory or an approximate theory in isolation.

In this thesis, we will focus primarily on benchmarking density functional theory (DFT) against highly accurate quantum Monte Carlo (QMC) calculations. Density functional theory is the workhorse in equation of state calculations for materials under extreme conditions due to its balance between accuracy and computational cost. We discuss the details of this approximation in Chapter 4. While there are flavors of DFT that have predictive levels of accuracy in some systems, it is very difficult to gauge the accuracy ahead of time. In addition, it is not uncommon for DFT to fail spectacularly in some systems. We discuss later in this chapter known failures of DFT in predicting high-pressure phase transitions in dense hydrogen.

Ground state Quantum Monte Carlo methods are an attractive alternative to DFT in cases where high levels of accuracy are required. We discuss the major flavors of QMC in Chapters 2 and 3. QMC is an explicitly correlated many-body theory that works with the physical Hamiltonian of any given system. Though practical QMC calculations for fermions make use of some uncontrolled approximations, the errors incurred from these approximations have been demonstrated to be extremely small for light elements. With no *a priori* assumptions about the relevant physics, calculation of the bulk modulus of beryllium agrees perfectly with experiment [7], and chemical accuracy can easily be achieved on well known quantum chemistry benchmarks like the G2 test-set [8], a system known for having delicate van der Waals and hydrogen bonding interactions. Since the computational cost scales cubically with the number of particles, it is also one of the only many-body methods able to treat bulk systems.

There are two main reasons why QMC is rarely seen in equation of state calculations. First is the computational cost relative to density functional theory, which is becoming less of a concern as computers become more powerful. Second is that QMC has traditionally not been able to directly estimate forces within a single simulation. This mostly ruled out its application to structure optimization, molecular dynamics, calculation of mechanical response properties, and fitting of classical potentials. To address this point, a major part of this thesis will be the development and deployment of QMC stress and force estimators for use in bulk systems. In Chapter 6, we will present our force and stress estimators, and in Chapter 7, we discuss the finite-size effects associated with these estimators.

1.3 Applications

Most of the remainder of this thesis will focus on the application of *ab initio* benchmarking to outstanding problems in the phase diagrams of low Z materials. We discuss in the following sections the motivations and problems in the phase diagrams of hydrogen and hydrogen-helium mixtures

1.3.1 Hydrogen

Despite its compositional simplicity, hydrogen possesses a surprisingly rich phase diagram [5]. To date, there are five experimentally known solid phases and two liquid phases [9]. Theoretically, an insulator-to-metal transition has been predicted in solid hydrogen [10], which would most likely be a BCS superconductor with a near room temperature T_c [11]. At high enough pressures, it has also been predicted that hydrogen could have a liquid metallic ground state which could also be a superconducting superfluid [12]. For these reasons, there has been intensive theoretical and experimental efforts to accurately map out the phase diagram of hydrogen.

Even now though, there are still significant controversies. Consider the liquid-liquid phase transition (LLPT), separating an insulating phase of liquid H_2 molecules and a metallic (or semimetallic) phase of H atoms. Diamond anvil cell experiments using pulsed laser heating estimate this transition to be near 175GPa at 1000K [13]. However, ramp-compression based shock experiments of deuterium performed on the Z-machine estimate the LLPT to be near 300GPa [14]. For theoretical predictions, *ab initio* methods place this transition to be between 200GPa and 400GPa [15], depending on various approximations to the electronic structure and nuclear quantum effects. The analogous atomic dissociation and insulator-to-metal transitions in solid hydrogen are less controversial experimentally, but only because it is expected that this transition lies beyond experimentally accessible pressures at the moment. Various theoretical predictions place this transition anywhere between 270GPa and 450GPa [16, 1], with the variance again coming from various approximations.

The main question we will concern ourselves with in this work is "by what structural mechanism does solid hydrogen become conducting?" Whether metallization occurs through a band gap closure within a particular molecular or atomic phase, or whether metallization is coincident with a structural phase transition is currently not known with certainty. In order to accurately predict and characterize the insulator-to-metal transition with *ab initio* methods, we need a firm understanding of all the structures hydrogen passes through on its way from the experimentally known phase III to the conducting atomic state. This insight is unlikely to come solely from experiment, as hydrogen's small x-ray scattering cross section precludes a definitive determination of its high-pressure structures.

We will present the result of our benchmarking study in pure hydrogen in Chapter 8. From these results, we present our predictions for the atomic-to-molecular transition in zero temperature hydrogen in Chapter 9.

1.3.2 Hydrogen-Helium Mixtures

Since Jovian planets are mostly hydrogen and helium, we have to consider the phase diagram and properties of hydrogen-helium mixtures. At pressures on the order of 1MBar, a homogeneous mixture of hydrogen and helium are entropically favored provided the temperature is high enough. As one lowers the temperature, however, it is expected that hydrogen and helium will phase separate into helium rich and helium poor regions on energetic grounds [17]. This is the so called "immiscibility transition" in dense hydrogen-helium mixtures. If there were a region of a Jovian planet where hydrogen and helium were immiscible, then as a homogeneous hydrogen-helium mixture was convected from the deep atmosphere to the upper atmosphere, the mixture would phase separate to form helium rich droplets [17, 18]. These droplets would then fall under their own weight to the deeper atmosphere until they reached pressures and temperatures where hydrogen and helium were miscible again. If this mechanism exists, it would modify the planetary model in two major ways. First, increased energy dissipation from the release of latent heat would increase the luminosity of the planet. Secondly, the formation of droplets would dramatically change the mass distribution of the planet–at the very least helium would be somewhat depleted from the upper atmosphere. It is likely that this would also cause depletion of heavier elements which have enhanced solubility in helium–heavier noble gasses for example.

Unfortunately, our knowledge of the phase diagram of hydrogen-helium mixtures is limited. The most recent calculations of the immiscibility transition using DFT based molecular dynamics have demonstrated a sensitivity of the phase diagram to the approximate treatment of the mixing entropy [19, 20]. Calculations of the immiscibility transition using thermodynamic integration exhibit quantitative and qualitative differences to calculations based on the ideal-mixing approximation [19, 21, 20]. In addition to the mixing entropy, the choice of exchange correlation functional and the use of small unit cells introduce unquantified errors. It is not obvious yet how sensitive the phase diagram should be to these effects, but the difficulties already discussed in the pure hydrogen phase diagram suggest that they could be large.

These experimental and theoretical uncertainties have led planetary scientists to treat the equation of state as an optimizable parameter [22] which they can adjust to increase agreement with the data obtained from the Voyager, Galileo, and Cassini probes [23]. Models taking this approach have shown an uncanny ability to accurately predict the gravitational moments, luminosities, and upper atmospheric concentrations

of helium and heavier elements. Unfortunately, this increases the uncertainties in other aspects of the model, such as the core mass and composition. It is our goal in this work to help constrain the equation of state of hydrogen-helium mixtures by quantifying the uncertainties of various approximations used in ab initio calculations, and to look at how these errors affect the phase diagram. We will do this in Chapters 10 and 11.

1.3.3 Dense Lithium

The MagLIF inertial confinement fusion concept has recently been proposed as an alternative to laser based methods [4]. This works by placing deuterium and/or tritium inside a conductive cylinder called a "target liner". By passing a current pulse of between 20-60 MA over a timespan of a few hundred nanoseconds along the axis of the target liner, the liner is forced to implode and compress the fuel via the Lorenz force. Used in conjunction with laser heating of the fuel, it is hoped that pressures and temperatures can be achieved to trigger a self-sustaining fusion reaction. While beryllium has been used in the initial proofs of concept, some have proposed using lithium due to its potentially higher peak implosion velocities [24]. To accurately predict how well this works, an accurate equation of state for lithium from cryogenic fuel loading conditions to pressures of millions of atmospheres is required.

Much like hydrogen, experimental work on lithium at high pressures has produced a rich phase diagram. At ambient conditions and temperatures, lithium is a textbook example of a nearly free electron metal. As pressure is increased, closed packed structures give way to low-coordinated crystal phases [25, 26] and a metal-semiconductor-metal transition [27]. Recent theoretical work has demonstrated that the liquid phase of lithium might demonstrate signatures of the low coordinated solid structures through the formation of long-lived tetrahedral clusters [28]. While this is interesting, the approximations used in this study were comparatively crude–nuclear quantum effects were totally neglected, and the impact of the approximation to the electronic structure was not studied. In this work, we are interested in establishing the robustness of clustering in the liquid phase. Due to the low-coordination phase of the liquid phase, we are also interested in observing how the inclusion of nuclear quantum effects will affect the melting line. Restricting our attention to pressures between 200GPa and 600GPa, we present our investigations into these questions in Chapter 12.

Chapter 2

Variational Monte Carlo

2.1 Introduction

In this chapter, we will present the theory and implementation of variational Monte Carlo (VMC). While rarely used in isolation, wave functions optimized using VMC serve an important role in improving the efficiency projector Quantum Monte Carlo (p-QMC) methods. Additionally, much of the theory and algorithms used in VMC require only slight modifications to be used in p-QMC methods. This chapter will serve as a review of existing methodology.

2.2 The Many-Body Problem

Nearly all material properties within the purview of condensed matter physics and chemistry can be obtained by solving the non-relativistic Schrödinger equation. If greek letters represent different types of particles, then the bare physical Hamiltonian for the system can be written as:

$$\hat{H} = \sum_{\alpha} \sum_{i_\alpha}^{N_\alpha - 1} -\lambda_\alpha \nabla_{i_\alpha}^2 + \sum_{\alpha} \frac{1}{2} \sum_{i_\alpha \neq j_\alpha} \frac{q_\alpha^2}{|\mathbf{r}_{i_\alpha} - \mathbf{r}_{j_\alpha}|^2} + \sum_{\alpha<\beta} \sum_{i_\alpha, j_\beta} \frac{q_\alpha q_\beta}{|\mathbf{r}_{i_\alpha} - \mathbf{r}_{j_\beta}|^2} \tag{2.1}$$

We have chosen Hartree atomic units, which means $m_e = 1$, $q_e = 1$, $\hbar = 1$, and the dielectric constant $k_e = 1$. In the above, $\lambda_\alpha = 1/(2m_\alpha)$, q_α is the charge of species α. While the above expression treats electrons and ions on equal footing, the dramatic mass difference between electrons and ions almost always allows us to use the Born-Oppenheimer approximation to separate the nuclear and electronic degrees of freedom. To this end, let lower case Roman indices denote electrons and upper case ones denote nuclei. Then we define the electronic Hamiltonian as:

$$
\begin{aligned}
\hat{H}_e &= \hat{T}_e + \hat{V}_{ee} + \hat{V}_{eI} + \hat{V}_{II} \\
\hat{T}_e &= \sum_i -\lambda_e \nabla_i^2 \\
\hat{V}_{ee} &= \frac{1}{2} \sum_{i \neq j} \frac{1}{|\hat{\mathbf{r}}_i - \hat{\mathbf{r}}_j|} \\
\hat{V}_{eI} &= \sum_{i,J} v^{eI}(\hat{\mathbf{r}}_i, \mathbf{R}_J) \\
\hat{V}_{II} &= \frac{1}{2} \sum_{I \neq J} \frac{Z_I Z_J}{|\mathbf{R}_I - \mathbf{R}_J|}
\end{aligned}
\tag{2.2}
$$

The solutions of the electron Hamiltonian $\hat{H}_e$ are denoted by

$$
\hat{H}_e |\Phi_i(\mathbf{R})\rangle = E_i(\mathbf{R}) |\Phi_i(\mathbf{R})\rangle \tag{2.3}
$$

Henceforth, we will use $\mathbf{r}$ without indices to denote all $3N_e$ electronic coordinates. The $3N_I$ ionic coordinates $\mathbf{R}$ are treated as parameters that determine the electronic potential. The set of solutions $E_i(\mathbf{R}$ at all accessible ionic positions $\mathbf{R}$ is called the electronic potential energy surface.

The easiest way to state the Born-Oppenheimer approximation is as follows. Provided that there are sizeable gaps in the electronic potential energy surfaces $E_0(\mathbf{R}) << E_1(\mathbf{R}) << \ldots$, and provided that $m_\alpha >> m_e$, then one can write the solutions to the full Hamiltonian $\hat{H}$ as $\Phi(\mathbf{r}, \mathbf{R}) = \Psi_n(\mathbf{R})\Psi_e(\mathbf{r}, \mathbf{R})$. $\Psi_e(\mathbf{r}, \mathbf{R})$ is the electronic wavefunction assuming the ions are fixed at position $\mathbf{R}$. These wavefunctions are calculated from Eq. 2.3. In the event that the ionic coordinates are fixed, we will often suppress the explicit dependence of $\Psi_e(\mathbf{r}, \mathbf{R})$ on $\mathbf{R}$, writing it as $\Psi_e(\mathbf{r})$.

Define $\hat{T}_n = -\sum_\alpha \sum_{i_\alpha}^{N_\alpha - 1} -\lambda_\alpha \nabla_{i_\alpha}^2$, where α denotes the type of ion species. The nuclear contribution to the wavefunction $\Psi_n(\mathbf{R})$ is obtained by solving the following equation:

$$
\left(\hat{T}_n + E_i(\mathbf{R})\right) \chi_j(\mathbf{R}) = E_{i,j} \chi_j(\mathbf{R}) \tag{2.4}
$$

This is just a time-independent Schrödinger equation for ions moving in a potential energy surface defined by solutions to the electronic Hamiltonian. The $\chi_j(\mathbf{R})$ wavefunctions depend only on the ionic coordinates. $E_{i,j}$ is the total energy of the system with ions in state j and electrons in state i.

It should be noted that the constraint that the gap be large between electronic states is not a necessary condition on the validity of the Born-Oppenheimer approximation: the approximation also works well in

some metallic systems. Ultimately, it's a question of whether matrix elements like $\frac{1}{m_\alpha}\langle\Phi_i(\mathbf{R})|\nabla_{i_\alpha}^2|\Phi_j(\mathbf{R})\rangle$ are small in a perturbative sense that determines the validity of the Born-Oppenheimer approximation.

We will be concerned with how to calculate expectation values over various wave functions. Let $|\Psi_T\rangle$ be an arbitrary wave function. We define the expectation value of any *local* operator $\hat{\mathcal{A}}$ in the state $|\Psi_T\rangle$ as:

$$\left\langle \hat{\mathcal{A}} \right\rangle_{\Psi_T} = \frac{\langle\Psi_T|\hat{\mathcal{A}}|\Psi_T\rangle}{\langle\Psi_T|\Psi_T\rangle} = \frac{\int d\mathbf{r}\Psi_T^*(\mathbf{r})\hat{\mathcal{A}}\Psi_T(\mathbf{r})}{\int d\mathbf{r}\Psi_T^*(\mathbf{r})\Psi_T(\mathbf{r})} \tag{2.5}$$

A slight generalization of the above is needed for non-local operators (e.g. the single-particle density matrix, nonlocal pseudopotential energy, etc). We can construct a local operator which is diagonal in position space by:

$$\hat{\mathcal{A}}_L = \mathcal{A}_L(\hat{\mathbf{r}}) = \frac{\hat{\mathcal{A}}\Psi_T(\mathbf{r})}{\Psi_T(\mathbf{r})} \tag{2.6}$$

In the special case that $\hat{\mathcal{A}} = \hat{H}_e$, the resulting operator $E_L(\mathbf{r})$ is referred to as the "local energy".

2.3 Variational Theorem

Since we cannot hope to solve Schrödinger's equation exactly for more than a few particles, we instead seek to construct approximate solutions which hopefully capture all physics we need. A strong guiding principle for constructing approximations is the Variational Theorem. This states that for an arbitrary wave function $|\Psi_T\rangle$,

$$E_0 \leq \left\langle \hat{H} \right\rangle_{\Psi_T} = \langle E_L \rangle_{\Psi_T} \tag{2.7}$$

Equality will hold in the event that $|\Psi_T\rangle$ is the ground state wave function $|\Phi_0\rangle$. A similar condition exists for the variance of the energy:

$$\sigma_{E_L}^2 = \left\langle E_L^2 \right\rangle_{\Psi_T} - \langle E_L \rangle_{\Psi_T}^2 \geq 0 \tag{2.8}$$

Strict equality will hold if $|\Psi_T\rangle$ is an eigenstate of $\hat{H}_e$.

The variational theorem immediately suggests a practical algorithm for approximately solving Schrödinger's equation. We choose a family of wave functions $|\Psi_T(\mathbf{c})\rangle$ parameterized by a list of variables $\mathbf{c} = \{c_0, c_1, \ldots\}$. Then we minimize Eq. 2.7 with respect to $\mathbf{c}$ to produce the "best" guess for the ground-state wave function within this family of wave functions. While this will not usually give us exact ground-state energies or properties, it will provide a strict upper bound on the ground-state energy. Additionally, improvements to the trial wave function ansatz can be immediately assessed based on whether or not they lower the energy

and variance.

2.4 Trial Wave functions

2.4.1 Slater-Determinant

One of the simplest wave function ansatzes we can make for fermionic wave functions is the Slater determinant. Considering N_α indistinguishable fermions of species α, one starts with a set of M_α single particle functions $\{\phi_{0_\alpha}, \phi_{1_\alpha}, \ldots, \phi_{M_\alpha}\}$, known as "single particle orbitals". These orbitals are occupied by the fermions with real particle coordinates given by $\{\mathbf{r}_{0_\alpha}, \ldots, \mathbf{r}_{N_\alpha - 1}\}$. Defining the $N_\alpha \times N_\alpha$ Slater matrix as $M^\alpha_{ij} = \phi^\alpha_j(\mathbf{r}_{i_\alpha})$, the Slater determinant wave function is $D^\alpha(\mathbf{r}_{0_\alpha}, \ldots, \mathbf{r}_{N_\alpha - 1}) = \det(M_\alpha)$. The Slater determinant is generalized to multiple species of fermions by a simple product: $D = \prod_{\alpha=0}^{N_s} D^\alpha(\mathbf{r}_{0_\alpha}, \ldots, \mathbf{r}_{N_\alpha - 1}) = \det(M^\alpha)$.

The variational theorem is used here by introducing variational parameters into the single particle orbitals, usually by introducing a basis such that $\phi^\alpha_j(\mathbf{r}) = \sum_{i=0}^{N_b - 1} c^\alpha_{ij} \xi_i(\mathbf{r})$. Upon explicitly minimizing the variational energy with respect to $\mathbf{c}$ subject to an orthonormality constraint, one recovers Hartree-Fock theory. In general, the true ground-state energy will be somewhat lower than the Hartree-Fock energy. This difference $E_0 - E_{HF}$ is commonly referred to as the "correlation energy".

2.4.2 Slater-Jastrow

One of the simplest modifications we can make to the Slater determinant is the following:

$$\Psi_T(\mathbf{r}) = De^{-J(\mathbf{r},\mathbf{R})} \tag{2.9}$$

The scalar function $J(\mathbf{r}, \mathbf{R})$ is known as the Jastrow factor, and has the following form:

$$J(\mathbf{r}, \mathbf{R}) = \sum_{\alpha,\beta} \sum_{i_\alpha, I_\beta} u^{\alpha\beta}_{1-bdy}(|\mathbf{r}_{i_\alpha} - \mathbf{R}_{I_\beta}|) + \sum_{\alpha,\beta} \sum_{i_\alpha, j_\beta} u^{\alpha\beta}_{2-bdy}(|\mathbf{r}_{i_\alpha} - \mathbf{r}_{j_\beta}|) + \ldots \tag{2.10}$$

One advantage of using Jastrow factors is that the true many-body wave function posesses certain analytic properties which we can use a Jastrow to enforce. Since $E_L(\mathbf{r})$ is a constant function if $\Psi_T(\mathbf{r})$ is an eigenfunction of $\hat{H}$, we know that the divergences from the coulomb terms as $\mathbf{r}_i \to \mathbf{r}_j$ and $\mathbf{r}_i \to \mathbf{R}_J$ must be exactly cancelled by the kinetic energy term. This happens if there is a cusp in the wave function near these coincident points. The "Kato cusp conditions" for the electron-ion, like-spin electron, and unlike-spin

electron are given respectively by [29]:

$$\begin{aligned}\frac{1}{\Psi_T}\frac{\partial \Psi_T}{\partial r_{iJ}} &= -q_J \\ \frac{1}{\Psi_T}\frac{\partial \Psi_T}{\partial r_{ij}^{\uparrow\uparrow}} &= \frac{1}{4} \\ \frac{1}{\Psi_T}\frac{\partial \Psi_T}{\partial r_{ij}^{\uparrow\downarrow}} &= \frac{1}{2}\end{aligned} \tag{2.11}$$

While possible to include the electron-ion cusp in the single-particle orbitals [30, 29], often times it is more convenient to let the one-body Jastrow $u_{1-bdy}(r)$ enforce this condition. In contrast, the electron-electron cusp conditions cannot be enforced at the Slater-determinant level, making the use of $u_{2-bdy}^{\alpha\beta}(r)$ the easiest way to enforce these conditions.

The other key advantage of Jastrows is their ability to include electron-electron correlations. Even with simple functional forms for $u_{2-bdy}^{\alpha\beta}(r)$, Slater-Jastrow wave functions are routinely able to capture in excess of 90% of the correlation energy missed by the Slater-Determinant. Even more correlation energy can be recovered by including higher-order terms to the Jastrow; three-body terms are not unusual.

2.4.3 Backflow

While we can add progressively higher order Jastrow terms to better describe the "electron-electron" correlation, a different approach is inspired by Fermi liquid theory. Fermi liquid theory was constructed to account for the unreasonable success of independent particle approximations for alkali metals. One of the main conclusions of this theory is that independent particle approximations work in many correlated electronic systems as long as the independent particles are no longer bare electrons. Instead, many-body correlation effects such as screening will dress the bare electrons resulting in "quasiparticles" [31].

One can show for the homogeneous electron gas that we can introduce leading order quasiparticle effects into the Slater-Jastrow type wave function by doing the following [32, 33]. Instead of evaluating the Slater matrix as $M_{ij} = \phi_j(\mathbf{r}_i)$, we evaluate it at new quasiparticle coordinates as $M_{ij} = \phi_j(\mathbf{q}_i)$, where $\mathbf{q}$ is defined as:

$$\mathbf{q}_{i_\alpha} = \mathbf{r}_{i_\alpha} + \sum_{\alpha \leq \beta} \sum_{i_\alpha \neq j_\beta} \eta^{\alpha\beta}(|\mathbf{r}_{i_\alpha} - \mathbf{r}_{j_\beta}|)(\mathbf{r}_{i_\alpha} - \mathbf{r}_{j_\beta}) \tag{2.12}$$

In practical applications, we treat $\eta^{\alpha\beta}(r)$ as a short-ranged optimizable spherically symmetric function, with separately optimizable terms for same spin, opposite spin, and electron-ion effects. Notice that in contrast to the Jastrow term, backflow will modify the antisymmetric contribution to the wave function.

2.4.4 Multideterminants

In addition to backflow, we can imagine improving the antisymmetric part of our trial wave function through use of a linear combination of determinants, known as a "multideterminant" wave function. If one appends a Jastrow factor onto the multideterminant, one has the multi-Slater-Jastrow form given below:

$$\Psi_T(\mathbf{r}) = e^{-J(\mathbf{r},\mathbf{R})} \sum_{k=0}^{N_{det}-1} c_k D_k^{\uparrow} D_k^{\downarrow} \tag{2.13}$$

The invention of fast-evaluation algorithms for calculating large multideterminant expansions has greatly increased their use in QMC calculations [34]. This is fortunate, as multideterminant wave functions offer several advantages over Slater-Jastrow or backflow wave functions. In multireference systems, such as the carbon dimer or nearly any diatomic molecule that has been pulled apart, the ground-state wave function is easily shown to be a sum of several determinants. Forging ahead with a single Slater-Jastrow ansatz risks incorrectly describing the antisymmetric part of the wave function in such cases. As backflow most generally provides a perturbative correction to the antisymmetric part of the trial wave function, it is doubtful that backflow alone is sufficient to describe this type of static correlation. Another major advantage of multideterminant wave functions is that many post Hartree-Fock methods like full and truncated configuration interaction are based on determinantal expansions [35], allowing us to use quantum chemistry methods to generate intelligent guesses for these wave functions.

2.5 Metropolis Monte Carlo

We've discussed the commonly used types of wave function ansatzes used in QMC and some quantum chemistry methods. The question is now a practical one: how do we evaluate expectation values over a trial wave function $|\Psi_T(\mathbf{c})\rangle$? This is important not only for understanding a system's properties, but is a crucial step in optimizing $\mathbf{c}$. For simple wave function ansatzes, like the Slater or multideterminant wave functions (without Jastrows), certain analytic tricks allow for rapid evaluation. Two-body integrals over multi-Slater determinants performed in $O(N^{det}N^4)$ time with the number of determinants N^{det} and particles N. The inclusion of a Jastrow or backflow transformation eliminates these tricks, forcing us to attack the general problem of performing $3N$ dimensional integrals like those found in Eq. 2.5.

Let X be a D-dimensional generalized set of coordinates: e.g., 3N particle positions, bond angles, etc. Consider numerically evaluating the integral $I = \int_\Omega dX f(X)$ to within some error ϵ. The most direct method to compute this integral is through numerical quadratures, whereby space is discretized by establishing a grid on each dimension. If the computer time is proportional to the number of function evaluations required,

second-order quadrature formulas like Simpson's rule have the computer time scale like $\epsilon^{-D/2}$ [36].

An alternative approach to evaluating I is through statistical sampling. Consider a positive function $\Pi(X)$, and let $\mathcal{Z} = \int_\Omega dX \Pi(X)$. By rewriting the integral as $I = \int dX \frac{\Pi(X)}{\mathcal{Z}} \left(f(X) \frac{\mathcal{Z}}{\Pi(X)} \right)$, we recognize that I can be interpreted as an average over a probability distribution $\Pi(X)/\mathcal{Z}$: $I = \left\langle f \frac{\mathcal{Z}}{\Pi} \right\rangle_{\Pi/\mathcal{Z}}$. Assuming the central limit theorem holds, I is estimated by generating N samples $X_0, X_1, \ldots, X_N$ distributed according to $\Pi(X)/\mathcal{Z}$ and then using the formula $I = \frac{1}{N} \sum_{i=0}^{N} f(X_i) \frac{\mathcal{Z}}{\Pi(X_i)} + \epsilon$. The statistical error ϵ on this estimate is of order $N^{-1/2}$ with the number of function evaluations, which implies that the computer time scales like ϵ^{-2} with the statistical approach. Due to its lack of dependence on the dimensionality of the problem, statistical sampling integrals rapidly becomes the most efficient way to calculate integrals above approximately four dimensions.

The problem with this general approach is that that while $\Pi(X)$ might be easily evaluated in real applications, calculating the normalization $\mathcal{Z}$ is tantamount to solving the integral we are trying to evaluate. Fortunately, this problem is largely circumvented for quantum and thermodynamic expectation values like Eq. 2.5 since the normalization factor cancels. In such cases, we can use the Metropolis Monte Carlo method to generate a sequence of samples $S = \{X_0, X_1, \ldots, X_N\}$ via a random walk distributed according to the probability distribution associated with $\Pi(X)$.

The random walk is generated by a specially constructed time-homogeneous ergodic Markov chain [37]. Unpacking the terminology, if the probability of generating a configuration X given a previous sequence of configurations S is $T(x_{N+1} = X | x_1 = X_1, x_2 = X_2, \ldots, x_N = X_N)$, then a process is said to be Markovian if $T(x_{N+1} = X | x_1 = X_1, x_2 = X_2, \ldots, x_N = X_N) = T(x_{N+1} = X | x_N = X_N)$. The probability of choosing a new state X depends only on the previous state X_N. The Markov chain is time-homogeneous if there is no dependence of T on the step number, so $T(x_{N+1} = X | x_N = X_N) = T(X_N \to X)$. Ergodicity is hard to explain succinctly without special terminology, but amounts to saying that for any state X_i, the probability of being able to access any other state X_j is nonzero for random walks of arbitrarily long lengths.

In discrete spaces, time-homogeneous ergodic Markov chains possess two highly desirable properties for our purposes. First, they possess a unique limiting distribution $\Pi(X)$ such that, if $T^{(n)}(X_i \to X_j)$ denotes the probability of a transition from X_i to X_j in n steps, and $\Pi'(X)$ is an arbitrary probability distribution, then:

$$\Pi(X_j) = \lim_{n \to \infty} \sum_i T^{(n)}(X_i \to X_j) \Pi'(X_i) \tag{2.14}$$

This means that we can start with an initial sample X_i, and after applying the transition matrix enough times, subsequent samples will be distributed according to $\Pi(X)$. No less importantly, these types of Markov chains exhibit a stationary state-property, such that if we start off with states distributed according to $\Pi(X)$

and act with the transition matrix, we will continue to sample $\Pi(X)$:

$$\Pi(X_j) = \sum_i T(X_i \to X_j)\Pi(X_i) \tag{2.15}$$

The choice of the transition matrix made by Metropolis was to split it into two components $T(X_i \to X_j) = R(X_i \to X_j)A(X_i \to X_j)$. $R(X_i \to X_j)$ is an *a priori* probability for updating the state from $X_i \to X_j$: randomly flipping a spin in a lattice, randomly displacing a particle in a box, etc. $A(X_i \to X_j)$ is the probability of accepting or rejecting the move we just proposed. This is done by choosing $A(X_i \to X_j)$ such that the detailed balance condition is satisfied:

$$R(X_i \to X_j)A(X_i \to X_j)\Pi(X_i) = R(X_j \to X_i)A(X_j \to X_i)\Pi(X_j) \tag{2.16}$$

The reader will verify that a solution to this equation is given by choosing $A(X_i \to X_j)$ to be:

$$A(X_i \to X_j) = \min\left(1.0, \frac{R(X_j \to X_i)}{R(X_i \to X_j)}\frac{\Pi(X_j)}{\Pi(X_i)}\right) \tag{2.17}$$

Note that while not a necessary condition, any transition matrix that satisfies Eq. 2.16 will automatically satisfy Eq. 2.15. We will see examples of trial moves which do not satisfy the detailed balance condition later.

2.6 Wave Function Evaluation and Optimization

Let us now focus on how Metropolis Monte Carlo is used in VMC. We begin the simulation by initializing a $3N_e$ dimensional random vector for the electron coordinates $\mathbf{r}(\beta = 0)$. Here, β is the simulation time, and τ is a "time step". To advance the simulation by a single time step, we propose a trial move $\mathbf{r}(\beta) \to \mathbf{r}'$ with probability $R(\mathbf{r} \to \mathbf{r}')$. We then accept this proposed move with probability $A(\mathbf{r} \to \mathbf{r}')$. If accepted, $\mathbf{r}(\beta + \tau) = \mathbf{r}'$, and if not, $\mathbf{r}(\beta + \tau) = \mathbf{r}(\beta)$. The vector $\mathbf{r}(\beta)$ is often called a "walker" in QMC parlance, and its entire trajectory in simulation time β is the random walk. After some equilibration time β_w, the walker trajectory $\{\mathbf{r}(\beta_w), \mathbf{r}(\beta_w + \tau), \mathbf{r}(\beta + 2\tau), \ldots\}$ will be distributed according to $|\Psi_T(\mathbf{r})|^2$.

2.6.1 Trial Moves

The simplest class of trial moves are all-electron moves, whereby one proposes a transition from $\mathbf{r} \to \mathbf{r}'$. One popular type of trial move is $\mathbf{r}' = \mathbf{r} + \boldsymbol{\chi}$, where $\boldsymbol{\chi}$ is a $3N_e$ dimensional vector drawn from a Gaussian

distribution:

$$R(\mathbf{r} \to \mathbf{r}') = \frac{1}{(2\sigma^2\pi)^{3N/2}} \exp\left(-\frac{(\mathbf{r}' - \mathbf{r})^2}{2\sigma^2}\right) \tag{2.18}$$

For now, the variance of the Gaussian distribution σ^2 is a free parameter which is adjusted to optimize the diffusion of the walker $\left\langle (\mathbf{r}(\beta) - \mathbf{r}(0))^2 \right\rangle$. Since $R(\mathbf{r} \to \mathbf{r}')$ is symmetric in $\mathbf{r}$ and $\mathbf{r}'$, the acceptance probability for this trial move is given by $A(\mathbf{R} \to \mathbf{R}') = \min\left(1.0, |\Psi_T(\mathbf{r}')|^2/|\Psi_T(\mathbf{r})|^2\right)$. The computational cost for a Slater-Jastrow wave function scales like $O(N^3)$ in the number of particles. This stems from the necessity of calculating calculating a determinant.

The difficulty with all-electron moves is that as the system size increases, the odds of accepting an all-electron move drops exponentially with system size. We can remedy this by performing single-particle moves. To do this, consider a particle i. We propose a move $\mathbf{r}_i' = \mathbf{r}_i + \boldsymbol{\chi}_i$ with transition probability:

$$R((\mathbf{r_0}, \ldots, \mathbf{r}_i, \ldots, \mathbf{r}_N) \to (\mathbf{r_0}, \ldots, \mathbf{r}_i', \ldots, \mathbf{r}_N)) = \frac{1}{(2\sigma^2\pi)^{3/2}} \exp\left(-\frac{(\mathbf{r}_i' - \mathbf{r}_i)^2}{2\sigma^2}\right) \tag{2.19}$$

This move is then accepted or rejected with the same transition probability as given for the all-electron moves. Assuming that each single-particle move independently maintains detailed balance, the process of generating a new all-electron configuration $\mathbf{r}$ by sequentially applying N single-particle moves will also maintain detailed balance. With low-rank determinant updates, calculating the acceptance probability for each single particle move only costs $O(N^2)$ time, amounting to $O(N^3)$ time for generating new N particle configurations. While this scales equivalently to the all-electron moves, efficiency is usually greatly improved by the higher acceptance ratios with this method.

2.6.2 Optimization

The presence of statistical noise for observables in variational Monte Carlo provides a unique challenge for wave function optimization. Fortunately, the linear method of Umrigar and coworkers has proven to be a reasonably efficient and robust algorithm for energy minimization in VMC [38, 39]. Let $|\Psi_0\rangle = |\Psi_T(\mathbf{c})\rangle$ and $|\Psi_i\rangle = \frac{\partial}{\partial c_i}|\Psi_T(\mathbf{c})\rangle$ for $i \geq 1$. Assume for pedagogical purposes that all wave functions and derivatives are normalized. The wave function is then expanded in this subspace:

$$|\Psi_T(\mathbf{c})\rangle = |\Psi_0\rangle + \sum_{i=1}^{N_{param}} \delta c_i |\Psi_i\rangle \tag{2.20}$$

The $\delta\mathbf{c}$ corresponding the lowest energy wave function $|\Psi\rangle$ is obtained by diagonalizing the Hamiltonian in this subspace. Defining the Hamiltonian and overlap matrices in this basis as $H_{ij} = \langle\Psi_i|\hat{H}|\Psi_j\rangle$ and

$S_{ij} = \langle \Psi_i | \Psi_j \rangle$ respectively, one just has to find the lowest eigenvalue solution to the following equation.

$$\mathbf{H} \cdot \delta\mathbf{c} = E\mathbf{S} \cdot \delta\mathbf{c} \tag{2.21}$$

At each step, VMC is used to evaluate the matrix elements of $\mathbf{H}$ and $\mathbf{S}$. The $\delta\mathbf{c}$ is used to update the parameters $\mathbf{c}$ in $|\Psi_T(\mathbf{c})\rangle$, and the process is iterated until $\delta\mathbf{c} = 0$.

To improve the stability of this procedure, some modifications to the above method were made for practical calculations. Instead of minimizing the trial energy $\langle E_L \rangle_{\Psi_T(\mathbf{c})}$, one minimizes a cost function defined as $C = x \langle E_L \rangle_{\Psi_T(\mathbf{c})} + (1-x)\sigma^2_{E_L}$, which is a mixture of variance and energy. Since the trial energy is estimated on a finite sample, a new wave function $|\Psi_T(\mathbf{c} + \delta\mathbf{c})\rangle$ can sometimes produce a lower estimate trial energy than $|\Psi_T(\mathbf{c})\rangle$, but only because the variance of the estimate is massive. Mixing a little bit of variance into the cost function helps avoid bad optimization steps to wave functions like these. The linear method is still used as described to calculate $\delta\mathbf{c}$, but the resulting vector is then used to minimize C via a line search [40].

Chapter 3

Projector Monte Carlo

3.1 Introduction

Projector quantum Monte Carlo (p-QMC) methods are among the most accurate electronic structure methods available. Instead of sampling a guess for the ground state wave function like in VMC, these methods project out and sample the ground state wave function. For bosonic systems, these methods are exact with a computational cost that scales polynomially with the system size. While one can still in principle project out the exact ground state for fermionic systems, the method will in general scale exponentially with the number of particles, forcing us to introduce an uncontrolled approximation.

In this chapter, we provide a summary of p-QMC methods. We will discuss how projectors work and present the "importance sampled Schrödinger equation" on which all practical p-QMC methods are based. We then present how two major ground state p-QMC methods, diffusion Monte Carlo and reptation Monte Carlo, work on a practical level. During my thesis research, we implemented and tested several improvements to both the propagator and trial moves used in reptation Monte Carlo. We present our findings at the end of the RMC section. All subsequent RMC calculations in this thesis will use the improved RMC algorithm discussed in tihs section. Lastly, we conclude by presenting the fermion sign problem and our use of the fixed-node approximation in practical p-QMC simulations.

3.2 Projector Methods

Consider the time-dependent Schrödinger's equation:

$$i\frac{\partial \Psi}{\partial t} = \hat{H}\Psi \tag{3.1}$$

The operator solution to this equation is the given by the Green's function or "propagator": $\hat{G}(t) = \exp\left(it\hat{H}\right)$. The propagator is important since the time evolution of any initially prepared state $|\Psi_T(t=0)\rangle$ can be obtained by $|\Psi_T(t)\rangle = \hat{G}(t)|\Psi_T(t=0)\rangle$. Henceforth, the term in parenthesis in $|\Psi_T(t)\rangle$ will always

denote a time index. If instead we now consider the "imaginary time" Schrödinger equation, obtained by letting $\beta = it$, we find the Green's function to be $\hat{G}(\beta) = \exp\left(-\beta\hat{H}\right)$. This operator is called a "projector" for the following reason. If $\{|\Phi_0\rangle, |\Phi_1\rangle, \ldots\}$ are the eigenfunctions of $\hat{H}$ with eigenvalues $\{E_0, E_1, \ldots\}$, any initially prepared state $|\Psi_T(0)\rangle$ can be expanded in these functions: $|\Psi_T(0)\rangle = \sum_{i=0}^{\infty} c_i|\Phi_i\rangle$. This state evolves in imaginary time as $|\Psi_T(\beta)\rangle = \sum_{i=0}^{\infty} c_i e^{-\beta E_i}|\Phi_i\rangle$. Assuming $|\Psi_T(0)\rangle$ has non-zero overlap with the ground state $|\Phi_0\rangle$, which we will assume is non-degenerate at the moment,

$$\lim_{\beta\to\infty} \hat{G}(\beta)|\Psi(0)\rangle = c_0 e^{-\beta E_0}|\Phi_0\rangle \propto |\Phi_0\rangle \tag{3.2}$$

Thus, applying the projector to $|\Psi_T(0)\rangle$ for long enough imaginary times will yield the ground state wave function. Projector quantum Monte Carlo (p-QMC) methods exploit this property by stochastically simulating the action of $\hat{G}(\beta)$. This allows us to sample the ground state wave function and calculate expectation values within the Metropolis Monte Carlo framework.

3.3 Importance Sampled Schrödinger Equation

For computational reasons, it is more convenient to work with the "importance sampled" Schrödinger equation [29, 41, 42]. Let $f(\mathbf{r}, \beta) = \Psi_T(\mathbf{r})\Phi(\mathbf{r}, \beta)$. Multiplying both sides of Schrödinger's equation by $\Psi_T(\mathbf{r})$ yields the following equation after some algebra:

$$\begin{aligned} \frac{\partial f}{\partial \tau} &= \hat{L} f(\mathbf{r}, \beta) \\ &= \left[\lambda_e \nabla \cdot (\nabla - \mathbf{F}(\mathbf{r})) - (E_L(\mathbf{r}) - E_T)\right] f(\mathbf{r}, \beta) \end{aligned} \tag{3.3}$$

$\mathbf{F}$ is the "wave function force", defined as $\mathbf{F} = 2\nabla \log \Psi_T$. E_T is an arbitrary constant added to the Hamiltonian, called the "trial energy".

If $f(\mathbf{r}, \beta) \geq 0$, then we can interpret it as a probability distribution. This allows us to make formal correspondences between the importance sampled Schrödinger equation and other well studied equations in statistical mechanics. The gradient terms in Eq. 3.3 are recognized as the Smoluchowski equation, which governs the evolution of a probability distribution describing Brownian particles in a forcefield. The energy terms are recognized as a spatially dependent rate equation.

We can solve for the Green's function $\hat{\tilde{G}}(\tau)$ of Eq. 3.3 approximately for short times τ. Solving the drift/diffusion equations and rate equations independently in the short-time limits, one uses the symmetrical Trotter formula $\exp(\tau(\hat{A} + \hat{B})) = \exp(\frac{\tau}{2}\hat{B})\exp(\tau\hat{A})\exp(\frac{\tau}{2}\hat{B}) + O(\tau^2)$ to stitch these independent solutions

together into an approximate solution for the importance sampled Green's function:

$$\tilde{G}(\mathbf{r},\mathbf{r}',\tau) = \langle \mathbf{r}|\hat{\tilde{G}}(\tau)|\mathbf{r}'\rangle = G_{DD}(\mathbf{r},\mathbf{r}',\tau)G_B(\mathbf{r},\mathbf{r}',\tau) + O(\tau^2) \tag{3.4}$$

$G_{DD}(\mathbf{r},\mathbf{r}',\tau)$ is the Green's function for the drift/diffusion operator $\lambda_e \nabla \cdot (\nabla - \mathbf{F}(\mathbf{r}))$. Assuming that $\mathbf{F}(\mathbf{r})$ is slowly varying, its solution is given by:

$$\tilde{G}_{DD}(\mathbf{r},\mathbf{r}',\tau) = \frac{1}{(4\pi\lambda\tau)^{3N/2}} \exp\left(-\frac{(\mathbf{r}' - \mathbf{r} - 2\lambda\tau\mathbf{F}(\mathbf{r}))^2}{4\lambda\tau}\right) \tag{3.5}$$

The Green's function for the local energy operator is:

$$\tilde{G}_B(\mathbf{r},\mathbf{r}',\tau) = P_0 \exp\left(-\frac{1}{2}(E_L(\mathbf{r}) + E_L(\mathbf{r}') - 2E_T)\tau\right) \tag{3.6}$$

The importance sampled Green's function at arbitrary times $\hat{\tilde{G}}(\beta)$ can then be obtained from a product of short-time Green's functions: $\hat{\tilde{G}}(\beta) = [\hat{\tilde{G}}(\tau)]^n$, where $\beta = n\tau$. The error in this approximation is $O(\tau)$, but can be reduced arbitrarily by increasing n and decreasing τ.

Once we have the importance sampled Green's function, we can recover the original projector to Schrödinger's equation with the following transformation:

$$G(\mathbf{r},\mathbf{r}',\beta) = \frac{1}{\Psi_T(\mathbf{r}')}\tilde{G}(\mathbf{r},\mathbf{r}',\beta)\Psi_T(\mathbf{r}) \tag{3.7}$$

3.4 Mixed Estimator Problem

One of the major disadvantages of the importance sampled Schrödinger equation is that sampling is done over the "mixed distribution" $f(\mathbf{r}) = \Psi_T(\mathbf{r})\Phi_0(\mathbf{r})$, and not the "pure distribution" $|\Phi_0(\mathbf{r})|^2$. Let $\hat{\mathcal{A}}$ be an operator that commutes with the Hamiltonian $\hat{H}$, and let $\{a_0, a_1, \ldots\}$ be its spectrum of eigenvalues. Expectation values of these types of operators can be evaluated without bias over the "mixed distribution" $f(\mathbf{r})$:

$$\left\langle \hat{\mathcal{A}} \right\rangle_f = \frac{\langle \Psi_T|\hat{\mathcal{A}}|\Phi_0\rangle}{\langle \Psi_T|\Phi_0\rangle} = \frac{\langle \Psi_T|\Phi_0\rangle}{\langle \Psi_T|\Phi_0\rangle} a_0 = a_0 \tag{3.8}$$

If an operator $\hat{\mathcal{B}}$ does not commute with the Hamiltonian, a bias will be introduced. Let $|\Psi_T\rangle = |\Phi_0\rangle + \delta|\delta\Phi_0\rangle$. The error incurred by sampling over the mixed distribution can be shown to be (to leading

order in δ):

$$\left\langle \hat{\mathcal{B}} \right\rangle_f - \left\langle \hat{\mathcal{B}} \right\rangle_{|\Phi_0|^2} = \delta \frac{\langle \delta\Phi_0 | \hat{\mathcal{B}} - \left\langle \hat{\mathcal{B}} \right\rangle_{|\Phi_0|^2} | \Phi_0 \rangle}{\langle \Phi_0 | \Phi_0 \rangle} \tag{3.9}$$

While it would be preferable to evaluate expectation values over the pure distribution, this requires some additional machinery which will be discussed later in this chapter. The easiest way to reduce the mixed-estimator error using quantities already on hand is by constructing an extrapolated estimate: $\left\langle \hat{\mathcal{B}} \right\rangle_{ext} = 2\left\langle \hat{\mathcal{B}} \right\rangle_f - \left\langle \hat{\mathcal{B}} \right\rangle_{|\Psi_T|^2}$. The quantity $\left\langle \hat{\mathcal{B}} \right\rangle_{|\Psi_T|^2}$ is recognized as the VMC expectation value. One can show that the error of this estimate scales like $O(\delta^2)$ in the quality of the trial wave function. While not exact, we will find this extrapolation scheme to be more than adequate for many applications.

3.5 Diffusion Monte Carlo

Diffusion Monte Carlo works by stochastically simulating the imaginary-time evolution of an initially prepared state $f(\mathbf{r}, 0) = |\Psi_T(\mathbf{r})|^2$. This is done by exploiting the mathematical correspondence between Fokker-Planck equations for the evolution of probability distributions and Langevin equations describing the stochastic evolution of particle trajectories [29, 43, 41, 44, 42]. To shift to a Langevin picture, we represent an initial state $f(\mathbf{r}, 0)$ by an ensemble of N_w walkers $\{\mathbf{r}_0(0), \mathbf{r}_1(0), \ldots, \mathbf{r}_{N_w}(0)\}$ distributed according to $f(\mathbf{r}, 0)$. Assume each walker also has an associated weight $w_i(\beta)$ where $w_i(0) = 1.0$. We consider the action of the short-time Green's function $\tilde{G}(\mathbf{r}, \mathbf{r}', \tau)$ on this distribution.

The action of the drift-diffusion propagator can be simulated with a stochastic drift-diffusion step, given by:

$$\mathbf{r}(\beta + \tau) = \mathbf{r}(\beta) + 2\lambda\tau\mathbf{F}(\mathbf{r}(\beta)) + \sqrt{2\lambda\tau}\boldsymbol{\xi} \tag{3.10}$$

Here, $\boldsymbol{\xi}$ is a $3N_e$ dimensional Gaussian random vector with unit variance. Once a new position is generated, the $G_B(\mathbf{r}, \mathbf{r}', \tau)$ contribution is dealt with by updating the walker weight $w_i(\beta)$ with the following formula:

$$w(\beta + \tau) = w(\beta) G_B(\mathbf{r}(\beta), \mathbf{r}(\beta + \tau), \tau) \tag{3.11}$$

Expectation values of local observables $\mathcal{A}(\mathbf{r})$ over the distribution $f(\mathbf{r}, \beta)$ are obtained by a weighted average:

$$\langle \mathcal{A} \rangle_f (\beta) = \frac{\sum_{i=0}^{N_w - 1} w_i(\beta) \mathcal{A}(\mathbf{r_i}(\beta))}{\sum_{i=0}^{N_w - 1} w_i(\beta)} \tag{3.12}$$

Implementing everything discussed up to this point results in "pure diffusion" Monte Carlo [45]. However, due to the exponential growth/decay of the walker weights with β, the efficiency of this method decays

exponentially with the projection time. "Branching" diffusion Monte Carlo circumvents this problem by implementing Eq. 3.11 stochastically through the replication/killing of walkers [44]. For each walker i, M_i copies of the walker are made after the drift/diffusion step according to the formula $M_i = \mathrm{INT}(w_i(\beta+\tau)+\xi)$, where ξ is a uniform random number between 0 and 1. The weights of these M_i walkers are reset to one, and the copies then proceed to the next time step. Notice that $M_i = 0$ implies that the walker is killed.

To avoid a walker population explosion or collapse, practical DMC simulations adjust E_T dynamically to keep the population stable. This introduces a "population bias" that must be controlled for in production level calculations. Ideally, one should allow the population of walkers to fluctuate as much as is computationally feasible [46].

Additional improvements to DMC can be had through improving the propagator. First, while the exact propagator $G(\mathbf{r}, \mathbf{r}', \tau)$ is symmetric, the short-time approximation will generally violate this for finite time-steps. Using Eq. 3.7 and 3.4, we find that:

$$\tilde{G}_{DD}(\mathbf{r}, \mathbf{r}', \tau)|\Psi_T(\mathbf{r})|^2 = \tilde{G}_{DD}(\mathbf{r}', \mathbf{r}, \tau)|\Psi_T(\mathbf{r}')|^2 \tag{3.13}$$

This condition is enforced by introducing an accept/reject step after the move proposal. Rejections lower the effective diffusion constant, which can be incorporated into the branching term by replacing τ with τ_{eff} [43, 29], defined as

$$\tau_{eff} = \tau \frac{\left\langle |\Delta\mathbf{r}_{accepted}|^2 \right\rangle}{\left\langle |\Delta\mathbf{r}_{proposed}|^2 \right\rangle} \tag{3.14}$$

In the above formula, $\Delta\mathbf{r}_{proposed} = \mathbf{r}' - \mathbf{r}(\beta)$, where $\mathbf{r}'$ is the proposed move vector. After the accept reject step, $\Delta\mathbf{r}_{accepted} = \mathbf{r}(\beta+\tau) - \mathbf{r}(\beta)$.

For finite time-steps, there is also a tendency for walker's to become stuck in regions where $E_L(\mathbf{r})$ is extremely small. This is commonly handled by killing the walker after its age exceeds some specified number. To prevent a stuck walker from excessively branching, its branching factor is often restricted by the following energy filtering scheme. Defining $\Delta E = \langle E_L \rangle_f - E$ and introducing an energy cutoff E_{cut}, the branching factor in Eq. 3.6 is modified by multiplying the time-step by a scaling factor $a(E)$, where $a(E)$ is defined as:

$$a(E) = \begin{cases} 1, & \text{if } \Delta E > E_{cut} \\ -\frac{2}{E_{cut}}(\Delta E - 1.5E_{cut}), & \text{if } E_{cut} \leq \Delta E \leq 1.5E_{cut} \\ 0, & \text{if } \Delta E > 1.5E_{cut} \end{cases} \tag{3.15}$$

E_{cut} is usually chosen to be $E_{cut} = c\sigma_{E_L}$, where c is an adjustable parameter. Usually this energy filtering scheme *increases* the time-step error, but also increases the stability of the algorithm.

3.6 Reptation Monte Carlo

Reptation Monte Carlo is an alternative projector method which is based on the Feynman path-integral formulation of Schrödinger's equation [47]. To see how this works, consider a ground state "partition function" $\mathcal{Z}$ defined as:

$$\mathcal{Z}(\beta) = \langle \Psi_T | e^{-\beta \hat{H}} | \Psi_T \rangle \tag{3.16}$$

Splitting the projector into $n+1$ "time-slices" and inserting n resolutions of the identity between each pair of projectors, the partition function is expressed in real space as:

$$\mathcal{Z}(\beta) = \int d\mathbf{r}_0 d\mathbf{r}_1 \dots d\mathbf{r}_n \left[\Psi_T(\mathbf{r}_0) G(\mathbf{r}_0, \mathbf{r_1}, \tau) G(\mathbf{r}_1, \mathbf{r}_2, \tau) \dots G(\mathbf{r}_{n-1}, \mathbf{r}_n, \tau) \Psi_T(\mathbf{r}_n) \right] \tag{3.17}$$

Associating the variable $X = \{\mathbf{r}_0, \mathbf{r}_1, \dots, \mathbf{r}_n\}$ with a path, Eq. 3.17 formula can be recast as a discretized Feynman path-integral: $\mathcal{Z}(\beta) = \int \mathcal{D}X \Pi[X]$. $\Pi[X]$ is the path weight, given by the term in brackets in Eq. 3.17. We will discuss the actual form of $\Pi[X]$ later. The expectation value of the local operator $\hat{\mathcal{A}}$ over both the mixed and pure distributions are given respectively by:

$$\left\langle \hat{\mathcal{A}} \right\rangle_f = \frac{\langle \Psi_T | \hat{\mathcal{A}} e^{-\beta \hat{H}} | \Psi_T \rangle}{\langle \Psi_T | \Phi_0 \rangle} = \frac{\int \mathcal{D}X \Pi[X] \mathcal{A}(\mathbf{r}_0)}{\int \mathcal{D}X \Pi[X]} \tag{3.18}$$

$$\left\langle \hat{\mathcal{A}} \right\rangle_{|\Phi_0|^2} = \frac{\langle \Psi_T | e^{-\frac{\beta}{2} \hat{H}} \hat{\mathcal{A}} e^{-\frac{\beta}{2} \hat{H}} | \Psi_T \rangle}{\langle \Phi_0 | \Phi_0 \rangle} = \frac{\int \mathcal{D}X \mathcal{A}(\mathbf{r}_{\beta/2})}{\int \mathcal{D}X \Pi[X]} \tag{3.19}$$

The form of these expectation values is amenable to Metropolis Monte Carlo sampling, but instead of proposing transitions between different sets of walker coordinates like in VMC and DMC, we are proposing transitions between different paths X.

Let us consider the directed paths $X_1 = \{\mathbf{r}_0, \mathbf{r}_1, \dots, \mathbf{r}_n\}$ and $X_{-1} = \{\mathbf{r}_n, \mathbf{r}_{n-1}, \dots, \mathbf{r}_0\}$ derived from X. For generality, denote directed paths as X_d, where $d = 1, -1$. The "head"/"tail" of the directed path is the coordinate at the end/beginning of the list X_d. Reptation Monte Carlo proposes a new path X^* by removing the tail of X_d and appending a trial all-electron configuration $\mathbf{r}'$ to serve as the new head. If $\mathbf{r}_h$ is the old head position, the new head $\mathbf{r}'_h$ is proposed by a random drift-diffusion step starting at $\mathbf{r}_h$. This implies the transition probability for the reptation move is $R_d(X \to X^*) = G_{DD}(\mathbf{r}_h, \mathbf{r}'_h, \tau)$. The reverse move is a

drift-diffusion step from the new tail position $\mathbf{r}'_t$ to the old $\mathbf{r}_t$, implying $R_{-d}(X^* \to X) = G_{DD}(\mathbf{r}'_t, \mathbf{r}_t, \tau)$

The acceptance probability for a reptation move in the direction d is given by:

$$A_d(X \to X^*) = \min\left(1.0, \frac{R_{-d}(X^* \to X)}{R_d(X \to X^*)} \frac{\Pi[X^*]}{\Pi[X]}\right) \tag{3.20}$$

While the original RMC algorithm chose d randomly to ensure detailed balance [47], d is almost universally chosen by the "bounce algorithm" [48]. Specifically, d is kept fixed until a proposed reptation move is rejected, at which point the direction is reversed $d \to -d$. This method does *not* satisfy detailed balance condition, but it does satisfy the stationary state property of time-independent ergodic Markov chains. This approach dramatically increases the diffusion of the path's centroid.

3.6.1 Symmetrized Link Action

Since we know that the exact projector must be symmetric, we can explicitly symmetrize the short-time approximation to the propagator by taking $G_s(\mathbf{r}, \mathbf{r}', \tau) = \sqrt{G(\mathbf{r}, \mathbf{r}', \tau) G(\mathbf{r}', \mathbf{r}, \tau)}$. Using Eq. 3.7, we can rewrite $\Pi[X] = \exp(S[X])$, where the "action" $S[X]$ is defined by [48]:

$$S[X] = \ln \Psi_T(\mathbf{r}_0) + \ln \Psi_T(\mathbf{r}_n) - \sum_{i=0}^{n-1} L_s(\mathbf{r}_i, \mathbf{r}_{i+1}) \tag{3.21}$$

$$L_s(\mathbf{r}', \mathbf{r}) = \frac{(\mathbf{r}' - \mathbf{r})^2}{4\lambda\tau} + \frac{1}{2}(\mathbf{r}' - \mathbf{r}) \cdot (\mathbf{F}(\mathbf{r}') - \mathbf{F}(\mathbf{r})) \tag{3.22}$$

$$+ \frac{\tau}{2}\left[E_L(\mathbf{r}') + E_L(\mathbf{r}) + \lambda(\mathbf{F}^2(\mathbf{r}') + \mathbf{F}^2(\mathbf{r}))\right] \tag{3.23}$$

This way of writing $\Pi[X]$ has some advantages. First, $S[X]$ is time reversal invariant, meaning it has the same form for X_d and X_{-d}. Secondly, since $\Pi[X]$ is explicitly given, correlated sampling can be performed. The main disadvantage is that we are largely restricted to proposing head-moves by all-electron moves.

3.6.2 DMC Action

If we don't explicitly symmetrize the short-time propagator $G(\mathbf{r}, \mathbf{r}', \tau)$, and instead write $\Pi[X]$ in Eq. 3.17 just in terms of the importance sampled propagator $\tilde{G}(\mathbf{r}, \mathbf{r}', \tau)$, we find $\Pi[X]$ can be written as [47]:

$$\Pi[X] = \mathcal{P}[X] \exp\left(-\sum_{i=0}^{n-1} L_{DMC}(\mathbf{r}_i, \mathbf{r}_{i+1})\right) \tag{3.24}$$

$$\mathcal{P}[X] = |\Psi_T(\mathbf{r}_0)|^2 \tilde{G}_{DD}(\mathbf{r}_0, \mathbf{r}_1)\tilde{G}_{DD}(\mathbf{r}_1, \mathbf{r}_2)\ldots\tilde{G}_{DD}(\mathbf{r}_{n-1}, \mathbf{r}_n) \tag{3.25}$$

$$L_{DMC}(\mathbf{r}_i, \mathbf{r}_{i+1}) = \frac{\tau}{2}\left(E_L(\mathbf{r}_i) + E_L(\mathbf{r}_{i+1})\right) \tag{3.26}$$

$L_{DMC}(\mathbf{r}, \mathbf{r}')$ is the "DMC" link action, since it is equivalent to the branching term $\widetilde{G}_B(\mathbf{r}, \mathbf{r}')$ in diffusion Monte Carlo. $\mathcal{P}[X]$ is the probability the path X was generated by a drift-diffusion random walk starting at $\mathbf{r}_0$ and ending at $\mathbf{r}_n$. While this breaks the formal symmetry between X_d and X_{-d}, this leads to a great simplification of the acceptance ratio formula. Assuming that new head move $\mathbf{r}'_h$ are proposed in a way such that VMC detailed balance holds, then the $\mathcal{P}[X]$ terms cancel, leaving the simple expression for the acceptance ratio:

$$A_d(X \to X^*) = \min(1.0, e^{-(L_{DMC}(\mathbf{r}_h, \mathbf{r}'_h) - L_{DMC}(\mathbf{r}'_t, \mathbf{r}_t))}) \tag{3.27}$$

In addition to being a massive simplification of the accept/reject step, this approach decouples the move proposals from the path accept/reject step. As long as the proposed head move is a valid VMC configuration, we have total freedom to improve the VMC move proposals without it adversely affecting the action.

3.6.3 Algorithmic Improvements

The same pathologies and solutions we discussed for DMC also exist in RMC, but the problems are compounded. Since we are dealing with paths instead of isolated walkers, problems of stuck time-slices and frequent rejections can more readily cause ergodicity problems in RMC than DMC. These issues become more severe as more time-slices are used to represent the path. In this section, we discuss tricks to reduce the time-step error and increase the acceptance ratio of RMC.

The most obvious improvements to RMC can be made by replacing τ with τ_{eff}. This improves the time-step error when using both the symmetrized and DMC link actions. Use of energy-filtering in the reptation accept-reject step was found to improve the stability of the algorithm when using both link actions: reptiles rarely required forced acceptances over the course of the simulation.

The following two improvements were found to be effective only with the DMC link action. First, the improved drift-scaling propagator of Umrigar was found to be effective in fermionic systems [49]. Secondly, proposing head-moves through a sequence of N_e single electron moves seemed to decrease time-step error and noticeably increase the acceptance ratio.

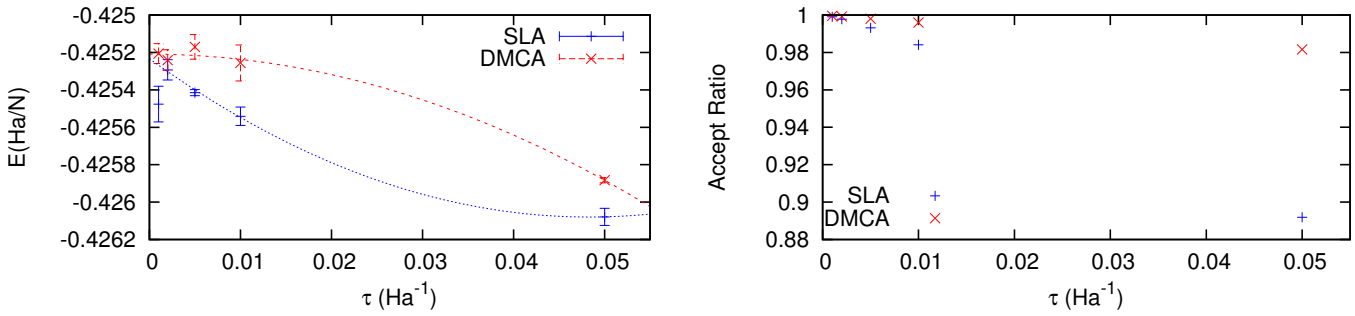

Figure 3.1: Comparison of improved link-actions in RMC. (Left) Total energy E as a function of time step τ using the symmetrized link-action (SLA) and DMC link-action (DMCA). (Right) Acceptance ratio as a function of time step for both actions. Time step error is lower and acceptance ratio is higher with the DMC action.

In Figure 3.6.3, we compare the performance of the symmetrized link-action with all-electron moves and energy-filtering against the DMC action with single-particle moves, energy-filtering, and an improved drift-diffusion propagator. The test system was 8 hydrogen atoms arranged in a cubic lattice in periodic boundary conditions. The nearest neighbor distance was chosen to be $1.6a_0$. Orbitals were taken from density functional theory. We used one and two-body Jastrows, the latter having independent functions for like and unlike spins. These were all short-ranged fully optimized b-spline Jastrows with proper cusp conditions. The projection time was chosen to be $\beta = 100Ha^{-1}$.

We find that the improved DMC action based RMC method has significantly higher acceptance ratios and lower time-step errors than the best symmetrized link action based RMC. This is most likely attributed to two features of the DMC link action. First, as previously discussed in the VMC chapter, all-electron moves have lower acceptance ratios than single-electron moves. This means that the symmetrized link action is limited by its constraint to all-electron move proposals, suffering from poorer reptile diffusion and higher probabilities of being stuck by pathological time-slices than the DMC action. Secondly, wave function forces near nodes in the trial wave function diverge. The explicit inclusion of these terms in the symmetrized link action requires a careful and consistent treatment when improving the drift part of the propagator, whereas these terms are not explicitly included in the DMC link action.

3.7 Fermion Sign Problem

Use of projection methods has assumed that the ground state wave function can be interpreted as a probability distribution. While this is formally exact for bosonic systems, fermionic systems must have negative regions to respect wave function antisymmetry under particle exchange.

Quite generally, if we wish to perform expectation values over a function $\Pi(X)$, but sample over a different distribution $\Pi'(X)$, we can do this with the following formula:

$$\langle A \rangle_{\Pi} = \frac{\langle wA \rangle_{\Pi'}}{\langle w \rangle_{\Pi'}} \tag{3.28}$$

In this case, A is an arbitrary observable and w is a weighting function, defined as $w(X) = \frac{\Pi(X)}{\Pi'(X)}$. If $\Pi(X)$ is a function with negative regions, we can still evaluate $\langle A \rangle_{\Pi}$ by choosing $\Pi'(X) = |\Pi(X)|$, and taking the weight to be $w(X) = \text{sgn}(\Pi(X))$.

What does the variance of this estimator look like? For now, we simplify the Eq. 3.28 by assuming that $w(X)$ and $A(X)$ are statistically independent. Noting that the variance of $\sigma_w = 1 - \langle w \rangle^2_{\Pi'}$, we look at the weight function's contribution to the observable's error bar. Assuming M samples, the error bar of $\sigma_w / \langle w \rangle_{\Pi'}$ is

$$Err = \frac{1}{\sqrt{M}} \sqrt{\frac{1}{\langle w \rangle_{\Pi'}} - 1} \tag{3.29}$$

In the context of p-QMC, if the trial fermionic ground state wave function has a nonzero overlap with the bosonic ground state $|\Phi_0^B\rangle$, then $|\Psi_T\rangle$ will eventually evolve to $|\Phi_0^B\rangle$ after long enough projection times β. Attempting to estimate fermionic expectation values from the bosonic distribution through the previously mentioned sign factoring trick leads to an exponentially scaling algorithm. Specifically, one can show that for fermionic systems, $\langle w \rangle_{\Psi_0^B} \sim \exp(-\beta(E_0^F - E_0^B))$, where E_0^F and E_0^B are the fermionic and bosonic ground state energies respectively [50, 51]. Plugging this into Eq. 3.29, one can see that the error bar for fermionic observables will scale like $\exp(\beta(E_0^F - E_0^B))$.

Note that $E_0^F - E_0^B$ refers to total energies, and therefore is extensive. Generally speaking then, estimating exact ground state fermionic properties to arbitrary precision is an exponentially scaling algorithm with the number of particles. This is the "sign-problem" of projector Monte Carlo, and is quite general to fermionic problems in both first and second quantized theories [52], and in both zero and finite temperature theories.

The most widely used way around the sign problem in ground state calculations is to impose the "fixed-node" approximation [43, 44]. This works by establishing the boundary condition that the projected wave function go to zero wherever $\Psi_T(\mathbf{r}) = 0$. This is equivalent to modifying our Hamiltonian to be the following:

$$\hat{H}^{FN} = \hat{H} + \delta(\Psi_T(\mathbf{r})) \tag{3.30}$$

$\hat{H}^{FN}$ is called the "fixed-node Hamiltonian", and its bosonic ground state wave function $|\Phi_0^{FN}\rangle$ is the fixed-node wave function. Despite being a bosonic solution, the fixed-node wave function is applicable to fermionic

wave functions by the "tiling theorem" [32]. This states that ground state fermionic wave functions possess nodal regions which are all related by symmetry. Insofar as our nodal surface obeys the tiling theorem, a bosonic solution within a single nodal pocket produces the best wave function compatible with the nodes.

While not exact, the fixed-node approximation still obeys the variational theorem, providing a strict upper bound on the ground state energy. In the event that we choose the exact nodal surface, all static ground state properties will be exact. Practically speaking, projection to the fixed node wave function considerably refines the starting $|\Psi_T\rangle$. Independent studies attempting to assess the impact of this uncontrolled approximation on realistic calculations find that the nodal surface is usually quite good. Single Slater-Jastrow based DMC calculations on the G2 test set show that even with this crude approximation, p-QMC is comparable with leading quantum chemistry methods in terms of accuracy [8]. Benchmarks of the fixed-node approximation in solid beryllium have shown that it is not the dominant source of error [7].

Chapter 4

Density Functional Theory

4.1 Introduction

Up to now, all methods we have discussed have been "wave function methods": they attempt to construct the ground state wave function $\Phi_0(\mathbf{r})$ of the physical Hamiltonian $\hat{H}$. The breakthrough of density functional theory (DFT) was the realization that rather than work directly with the $3N_e$ variable many-body wave function, one can without loss of generality work with the ground state density instead.

In this chapter, we will focus on presenting the theory that supports the most commonly used variant of density functional theory, Kohn-Sham DFT. After discussing the Kohn-Sham equations, we discuss the common approximations to the Kohn-Sham exchange-correlation functionals. We present nothing new in this chapter, but the formalism laid out will be critical in understanding how traditional DFT simulations succeed or fail in treating important phase boundaries in the high-pressure equations of state of hydrogen and hydrogen-helium mixtures.

4.2 Hohenberg-Kohn Theorems

The origin and validity of density functional theory comes from the Hohenberg-Kohn theorems. Referring back to the electronic Hamiltonian in Eq. 2.2, we define the external potential $V_{ext}(\mathbf{r})$ as:

$$V_{ext}(\mathbf{r}) = \sum_J v^{eI}(\mathbf{r}, \mathbf{R}_J) \tag{4.1}$$

Letting $\rho_0(\mathbf{r})$ denote the ground state density, and taking V_{II} from Eq. 2.2, the Hohenberg-Kohn theorems are given by [53]:

1. **The external potential V_{ext} is uniquely determined by the ground state density $\rho_0(\mathbf{r})$ (up to a constant).**

2. **There exists a functional of the density, $E_{HK}[\rho] = \int d\mathbf{r}\rho(\mathbf{r})V_{ext}(\mathbf{r}) + F[\rho] + V_{II}$, whose varia-**

tional minimum corresponds to the ground state energy E_0 and density $\rho_0(\mathbf{r})$ of the true many-body system.

Theorem I states that the ground state density uniquely determines (up to a constant) the external potential V_{ext}. Knowing $V_{ext}(\mathbf{r})$ allows us to specify the many-body Hamiltonian, whose solutions contain everything describable about a given system.

Unpacking Theorem II, the integral in $E_{HK}[\rho]$ and the ion-ion potential V_{II} are system specific–they are easily evaluated and depend only on the arrangement and type of ions $\mathbf{R}$. What's interesting is that $F[\rho]$ does *not* depend on the specific system. It is a universal exchange correlation functional which gives the electronic kinetic energy and all electron-electron contributions to the total energy. Thus, knowing this universal functional $F[\rho]$ allows us to solve all ground state electronic structure problems.

4.3 Kohn-Sham Equations

While profound, the Hohenberg-Kohn theorems do little to tell us what the proper form of the universal exchange-correlation functional should be. Finding workable approximations to this functional is the core of DFT. Some approaches such as Thomas-Fermi and "orbital-free" DFT attempt to write direct approximations to the universal functional $F[\rho]$ as analytic expressions of the density and its gradients [54], but these approaches have comparatively poor accuracy for condensed matter and chemical systems.

Kohn-Sham density functional theory makes the ansatz there exists an auxiliary non-interacting theory whose ground state density $\rho_0(\mathbf{r})$ is identical to that of the true many-body system [55, 54]. Inspired by Hartree-Fock theory, one introduces a set of single-particle orbitals $\{\phi_0(\mathbf{r}), \phi_1(\mathbf{r}), \ldots, \phi_M(\mathbf{r})\}$. The density is then written as $\rho(\mathbf{r}) = \sum_{i=0}^{N-1} |\phi_i(\mathbf{r})|^2$. The Kohn-Sham density functional is given by:

$$E_{KS}[\rho] = T_{KS}[\rho] + E_{Hartree}[\rho] + E_{xc}[\rho] + \int d\mathbf{r}\rho(\mathbf{r})V_{ext}(\mathbf{r}) + V_{II} \tag{4.2}$$

The kinetic energy functional $T_{KS}[\rho]$ and $E_{Hartree}[\rho]$ are given by the following:

$$T_{KS}[\rho] = -\frac{1}{2}\sum_{i=0}^{N-1}\int d\mathbf{r}\phi_i^*(\mathbf{r})\nabla^2\phi_i(\mathbf{r}) \tag{4.3}$$

$$E_{Hartree}[\rho] = \int d\mathbf{r}d\mathbf{r}'\frac{\rho(\mathbf{r})\rho(\mathbf{r}')}{|\mathbf{r}-\mathbf{r}'|} \tag{4.4}$$

$E_{xc}[\rho]$ is known as the "exchange-correlation" functional, and includes all the missing energy from the single-particle picture coming from particle statistics and correlation effects. Ideally, it is defined as $E_{xc}[\rho] =$

$F[\rho] - (T[\rho] + E_{Hartree}[\rho])$,

If one minimizes the Kohn-Sham total energy functional with respect to the single-particle orbitals, subject to the constraint that the orbitals are orthonormal, one arrives at the Kohn-Sham equations:

$$\left(-\frac{1}{2}\nabla^2 + v_{eff}(\mathbf{r})\right)\phi_i(\mathbf{r}) = \epsilon_i\phi_i(\mathbf{r}) \tag{4.5}$$

The effective potential $v_{eff}(\mathbf{r})$ is given by:

$$v_{eff}(\mathbf{r}) = V_{ext}(\mathbf{r}) + \int d\mathbf{r}' \frac{\rho(\mathbf{r}')}{|\mathbf{r} - \mathbf{r}'|} + \frac{\delta E_{xc}[\rho]}{\delta\rho(\mathbf{r})} \tag{4.6}$$

Intuitively, the Kohn-Sham equations are formally similar to the Hartree-Fock equations, with the exception that the missing exchange-correlation energy can be added in with $E_{xc}[\rho]$. Notice that we are not "fixing" Hartree-Fock theory, as the formal justification for introducing $E_{xc}[\rho]$ comes from the Hohenberg-Kohn theorems [53].

4.4 Exchange-Correlation Functionals

Most approximations to $E_{xc}[\rho]$ begin by decomposing it into a sum of an exchange functional $E_x[\rho]$ and a correlation functional $E_c[\rho]$. Separate approximations are then constructed for each functional. In Hartree-Fock theory, the exchange functional can be written exactly as:

$$E_x^{HF}[\rho] = -\sum_{i<j}\int d\mathbf{r}d\mathbf{r}' \frac{\phi_i^*(\mathbf{r}')\phi_j^*(\mathbf{r})\phi_i(\mathbf{r})\phi_j(\mathbf{r}')}{|\mathbf{r} - \mathbf{r}'|} \tag{4.7}$$

This expression for the "exact exchange" is actually used in some functionals like hybrids, but most of the functionals we discuss introduce simpler approximations to exchange to decrease computational cost.

4.4.1 LDA

In the homogeneous electron gas, the exchange-correlation energy per particle $\epsilon_{xc}^{hom}(\rho) = \epsilon_x^{hom}(\mathbf{r}) + \epsilon_c^{hom}(\mathbf{r})$ is known as a function of density and polarization. The exchange energy is given by $\epsilon_x^{hom}(\rho) = -\frac{3}{4}(\frac{6}{\pi}\rho)^{\frac{1}{3}}$ and can be obtained from a direct application of Eq. 4.7. In contrast, $\epsilon_c^{hom}(\mathbf{r})$ is not known analytically, but has been numerically established through quantum Monte Carlo calculations [56]. With these expressions in hand, LDA generalizes the homogeneous electron gas results to inhomogeneous systems with the simple exchange-correlation function ansatz:

$$E_{xc}^{LDA} = \int d\mathbf{r}\rho(\mathbf{r})\epsilon_{xc}^{hom}(\rho(\mathbf{r})) \tag{4.8}$$

4.4.2 GGA

While the $E_{xc}^{LDA}[\rho]$ functional depends on just the local density $\rho(\mathbf{r})$, functionals within the generalized gradient approximation (GGA) framework seek to improve upon this by including an explicit dependence on density gradients $\nabla\rho(\mathbf{r})$. Using the exchange functional as a concrete example, one modifies the LDA functional in Eq. 4.8 to read:

$$E_{x}^{GGA} = \int d\mathbf{r}\rho(\mathbf{r})F_{x}^{GGA}(s)\epsilon_{x}^{hom}(\rho(\mathbf{r})) \tag{4.9}$$

Here, $F_x^{GGA}(s)$ is the "exchange enhancement factor", s is the reduced gradient given by $s = |\nabla\rho|/2k_f\rho$, and $k_f = (3\pi^2\rho)^{1/3}$. A corresponding $F_c^{GGA}(s)$ exists for the correlation functional. $F_x^{GGA}(s)$ is not analytically derivable from first principles for all s, but its construction is guided by exact constraints on both the large s and small s behavior. Interestingly, the GGA form is not flexible enough to account for all exact constraints, so we will discuss the trade-offs incurred by these approximations.

In order to recover the homogeneous electron gas limit, GGA's must have the following form for small s: $F_x(s) = 1 + \mu s^2$. There are two mutually exclusive choices one can make for μ. Using the gradient expansion approximation (GEA), one can show that $\mu_{GEA} = 10/81$ is required to recover the slowly-varying electron gas [57]. However, if one fits the enhancement factor to reproduce the exchange energies of neutral atoms and molecules, one finds a value of $\mu \approx 2\mu_{GEA}$ [58, 59]. The consequence of this is that GGA's that enforce the GEA predict more accurate bulk moduli and lattice constants, but doing so less accurately predicts total and atomization energies [59, 60]. Some functionals are chosen to satisfy one of these two limits exactly. PBEsol [60] is chosen to satisfy the GEA, whereas B88 [61] and revPBE [62] are chosen to satisfy $\mu \approx 2\mu_{GEA}$. However, most GGA's will fall somewhere between the two extremes. Wu-Cohen, a GGA designed for solids, is an oddity in that it is designed to reduce to PBE as $s \to 0$, but begins to recover the GEA starting at $s > 0.4$.

One of the more popular constraints on the large s behavior of $F_x(s)$ is derived from the Lieb-Oxford bound [63]. This is a rigorous result, stating that $E_{xc}[\rho] \leq -C\int d\mathbf{r}(\rho(\mathbf{r}))^{4/3}$, where $C = 1.64$ [64] (revised downward from the original $C = 1.68$). Functionals like PBE [65], revPBE, and rPBE [66] enforce this constraint by asymptoting to a fixed limiting value $1 + \kappa$. The specific value of κ will often depend on whether one is trying to satisfy the stated Lieb-Oxford bound, or the much stricter "local" Lieb-Oxford bound [65, 54], given by $\epsilon_{xc}(\rho(\mathbf{r})) \leq -C\rho(\mathbf{r})^{4/3}$.

In molecular systems, satisfying the Lieb-Oxford bound is often abandoned in exchange for setting the correct scaling behavior of $F_x(s)$. In particular, the exact exchange energy density ϵ_x tends towards $-\frac{1}{r}$ as one takes $r \to \infty$. From this, it can be shown that $F_x(s)$ must scale like $s/\ln(s)$ for large s [61]. This approach was successfully used to construct the B88 functional.

4.4.3 Hybrid

Hybrid functionals improve upon the basic $E_x^{GGA}[\rho]$ by including a fraction of exact exchange:

$$E_x^{hybrid}[\rho] = (1-\alpha)E_x^{GGA}[\rho] + \alpha E_x^{HF}[\rho] \tag{4.10}$$

Here, α is the "mixing fraction" of exact exchange. Note that $\alpha = 0$ would reduce to the $E_x^{GGA}[\rho]$, whereas $\alpha = 1$ would reduce to Hartree-Fock exchange.

The original motivation for including a small amount ($\alpha \approx 0.25$) of exact exchange was from the adiabatic connection formula, which rigorously relates the non-interacting Kohn-Sham $E_{xc}^{KS}[\rho]$ functional to the exact exchange-correlation functional [67, 68]. Hybrid functionals have been demonstrated to provide more accurate bond-lengths, vibrational frequencies, and atomization energies than the GGA's on which they are based [68]. Commonly used hybrids are B3LYP [69, 67] and $\omega B97X$ [70] for molecular systems, and HSE [71] or PBE0 [68] for solid-state systems.

4.4.4 Non-local van der Waals

One of the major failures of semi-local functionals is their inability to properly describe van der Waals interactions. van der Waals interactions are long ranged correlations arising from the dynamical correlations induced between spatially separated charge distributions. While some approaches like the vdW-TS [72] and Grimme [73] corrections tack on the proper $1/r^6$ dependence in post-processing, non-local vdW functionals attempt to reproduce this behavior generically from a properly constructed density functional.

The non-local correlation functionals work by assuming the decomposition $E_{xc}[\rho] = E_{xc}^{sl}[\rho] + E_c^{nl}[\rho]$. $E_{xc}^{sl}[\rho]$ is "semi-local", or GGA like contribution, whereas $E_c^{nl}[\rho]$ is the non-local correlation, given by the following integral.

$$E_c^{nl}[\rho] = \int d\mathbf{r}d\mathbf{r}'\rho(\mathbf{r})K(\mathbf{r},\mathbf{r}')\rho(\mathbf{r}') \tag{4.11}$$

The vdW-DF [74] and vdW-DF2 [75] family of functionals successfully approximate the kernel $K(\mathbf{r},\mathbf{r}')$ by using a plasmon-pole based approximation to the dielectric function. The major subtlety in this framework is that $K(\mathbf{r},\mathbf{r}')$ depends upon a separate semi-local functional $E_{xc}^{i}[\mathbf{r}]$, termed the "inner" functional, which

is usually different from the E_{xc}^{sl} functional, termed the "outer-functional" [74]. Interestingly, this mismatch between E_{xc}^{sl} and E_{xc}^{i} breaks some exact constraints which GGA's usually obey, such as conservation of the exchange-correlation hole [76]. This issue was formally identified and corrected by introducing an "exchange-consistent" exchange functional [76], although the issue was approximately corrected much earlier with exchange functionals independently optimized for use with vdW-DF or vdW-DF2 type non-local correlation functionals [77, 78].

Chapter 5

Finite Temperature Methods

5.1 Introduction

Up to now, we have discussed ground state electronic structure methods. In this chapter, we review basic quantum and classical thermodynamics and then discuss how we can sample various thermodynamic ensembles through the use of molecular dynamics. Due to the importance of computing accurate free energies in determining the immiscibility transition in hydrogen-helium mixtures and the phase diagram of lithium, we discuss the theory and use of thermodynamic and coupling-constant integration. While most of this chapter is a review of existing methods, instabilities of some lithium structures at the classical pair potential level forced us to modify the traditional coupling-constant integration technique. We present our method for circumventing these issues and test its validity in the last part of this chapter.

5.2 Quantum Thermodynamics

All equilibrium finite temperature properties of a quantum system can be obtained from the density matrix $\hat{\rho} = e^{-\beta \hat{H}}$, where $\hat{H}$ is the full Hamiltonian of the system. Thermal expectation values are given by $\left\langle \hat{\mathcal{A}} \right\rangle_\rho = \mathrm{Tr}[\hat{\rho}\hat{\mathcal{A}}]/\mathcal{Z}$. $\mathcal{Z}$ is the partition function, which is given by:

$$\mathcal{Z} = \mathrm{Tr}[e^{-\beta \hat{H}}] \tag{5.1}$$

Noting that the density matrix is formally identical to the projection operator discussed in Chapter 3, we can write it as a path-integral. While one can use the full Hamiltonian to sample the exact many-body density matrix [79], we will confine ourselves to the Born-Oppenheimer approximation. Additionally, we will assume the nuclei possess Boltzmann statistics. These assumptions lead to the Born-Oppenheimer partition function $\mathcal{Z}_{BO}$, given by [80, 5]:

$$\mathcal{Z}_{BO} = \int \mathcal{D}[\mathbf{R}(\beta)] \exp\left(-\beta \int_0^\beta d\tau \left[T_n(\mathbf{R}(\tau)) + F_{el}(\mathbf{R}(\tau))\right]\right) \tag{5.2}$$

Since the partition function is defined in terms of a trace, the paths referred to in Eq. 5.2 are subject to the boundary condition that $\mathbf{R}(\tau = 0) = \mathbf{R}(\tau = \beta)$. $T_n(\mathbf{R})$ is defined as $T_n(\mathbf{R}) = \frac{m}{2}|\frac{\partial \mathbf{R}}{\partial \tau}|^2$, where for notational convenience, we have assumed all nuclei have the same mass m. $F_{el}(\mathbf{R})$ is the free energy of the electron system with the ions fixed at position $\mathbf{R}$. It is defined as $F_{el}(\mathbf{R}) = \ln(\sum_i e^{-\beta E_i(\mathbf{R})})$. In DFT, $F_{el}(\mathbf{R})$ is calculated using the finite-temperature Mermin functional [54]. While path-integral Monte Carlo methods are capable of computing $F_{el}(\mathbf{R})$, QMC path-integral methods based on coupled electron-ion Monte Carlo [81] assume that $F_{el}(\mathbf{R}) \approx E_0(\mathbf{R})$, which is valid when the energy gap $\Delta E > k_b T$.

As the ionic masses go to infinity, we recover the classical partition function, given by [82]:

$$\mathcal{Z}_{cl} = \frac{1}{N!}\frac{1}{h^{3N}} \int d\mathbf{p} d\mathbf{q} e^{-\beta H(\mathbf{p},\mathbf{q})} \tag{5.3}$$

$H(\mathbf{p}, \mathbf{q})$ is the classical Hamiltonian, $H(\mathbf{p}, \mathbf{q}) = \mathbf{p}^2/2m + U(\mathbf{q})$. If the only velocity dependence in the Hamiltonian is from the kinetic energy, the kinetic energy part of the integral can be explicitly evaluated, resulting in the following expression for the classical partition function:

$$\mathcal{Z}_{cl} = \frac{\Omega^N}{N!\Lambda^{3N}} \int d\mathbf{q} e^{-\beta U(\mathbf{q})} \tag{5.4}$$

Λ is the de Broglie wavelength, given by $\Lambda = \sqrt{h^2/(2\pi m k_b T)}$.

5.3 Quasi-harmonic Approximation

For most solids at sufficiently low temperatures, one can treat finite temperature properties reasonably well within the "quasi-harmonic approximation" [54]. Specifically, if the ion positions $\mathbf{R}_0$ correspond to the lowest energy point in $E_0(\mathbf{R})$, one performs a Taylor expansion of $E_0(\mathbf{R})$ with respect to ionic displacements $\Delta\mathbf{R} = \mathbf{R} - \mathbf{R}_0$ up to second order. One can then compute the normal modes and their energies, which then allows the calculation of finite temperature properties. The primary advantage of this method is that the computational cost stems from computing the force constant matrix $C_{i_\alpha j_\beta} = \frac{\partial E_0}{\partial R_{i_\alpha} \partial R_{j_\beta}}|_{\mathbf{R}_0}$. While technically a $3N \times 3N$ matrix, crystalline symmetry significantly reduces the number of independent matrix elements. The independent matrix elements are computed using some zero temperature theory; most commonly DFT.

One should keep in mind the limits of the quasi-harmonic approximation before blindly applying it to a given system of interest. If fluctuations about an ion's equilibrium position expose it to anharmonic parts

of the potential, one can incur sizeable quantitative errors and occasionally qualitative errors. In hydrogen and helium, zero-point fluctuations are large enough for these solids to experience strong anharmonic effects even at zero temperature. For heavier elements, one simply has to go to high enough temperatures for the quasi-harmonic approximation to break down. We will see effect in detail when we discuss the equation of state of dense lithium.

5.4 Molecular Dynamics

In cases where the quasi-harmonic approximation breaks down, direct sampling of the partition function in Eq. 5.2 is required.

When DFT is used to calculate $F_{el}(\mathbf{R})$, sampling is usually done using Born-Oppenheimer molecular dynamics. To see how this works, consider how we would sample classical nuclei $\mathbf{R}$ within the microcanonical ensemble. Starting with initial conditions on the particle positions and velocities, interatomic forces are used to approximately integrate Newton's equation. Given the chaotic nature of these solutions [83], one can use these trajectories to sample the microcanonical ensemble. This allows one to compute thermodynamic expectation values like those described in Chapter 3, provided the simulation is run long enough to generate sufficient numbers of statistically uncorrelated points.

Moving from the microcanonical ensemble to the canonical ensemble requires introducing thermostats which couple the system's dynamical variables $\mathbf{V}$ to a bath. Langevin thermostats introduce this coupling stochastically by adding white noise to the particle velocities [84]. If the magnitude of the noise is set according to the fluctuation dissipation theorem, the system will sample the canonical ensemble. Generalized Langevin thermostats (GLE) exist which use correlated noise to either sample the canonical distribution more efficiently or sample non-canonical distributions [85, 86].

With the Nose-Hoover thermostat, coupling to the bath is implemented by rescaling the particle momenta as $\mathbf{p} \rightarrow \mathbf{p}/s$, where s is a fictitious variable representing the bath [83]. Fictitious terms representing the kinetic and potential energy of the variable s are introduced into the system's Hamiltonian, which are used to dictate the deterministic time evolution of s. The major advantage of this approach is that finite-temperature time-correlation functions are preserved, in contrast with Langevin approaches. However, the fictitious mass associated with the fictitious momentum of s must be tuned to minimize the autocorrelation time of observables. Additionally, ergodicity can sometimes be a problem when the Nose-Hoover thermostat is used in harmonic systems–the bath and harmonic degrees of freedom can swap energy in a periodic manner [87], much akin to the Ulam-Pasta-Fermi problem [88].

The molecular dynamics framework for classical nuclei can be generalized to propagate path-integral configurations $\mathbf{R}(\beta)$ consistent with Eq. 5.2 [80]. The method is known as path-integral molecular dynamics (PIMD). As in RMC, we have control over the number of beads used to represent the path. However, in contrast to classical molecular dynamics, we no longer have access to real-time correlation functions. To sample the canonical distribution, we use a combination of Langevin and generalized Langevin (GLE) thermostats [86]. The ability of GLE thermostats to sample non-canonical distributions can be used to drastically reduce the number of time-slices needed to represent a path.

5.5 Thermodynamic Integration

With the ability to calculate thermodynamic expectation values, the next step is to construct an equation of state for phases in which we are interested. This is done by estimating the internal energy E and pressure P as a function of volume and temperature via molecular dynamics or Monte Carlo methods. In general, these methods will not yield the free energy of a system when used in isolation. In this and the following section, we discuss how a combined use of coupling-constant integration and thermodynamic integration can give us the free energy of a system.

If one can establish the free energy at a specific reference point (T_0, Ω_0), the free energy at any other point can be calculated through thermodynamic integration. Let the total energy and pressure of a system at temperature T and volume Ω be $E(T, \Omega)$ and $P(T, \Omega)$ respectively. Assuming the volume is fixed at the reference point value Ω_0, the free energy at arbitrary temperatures is given by:

$$F(T', \Omega_0) = T' \left(\frac{F(T_0, \Omega_0)}{T_0} - \int_{T_0}^{T'} dT \frac{E(T, \Omega_0)}{T^2} \right) \tag{5.5}$$

If instead the temperature is fixed at T_0, we can get the free energy at any other volume Ω' by:

$$F(T_0, \Omega') = F(T_0, \Omega_0) - \int_{\Omega_0}^{\Omega'} d\Omega P(T_0, \Omega) \tag{5.6}$$

The free energy at any arbitrary point $F(T, \Omega)$ can be obtained by sequentially applying Eqs. 5.5 and 5.6.

5.6 Coupling-Constant Integration

The above procedure works provided we can establish the reference point free energy $F(T_0, \Omega_0)$. Coupling-constant integration is the most general means of accomplishing this [83], and is based on a very simple idea.

The fundamental theorem of calculus states that:

$$F_{\lambda=1} - F_{\lambda=0} = \int_0^1 d\lambda \frac{dF_\lambda}{d\lambda} \tag{5.7}$$

If we can introduce a λ dependence to the free energy in such a way that $F_{\lambda=0}$ is the free energy of system A and $F_{\lambda=1}$ is the free energy of system B, then assuming there are no singularities in $dF/d\lambda$, Eq. 5.7 will give us $\Delta F_{AB} = F_B - F_A$. The most common way of introducing this dependence at the classical level is to define a λ-dependent potential energy surface of the following form:

$$U_\lambda(\mathbf{r}) = f(\lambda)U_A(\mathbf{r}) + g(\lambda)U_B(\mathbf{r}) \tag{5.8}$$

$f(\lambda)$ and $g(\lambda)$ are arbitrary except that they must enforce $U_{\lambda=0}(\mathbf{r}) = U_A(\mathbf{r})$ and $U_{\lambda=1}(\mathbf{r}) = U_B(\mathbf{r})$. Using the definition of the classical partition function for a system with potential energy $U_\lambda(\mathbf{r})$, $dF_\lambda/d\lambda$ can be calculated explicitly as:

$$\begin{aligned} \frac{dF_\lambda}{d\lambda} &= \frac{\int d\mathbf{r} \partial U_\lambda/\partial\lambda e^{-\beta U_\lambda(\mathbf{r})}}{\int d\mathbf{r} e^{-\beta U_\lambda(\mathbf{r})}} \\ &= \left\langle \frac{\partial U_\lambda}{\partial \lambda} \right\rangle_{U_\lambda} \end{aligned} \tag{5.9}$$

Eq. 5.9 is readily evaluated with a molecular dynamics or Monte Carlo simulation, provided that the estimator $\partial U_\lambda/\partial\lambda$ has finite variance. This can then be plugged into Eq. 5.7 to evaluate the free energy difference between systems A and B.

Assume the reference point at (T_0, Ω_0) has a potential given by $U_{A_0}(\mathbf{r})$. If we can construct an integration path $A_0 \to A_1 \to \ldots \to A_N$ from our system A_0 to a system A_N where we know the free energy F_{A_N}, then we can use equation Eq. 5.7 to find the energy of the reference point by:

$$F_{A_0} = \sum_{i=0}^{N-1} \Delta F_{A_i A_{i+1}} + F_{A_N} \tag{5.10}$$

In the following sections, we will discuss how reference points are chosen for both solid and liquid atomic systems.

5.6.1 Liquids

Coupling-constant integration for QMD simulations of liquids is generally done in two steps. First, the system described by the DFT potential energy surface $U_{DFT}(\mathbf{r})$ is integrated to a classical pair potential system $U_{cl}(\mathbf{r})$, where the pair interactions are optimized to minimize the mean square error between the classical and DFT forces. This procedure is known as "force-matching" [89]. The last step integrates $U_{cl}(\mathbf{r})$ to the non-interacting ideal gas $U_{id}(\mathbf{r}) = 0$.

The λ-dependent potential for the first step is taken to be $U_\lambda(\mathbf{r}) = \lambda U_{cl}(\mathbf{r}) + (1-\lambda)U_{DFT}(\mathbf{r})$. For the second step, the following form is taken: $U_\lambda(\mathbf{r}) = (1-\lambda)^2 U_{cl}(\mathbf{r})$. The λ^2 factor is to suppress the diverging variance of $\langle \partial U/\partial\lambda \rangle$ as $\lambda \to 1$ [90]. This is a generic problem when integrating from interacting to non-interacting potentials. With interacting potentials, the energy of two particles separated by a distance r usually diverges to $+\infty$ as $r \to 0$ to prevent the particles from overlapping. Non-interacting potentials have no such constraint, so that as $\lambda \to 1$, configurations will be generated which will occasionally have unphysically small inter-particle separations, which causes spikes if U_λ is constructed such that $\frac{d}{d\lambda}U_\lambda = U_{cl}$.

Now all that remains is to calculate the free energy of the non-interacting ideal gas. Since we are dealing with both single component and binary mixtures, we will focus on the free energy of the latter. Let two atomic species have N_a and N_b atoms respectively, and let $N = N_a + N_b$. We define the molar fraction of species a as $x_a = N_a/N$, with x_b equivalently defined.

The free energy of the classical ideal gas is given by the following expression:

$$\frac{F^0_{liq}}{N} = k_b T \left[x_a \ln\left(\frac{\rho_a}{\rho_a^Q}\right) + x_b \ln\left(\frac{\rho_b}{\rho_b^Q}\right) - 1 \right] \tag{5.11}$$

Here, $\rho_a^Q = \left(\frac{m_a k_b T}{2\pi\hbar^2}\right)^{3/2}$, and likewise for ρ_b^Q. The single component free energy can be obtained by dropping the second term in the brackets.

5.6.2 Solids

The target reference system for solids is an Einstein crystal, which is defined by the following potential:

$$U_{harm}(\mathbf{R}) = \frac{1}{2}\Lambda_E(\mathbf{R} - \mathbf{R}_0)^2 \tag{5.12}$$

Here, $\mathbf{R}_0$ is the equilibrium position of all N atoms, and Λ_E is the force constant. While one could in principle use different force constants for each atom, we found the use of one to be sufficient for our purposes.

Coupling-constant integration is more complicated for solids than it is for liquids for two reasons. First,

imposing a harmonic potential of the Einstein crystal breaks translational invariance in the system. When integrating from a translationally invariant potential (such as DFT or a pair-potential) to the Einstein crystal, the center-of-mass of the system is free to wander, which causes divergences from the fixed harmonic potential as $\lambda \to 0$ or $\lambda \to 1$ (depending on definition of U_λ) [83]. This is handled by performing all thermodynamic integration steps subject to a fixed center-of-mass constraint, and then adding free energy corrections to get the free energy of the unconstrained system.

Another complication is the fact that crystals stable at the DFT level will in general not be stable using a force-matched pair potential. This was a problem in our studies in dense lithium, where only one out of four candidate ground state structures were stable at finite temperature when using a force matched pair-potential. We were able to deal with this by using the following classical potential:

$$U_{mix}(\mathbf{r}) = U_{pair}(\mathbf{r}) + U_{harm}(\mathbf{r}) \tag{5.13}$$

Integration from DFT to this potential is done with the following potential: $U_\lambda(\mathbf{r}) = \lambda U_{mix}(\mathbf{r}) + (1 - \lambda)U_{DFT}(\mathbf{r})$. Then, integration from the classical pair-potential to the Einstein crystal is done with a potential given by: $U_\lambda(\mathbf{r}) = (1-\lambda)^2 U_{pair}(\mathbf{r}) + U_{harm}(\mathbf{r})$. As we discussed in the liquid section, the λ^2 factor is to prevent divergences in the $\langle \partial U/\partial\lambda \rangle$ estimator stemming from non-interacting particle overlaps.

The classical free energy of an Einstein crystal with the center-of-mass correction is given by the following [91, 83]:

$$\frac{\beta}{N}F^0_{ein} = \frac{1}{N}\ln\left(\frac{N}{\Omega}\Lambda^3\right) + \frac{3}{2}\left(1 - \frac{1}{N}\right)\ln\left(\frac{\beta\Lambda^2\Lambda_E}{\pi}\right) \tag{5.14}$$

While this is not the way that thermodynamic integration is typically done in solids, we self consistently checked its correctness using the following. We chose a system with $N = 144$ atoms, a volume of $462.44\mathring{A}^3$ at T=500K. It was initialized in the $R\bar{3}m$ structure. A classical pair potential was fit to this system and found to be stable. The classical free energy of the pair-potential was then calculated using harmonic potentials with two different spring constants: $\Lambda_E = 2.0eV/\mathring{A}$, and $\Lambda_E = 0.5eV/\mathring{A}$. If our integration procedure is correct, there should be no dependence of the reference point free energy on the particulars of our potential. Varying the Einstein crystal spring constant Λ_E is one such test. In Table 5.7, we find that this is indeed true to within statistical error of approximately $0.2mHa/atom$.

5.7 Table

	$\Lambda_E = 0.5$	$\Lambda_E = 2.0$
F^0_{harm}	-0.004366	-0.001096
$\Delta F_{harm \to mix}$	0.015015(58)	0.01143(19)
$\Delta F_{mix \to pair}$	0.000484(72)	0.000908(98)
F_{pair}	0.011133(96)	0.01124(21)

Table 5.1: Results from computing the reference-point free energy with two different potentials. All units are in $Ha/atom$. The rows represent the thermodynamic integration steps listed in the text. The columns represent two choices for the Einstein crystal spring constant Λ_E. As expected, the total free energy of the reference point (last line) is independent of Λ_E, indicating its correctness.

Chapter 6

Force and Stress Estimators

6.1 Introduction

Despite the importance of forces and stresses for calculating equilibrium geometries and elastic properties, their use in QMC calculations is sparing. The reason for the lack of QMC forces stems from the statistical nature of QMC. All observables must have well defined means and variances to allow estimation via the central limit theorem. Naïve force estimators can be easily shown to have infinite variance.

In this chapter, I will present the theory and implementation of QMC force and stress estimators for use in bulk systems. In the first section, we will review periodic boundary conditions and the general treatment of long-ranged interactions. Then we will use these expressions to derive force and stress estimators. Our major contribution is the generalization of the preexisting Chiesa force estimator to bulk systems and the generalization of the Nielsen-Martin method of computing stresses to construct a QMC stress estimator. After validating these with numerical experiments, I return to the particulars of treating long-ranged interactions in periodic systems. We review the existing methods of treating long-range interactions for energies and forces. We then present our new method of calculating long-ranged contributions to stress tensor components.

6.2 Periodic Boundary Conditions

Long-range interactions require delicate care in the handling of periodic boundary conditions. This is because each particle sees and interacts with an infinite lattice made up of copies of the unit cell. We will assume for now that our unit cell is specified by primitive vectors $\{\mathbf{a}_1, \mathbf{a}_2, \mathbf{a}_3\}$ and has a volume Ω. The set of lattice points $\{\mathbf{L}\}$, is built up from the primitive vectors in the usual manner:

$$\{\mathbf{L}\} = \{n_1\mathbf{a}_1 + n_2\mathbf{a}_2 + n_3\mathbf{a}_3 | n_1, n_2, n_3 \in \mathbb{Z}\} \tag{6.1}$$

This also generates a reciprocal lattice, which is similarly defined as:

$$\{\mathbf{G}\} = \{n_1\mathbf{b}_1 + n_2\mathbf{b}_2 + n_3\mathbf{b}_3 | n_1, n_2, n_3 \in \mathbb{Z}\} \tag{6.2}$$

Lattice vectors and reciprocal lattice vectors satisfy the relation $\mathbf{a}_i \cdot \mathbf{b}_j = 2\pi\delta_{ij}$.

In Chapter 2, we specified the general Coulomb Hamiltonian. For now, lets represent an arbitrary pair-wise interaction between particles of species α and β as $v^{\alpha\beta}(\mathbf{r})$. Using periodic boundary conditions, we write the potential energy for a unit cell interacting with an infinite lattice of identical copies of itself as:

$$V = \frac{1}{2}\sum_{\alpha}\sum_{i_\alpha \neq j_\alpha}\sum_{\mathbf{L}} v^{\alpha\alpha}(|\mathbf{r}^\alpha_{i_\alpha} - \mathbf{r}^\alpha_{j_\alpha} + \mathbf{L}|) + \sum_{\alpha<\beta}\sum_{i_\alpha, j_\beta}\sum_{\mathbf{L}} v^{\alpha\beta}(|\mathbf{r}^\alpha_{i_\alpha} - \mathbf{r}^\beta_{j_\beta} + \mathbf{L}|) + \sum_{\alpha}\sum_{|\mathbf{L}|\neq 0} N^\alpha v^{\alpha\alpha}(|\mathbf{L}|) \tag{6.3}$$

We have implicitly made the split between same-species (homologous) and different-species (heterologous) terms.

Even though $v^{\alpha\beta}(|\mathbf{r}_i - \mathbf{r}_j|)$ is in general not periodic, the use of periodic boundary conditions yields a periodic potential function $v^{\alpha\beta}_{\mathbf{P}}(\mathbf{r}_i - \mathbf{r}_j)$ expressible as follows:

$$v^{\alpha\beta}_{\mathbf{P}}(\mathbf{r}) = \sum_{\mathbf{L}} v^{\alpha\beta}(|\mathbf{r} + \mathbf{L}|) \tag{6.4}$$

As such, $v^{\alpha\beta}_{\mathbf{P}}(\mathbf{r})$ can be represented as a discrete Fourier series. We define the Fourier transform pair relating $v(r)$ to $v_{\mathbf{G}}$ as follows:

$$v^{\alpha\beta}_{\mathbf{G}} = \frac{1}{\Omega}\int d\mathbf{r} v^{\alpha\beta}(\mathbf{r}) e^{-i\mathbf{G}\cdot\mathbf{r}} \tag{6.5}$$

$$v^{\alpha\beta}_{\mathbf{p}}(\mathbf{r}) = \sum_{\mathbf{G}} v^{\alpha\beta}_{\mathbf{G}} e^{i\mathbf{G}\cdot\mathbf{r}} \tag{6.6}$$

We also take this opportunity to define the Fourier transform of the particle density for a species α:

$$\rho^\alpha_{\mathbf{G}} = \sum_{i_\alpha=0}^{N_\alpha - 1} e^{-i\mathbf{G}\cdot\mathbf{r}_{i_\alpha}} \tag{6.7}$$

Immediately using either $v^{\alpha\beta}_{\mathbf{p}}(r)$ or $v^{\alpha\beta}_{\mathbf{G}}$ to express Eq. 6.3 suffers from the fact that sums over long-ranged potentials are slowly convergent when done entirely in real space or Fourier space. However, convergence can be dramatically accelerated if $v^{\alpha\beta}_{\mathbf{P}}(\mathbf{r})$ is split into long-range and short-range pieces: $v^{\alpha\beta}_{\mathbf{P}}(\mathbf{r}) = \sum_{\mathbf{L}} \sigma^{\alpha\beta}(|\mathbf{r} + \mathbf{L}|) + \sum_{\mathbf{G}} \Lambda^{\alpha\beta}_{\mathbf{G}} e^{i\mathbf{G}\cdot\mathbf{r}}$. Here, $\sigma^{\alpha\beta}(r)$ is a short-ranged function with a cutoff of r_c, and $\Lambda^{\alpha\beta}_{\mathbf{G}}$ is a long-ranged function expressed in Fourier space with a cutoff of k_c. This decomposition is possible because of the Ewald

and "optimized breakup" schemes, which will be discussed later.

To spare a lengthy rederivation of the potential energy term, we present the general result from reference [92]. This formula is obtained by introducing compensating uniform background charges for each species α. It is valid not only for neutral coulomb systems, but also for charged systems interacting with pseudopotentials.

$$
\begin{aligned}
V &= \sum_{\alpha} \sum_{i_\alpha < j_\alpha} \sigma^{\alpha\alpha}(|\mathbf{r}_{i_\alpha} - \mathbf{r}_{j_\alpha}|) + \sum_{\alpha} \sum_{\mathbf{G}\neq 0} \Lambda^{\alpha\alpha}_{\mathbf{G}} |\rho^{\alpha}_{\mathbf{G}}|^2 && (6.8)\\
&+ \sum_{\alpha<\beta} \sum_{i_\alpha, j_\beta} \sigma^{\alpha\beta}(|\mathbf{r}_{i_\alpha} - \mathbf{r}_{j_\beta}|) + \sum_{\alpha<\beta} \sum_{\mathbf{G}\neq 0} \Lambda^{\alpha\beta}_{\mathbf{G}} \Re(\rho^{\alpha}_{-\mathbf{G}} \rho^{\beta}_{\mathbf{G}}) && (6.9)\\
&+ \frac{1}{2} \sum_{\alpha} \left[(N^{\alpha})^2 (\Lambda^{\alpha\beta}_{\mathbf{G}=0} - \sigma^{\alpha\alpha}_{G=\mathbf{0}}) - N_\alpha \Lambda^{\alpha\alpha}(0) \right] && (6.10)\\
&+ \sum_{\alpha,\beta} N^{\alpha} N^{\beta} \left[\Lambda^{\alpha\beta}_{\mathbf{G}=0} - \sigma^{\alpha\beta}_{G=\mathbf{0}} \right] && (6.11)
\end{aligned}
$$

The first two lines are the heterologous and homologous terms respectively. The last two lines are terms arising from the introduction of neutralizing background terms and residual $\mathbf{G} = 0$ contributions. The terms $\sigma^{\alpha\beta}_{\mathbf{G}=0}$, $\Lambda^{\alpha\beta}_{\mathbf{G}=0}$, and $\Lambda^{\alpha\beta}(0)$ are defined respectively as:

$$
\begin{aligned}
\sigma^{\alpha\beta}_{\mathbf{G}=0} &= \frac{4\pi}{\Omega} \int_0^{r_c} dr r^2 \sigma^{\alpha\beta}(r) && (6.12)\\
\Lambda^{\alpha\beta}_{\mathbf{G}=0} &= \frac{4\pi}{\Omega} \int_0^{r_c} dr r^2 \Lambda^{\alpha\beta}(r) && (6.13)\\
\Lambda^{\alpha\beta}(0) &= v^{\alpha\beta}(0) - \sigma^{\alpha\beta}(0) && (6.14)
\end{aligned}
$$

6.3 Force Estimators

6.3.1 Theory

The Hellmann-Feynman theorem [93] states that if a system is in a state $|\Psi\rangle$ which is a variational minimum of $\hat{H}$, and if there is no explicit dependence of $|\Psi\rangle$ on a parameter λ, then the derivative of the energy of a system with respect to λ is given by:

$$
\frac{\partial E}{\partial \lambda} = \frac{\langle \Psi | \frac{\partial \hat{H}}{\partial \lambda} | \Psi \rangle}{\langle \Psi | \Psi \rangle} \tag{6.15}
$$

We can use this to calculate the force on ion p_α of species α with the following:

$$
\mathbf{F}_{p_\alpha} = \frac{\langle \Psi | - \nabla_{p_\alpha} \hat{H} | \Psi \rangle}{\langle \Psi | \Psi \rangle} \tag{6.16}
$$

This is true provided that $|\Psi\rangle$ is optimized with VMC. Additionally, while in general we cannot exclude explicit dependencies of $|\Psi\rangle$ on the ionic coordinates $\mathbf{R}$, the use of a plane-wave basis set common in bulk calculations eliminates this explicit dependence. We will only consider such types of wave functions in this work.

Assuming the nuclei are fixed, the kinetic energy term in $\hat{H}$ has no dependence on the ionic coordinates, leaving $-\nabla_{p_\alpha}\hat{H} = -\nabla_{p_\alpha}V$. We can calculate this explicitly using Eq. 6.8.

It is useful to decompose the total force on ion p of species α as $\mathbf{f}_{p_\alpha} = \mathbf{f}^I_{p_\alpha} + \mathbf{f}^e_{p_\alpha}$. The ionic contribution to the force, $\mathbf{f}^I_{p_\alpha}$, is computed in one shot at the beginning of the simulation. The electron-ion contribution is given by

$$\mathbf{f}^e_{p_\alpha} = \frac{\langle\Psi|\sum_{i_e}\frac{d}{dr}\sigma^{\alpha e}(|\mathbf{r}_{i_e}-\mathbf{R}_{p_\alpha}|)\frac{\mathbf{r}_{i_e}-\mathbf{R}_{p_\alpha}}{|\mathbf{r}_{i_e}-\mathbf{R}_{p_\alpha}|} + \sum_{\mathbf{G}\neq 0}\Lambda^{\alpha\beta}_{\mathbf{G}}\Im\left(e^{i\mathbf{G}\cdot\mathbf{R}_{p_\alpha}}\rho^e_{\mathbf{G}}\right)\mathbf{G}|\Psi\rangle}{\langle\Psi|\Psi\rangle} \tag{6.17}$$

Monte Carlo sampling the above expression suffers from a fatal flaw. The magnitude of the short-range real space force has a $1/r^2$ divergence as $r \to 0$. This means that while the mean of this part of the estimator exists, the variance is infinite. The long range contribution is smooth and has no such problem. One solution to this problem used here follows the Chiesa, Ceperley, Zhang scheme [94]. Though this technique was originally developed for bare coulomb potentials in open boundary conditions, we note the that derivation is general as long as the radially symmetric potential is continuous. Consider the expression for the total force on an ion located at the origin.

$$\mathbf{f} = \int d^3\mathbf{r}\rho(\mathbf{r})h(r)\frac{\mathbf{r}}{r} \tag{6.18}$$

In the original derivation, $h(r) = Z/r^2$. In our case, $h(r) = \frac{d}{dr}\sigma(r) = Zw(r)/r^2$. To recover the short-ranged behavior of the electron-ion coulomb force term, $w(r) \to 1$ as $r \to 0$, and $w(r) \to r^3$ as $r \to r_c$. The latter condition stems from the fact that the short-ranged force magnitude should be constructed to smoothly go to zero outside a radius of r_c. Given these conditions, the arguments for the force density $f_z(r) \propto r$ as $r \to 0$ by the constraint that $\rho(r)$ be a physically reasonable density still holds. The reader is invited to verify that the derivation of the filtering function $g(r)$ in this paper remains unchanged with the substitution $Z/r^2 \to Zw(r)/r^2$. Thus, we can apply the Chiesa filtering scheme without modification to the short-range force terms to fix the divergence. Taking the operator between $\langle\Psi|\ldots|\Psi\rangle$ in Eq. 6.3.1 and applying the Chiesa correction yields the following finite-variance operator $\hat{\mathbf{f}}^e_{p_\alpha}$:

	Finite Diff	Chiesa	ΔF
f_x^e	-0.3260(27)	-0.3244(16)	-0.0016(31)
f_y^e	0.0997(27)	0.0953(24)	0.0044(34)
f_z^e	0.2840(28)	0.2832(18)	0.0008(33)

Table 6.1: VMC Electron-ion force $\mathbf{f}^e$ computed using the Chiesa-Ceperley-Zhang estimator and finite-differencing of local energy. The two agree to within the somewhat large error bars.

$$\hat{\mathbf{f}}^e_{p_\alpha} = \sum_{i_e} g(|\mathbf{r}_{i_e} - \mathbf{R}_{p_\alpha}|) \frac{d}{dr}\sigma^{\alpha e}(|\mathbf{r}_{i_e} - \mathbf{R}_{p_\alpha}|) \frac{\mathbf{r}_{i_e} - \mathbf{R}_{p_\alpha}}{|\mathbf{r}_{i_e} - \mathbf{R}_{p_\alpha}|} + \sum_{\mathbf{G}\neq 0} \Lambda^{\alpha\beta}_{\mathbf{G}} \Im\left(e^{i\mathbf{G}\cdot\mathbf{R}_{p_\alpha}} \rho^e_{\mathbf{G}}\right) \mathbf{G} \tag{6.19}$$

From the original paper [94], $g(r) = \theta(\mathcal{R} - r)\sum_{k=1}^{M} c_k r^{k+m}$, where c_k is given by $\mathbf{c} = \mathbf{S^{-1}h}$. $\mathcal{R}$ is a real-space cutoff, and M specifies the degree of the smoothing polynomial. $\mathbf{S}$ and $\mathbf{h}$ are given by:

$$S_{kj} = \frac{\mathcal{R}^{m+k+j+1}}{m+k+j+1} \tag{6.20}$$

$$h_j = \frac{\mathcal{R}^{j+1}}{j+1} \tag{6.21}$$

6.3.2 Validation

To test the validity of both the Chiesa correction and our long-range implementation, we considered a snapshot from a liquid hydrogen simulation performed at T=1000K using the vdW-DF2 functional. The system had 54 hydrogen atoms at a density of r_s=1.60a_0. We chose an atom in this system and computed all three force components by using a three-point finite-difference formula. The step size was chosen to be $\Delta = 0.001a_0$. The energy differences required were computed using correlated sampling within VMC. We then computed the force components using the Chiesa estimator, also within VMC. We used $\mathcal{R} = 1.0a_0$ and $n = 3$ to specify the estimator. We used the optimized breakup scheme for forces described in Section 6.5.2 with $k_c r_c = 15$, and r_c taken to be half the box length.

In Table 6.1, we compare the electron-ion component of the force on an atom computed via the Chiesa estimator and our finite-difference formula. We find that to within error bars, the Chiesa correction agrees with the finite-difference results. From previous plane-wave calculations we did with isolated H_4 molecules in very large simulation boxes ($L = 20a_0$), we found a sensitivity in the calculated force components to the density of the real space grid used to represent the density. This was found to be as large as $2mHa/a_0$. This is not a theoretical problem with the estimator so much as it is a documented sensitivity of the estimator to the representation of the charge density close to atoms.

6.4 Stress Estimator

6.4.1 Theory

Consider an infinitesimal deformation of our unit cell. This is equivalent to a transformation of all particle coordinates $\mathbf{r}$, given by $\mathbf{r}' = (\mathbf{I} + \boldsymbol{\varepsilon})\mathbf{r}$. $\mathbf{I}$ is the 3×3 identity matrix and $\boldsymbol{\varepsilon}$ is a symmetric matrix known as the "strain tensor". This transformation affects a similar transformation on vectors in reciprocal space: $\mathbf{G}' = (\mathbf{I} - \boldsymbol{\varepsilon})\mathbf{G}$. The stress tensor $\boldsymbol{\sigma}$ is defined in terms of the above as follows:

$$\sigma_{\mu\nu} = -\frac{1}{\Omega}\frac{\partial E}{\partial \varepsilon_{\mu\nu}} \tag{6.22}$$

To calculate this expression, Nielsen and Martin [95] considered calculating the energy expectation value of an arbitrary wave function $|\Psi_\varepsilon\rangle$, obtained by making the strained coordinate transformation $\Psi_\varepsilon(\mathbf{r}'_0, \ldots, \mathbf{r}'_N) = \Psi((\mathbf{I} + \boldsymbol{\varepsilon})^{-1}\mathbf{r}_0, \ldots, (\mathbf{I} + \boldsymbol{\varepsilon})^{-1}\mathbf{r}_N)$. By writing out $|\Psi_\varepsilon\rangle$ as a Taylor expansion in terms of the various strain components, one finds that:

$$\frac{\partial \langle H \rangle_{|\Psi|^2}}{\partial \varepsilon_{\mu\nu}} = \langle \Psi | \frac{1}{2} \sum_i^{N_e} \partial_i^\mu \partial_i^\nu + \frac{\partial V}{\partial \varepsilon_{\mu\nu}} | \Psi \rangle \tag{6.23}$$

The strain derivative of the potential is dealt with using the chain rule. The particle coordinates, reciprocal space vectors, and the volume are all subject to explicit changes under strain deformations. For an arbitrary function $f(r)$ depending on the magnitude of a vector $\mathbf{r}$, and for an arbitrary function $g(G, \Omega)$ depending on the magnitude of a reciprocal space vector $\mathbf{G}$ and total system volume Ω, the strain derivatives are given by.

$$\frac{\partial}{\partial \varepsilon_{\mu\nu}} f(r) = \frac{r_\mu r_\nu}{r}\frac{\partial f}{\partial r} \tag{6.24}$$

$$\frac{\partial}{\partial \varepsilon_{\mu\nu}} g(G, \Omega) = -\frac{G_\mu G_\nu}{G}\frac{\partial g}{\partial G} + \delta_{\mu\nu}\Omega\frac{\partial g}{\partial \Omega} \tag{6.25}$$

We write the stress tensor as a sum:

$$\boldsymbol{\sigma} = \boldsymbol{\sigma}_{kinetic} + \boldsymbol{\sigma}_{SR} + \boldsymbol{\sigma}_{LR} + \boldsymbol{\sigma}_{BG} \tag{6.26}$$

The sum on the right represent the kinetic, short-ranged, long-ranged, and background contributions to the

total stress tensor.

$$\boldsymbol{\sigma}_{kinetic} = \frac{1}{\Omega}\sum_{\alpha}\sum_{i_\alpha}^{N_\alpha} -\frac{1}{2}\nabla_{i_\alpha}\otimes\nabla_{i_\alpha} \tag{6.27}$$

$$\boldsymbol{\sigma}_{SR} = \frac{1}{\Omega}\sum_{\alpha<\beta}\sum_{i_\alpha,j_\beta}\frac{(\mathbf{r}_{i_\alpha}-\mathbf{r}_{j_\alpha})\otimes(\mathbf{r}_{i_\beta}-\mathbf{r}_{j_\beta})}{|\mathbf{r}_{i_\alpha}-\mathbf{r}_{j_\beta}|}\frac{\partial}{\partial r}\sigma^{\alpha\beta}(|\mathbf{r}_{i_\alpha}-\mathbf{r}_{j_\beta}|) + \text{homologous} \tag{6.28}$$

$$\boldsymbol{\sigma}_{LR} = \frac{1}{\Omega}\sum_{\alpha<\beta}\sum_{\mathbf{G}\neq 0}\left(\frac{\mathbf{G}\otimes\mathbf{G}}{G}\frac{\partial\Lambda^{\alpha\beta}_{\mathbf{G}}}{\partial G} - \mathbf{I}\Omega\frac{\partial\Lambda^{\alpha\beta}_{\mathbf{G}}}{\partial\Omega}\right)\Re(\rho^{\alpha}_{-\mathbf{G}}\rho^{\beta}_{\mathbf{G}}) + \text{homologous} \tag{6.29}$$

$$\boldsymbol{\sigma}_{BG} = \frac{1}{\Omega}\mathbf{I}\sum_{\alpha,\beta}N^{\alpha}N^{\beta}\left[\Lambda^{\alpha\beta}_{\mathbf{G}=0} - \sigma^{\alpha\beta}_{G=\mathbf{0}}\right] \tag{6.30}$$

The "homologous" terms are formally identical to the "heterlogous" terms, except they include a factor of $1/2$ and exclude self-interactions.

Since the reciprocal space terms are smooth, the remaining place where we might have an infinite-variance problem is in Eq. 6.29. In contrast to the force estimator, the term involving $\frac{\partial}{\partial r}\sigma(r)$ is multiplied by $r_\mu r_\nu/r$, which when integrated contributes a net factor of r to $\frac{\partial}{\partial r}\sigma(r)$. This term will thus diverge like the potential energy term, and therefore has finite variance. This argument can be made more rigorous by performing integrals similar to those found in Eq. 6.42.

6.4.2 Validation

The above estimator was implemented initially using the Ewald method described in section 6.5.1. After calculating the stress tensor in a simple BCC system by finite differencing, and finding that the error on both the off-diagonal and diagonal components could be made arbitrarily small by increasing k_c, we tested the stress tensor on a more complex system. We chose a disordered snapshot of pure liquid hydrogen with $N_H = 54$ and at a density of r_s=1.60a_0. The expectation value for each component was computed with both VMC and DMC. We also computed the same estimates using a $2\times2\times2$ supercell, which allowed us to calculate finite-size corrections. Twist-averaging was done on a $3\times3\times3$ offset Monkhorst-Pack grid in the unit cell, and $2\times2\times2$ grid in the supercell. Finite size corrections are discussed at length in Chapter 7.

In Table 6.2, we show the twist-averaged QMC stress tensor (in GPa) obtained using the extrapolated estimate $\sigma^{EXT}_{\mu\nu} = 2\sigma^{DMC}_{\mu\nu} - \sigma^{VMC}_{\mu\nu}$. These results are not finite-size corrected. We also show the stress tensors computed using fully converged DFT calculations based on the PBE, vdW-DF, vdW-DF2, and HSE functionals. We find that the QMC stress tensor is roughly in agreement with the different DFT approximations, especially concerning the anisotropy seen on the diagonal and the magnitudes of the off-diagonal components. However, we find that σ_{zz} in particular is noticeably lower than all DFT estimates,

(GPa)	QMC	err	LDA	PBE	vdW-DF	vdW-DF2	HSE
σ_{xx}	78.29	0.16	81.42	86.79	93.16	96.06	79.97
σ_{yy}	76.88	0.16	78.66	84.30	91.00	94.20	75.99
σ_{zz}	114.32	0.14	127.93	127.08	127.34	127.16	126.19
σ_{xy}	3.97	0.12	6.20	4.76	3.32	2.60	6.71
σ_{xz}	-3.67	0.11	-2.04	-2.84	-3.84	-4.42	-1.59
σ_{yz}	-1.46	0.11	-1.56	-1.56	-1.38	-1.29	-2.82

Table 6.2: QMC stress tensor (Column 2) compared against DFT stress tensors computed using different functionals (Column 3-8).

(GPa)	Finite Size Correction
σ_{xx}	-1.70
σ_{yy}	-3.10
σ_{zz}	16.28
σ_{xy}	2.17
σ_{xz}	1.43
σ_{yz}	1.38

Table 6.3: Finite size corrections for QMC stress tensor obtained from 1/N extrapolation.

indicating a likely bias. Under the assumption that the bias is from finite size effects, we computed the finite size corrections for each component via 1/N extrapolation. We used extrapolated, twist-averaged stress components from our unit cell and a 2x2x2 supercell to compute the corrections, which we show in Table 6.3.

After adding the finite-size corrections to the QMC data, we computed the relative error of the different DFT stress tensor components relative to QMC. We present these numbers in Figure 6.4. We see that LDA and HSE have strong agreement with the QMC numbers. Encouragingly, there does not appear to be the same systematic bias as observed before adding the finite-size corrections. Additionally, as we will see in upcoming DFT benchmarking chapters, magnitudes of the DFT errors for both the diagonal and off-diagonal stress tensor elements exhibit the same patterns observed for the pressure. Namely, HSE and LDA will be found to produce the best estimates of the pressure, with PBE, vdW-DF, and vdW-DF2 getting progressively worse in that order.

(% Error)	LDA	PBE	vdW-DF	vdW-DF2	HSE
σ_{xx}	6.31	13.32	21.64	25.43	4.42
σ_{yy}	6.61	14.24	23.33	27.67	-2.98
σ_{zz}	-2.05	-2.70	-2.50	-2.64	-3.38
σ_{xy}	0.94	-22.47	-45.95	-57.70	9.36
σ_{xz}	-8.90	26.90	71.54	97.28	-28.97
σ_{yz}	-40.72	-45.11	-51.22	-54.65	-0.64

Table 6.4: Relative error of DFT stress tensor components to finite-size corrected QMC stress tensor components.

6.5 Breakup Schemes

In the previous sections, we laid out the formal expressions for the potential energy, force, and stress, based on the assumption of a decomposition of the long-range potential $v^{\alpha\beta}(r)$. In this section, we provide a discussion of the Ewald and optimized breakup schemes. We henceforth suppress the species indices on $v^{\alpha\beta}(r)$, $\sigma^{\alpha\beta}(r)$, and $\Lambda^{\alpha\beta}(r)$ for notational simplicity.

6.5.1 Ewald

The Ewald method is the most widely used approach to breaking up long-ranged potentials [82]. This works by adding a Gaussian screening charge distribution to each point particle in real space, and subtracting it out in reciprocal space. The standard deviation of the Gaussian distribution is defined to be η, which determines how localized $\sigma(r)$ or $\Lambda_{\mathbf{G}}$ are in real and reciprocal space respectively. This yields the following terms for the short and long range components:

$$\sigma(r) = \frac{1-\text{erf}(\eta r)}{r} \tag{6.31}$$

$$\Lambda_{\mathbf{G}} = \frac{4\pi}{\Omega}\frac{\exp(-\frac{-G^2}{4\eta^2})}{G^2} \tag{6.32}$$

$$\sigma_{\mathbf{G}=0} = \frac{\pi}{\eta^2\Omega} \tag{6.33}$$

$$\Lambda(0) = \frac{2\eta}{\sqrt{\pi}} \tag{6.34}$$

Typically, η is chosen to ensure the short-range piece decays sufficiently at $L/2$.

6.5.2 Optimized Breakup

The other approach one can take is the "optimized breakup" scheme [96, 92]. While the technical machinery is far more involved than Ewald, the advantage is that the error in the breakup can be orders of magnitude lower than the Ewald scheme for the same reciprocal space cutoff k_c. In this section, we present the major formulas used to calculate the optimized breakup for energies and forces, and then generalize the procedure to stresses.

To perform the optimized breakup for energies, we define an energy χ^2 function as follows:

$$\chi_E^2 = \int d\mathbf{r}|v_{\mathbf{p}}(\mathbf{r}) - v_a(\mathbf{r})|^2 \tag{6.35}$$

Here, $v_{\mathbf{p}}(\mathbf{r})$ is the exact periodic potential, and $v_a(\mathbf{r}) = \sigma(r) + \sum_{|\mathbf{G}|\leq k_c}\Lambda_{\mathbf{G}}e^{i\mathbf{G}\cdot\mathbf{r}}$ is our approximation to it.

The optimized breakup procedure works by parameterizing either $\sigma(r)$ or $\Lambda(r)$ as a linear combination of M basis functions $\{h_0(r), h_1(r), h_{M-1}(r)\}$ [96, 92]. We choose the convention of Natoli for all implementations in this work, whereby we represent the short-ranged function $\sigma(r)$ as $\sigma(r) = g(r)/r$ with $g(r) = \sum_n t_n h_n(r)$. We used the LPQHI interpolating basis functions for $h_n(r)$ [96]. To recover the Coulomb singularity as $r \to 0$, we demand that $g(0) = 1$ and $g'(0) = g''(0) = 0$. To implement a smooth cutoff such that $\sigma(r) = 0$ when $r \geq r_c$, we demand that $g(r_c) = g'(r_c) = g''(r_c) = 0$.

Define $c_{n\mathbf{G}}$ as the Fourier transform of $h_n(r)$. Letting $\Lambda_{\mathbf{G}} = v_{\mathbf{G}} - \sum_{n=0}^{M} t_n c_{n\mathbf{G}}$, we can write Eq. 6.35 in reciprocal space as:

$$\chi_E^2 = \int d\mathbf{r}(\sum_{|\mathbf{G}|>k_c} e^{i\mathbf{G}\cdot\mathbf{r}}(v_{\mathbf{G}} - \sum_{n=0}^{M-1} t_n c_{n\mathbf{G}}))^2 \tag{6.36}$$

Minimizing the above w.r.t. the t_n coefficients yields the following system of equations, which can be solved by a singular value decomposition (SVD)[40]:

$$\sum_{m=0}^{M-1} \sum_{|\mathbf{G}|\geq k_c} c_{m\mathbf{G}} c_{n\mathbf{G}} t_n = \sum_{|\mathbf{G}|\geq k_c} v_{\mathbf{G}} c_{n\mathbf{G}} \tag{6.37}$$

One can show that the mean square error χ_E^2 is given explicitly by $\chi_E^2 = \sum_{|\mathbf{G}|>k_c} |v_{\mathbf{G}} - \sum t_n c_{n\mathbf{G}}|^2$.

For forces, it was shown that the correct optimized breakup scheme is to minimize the following integral with respect to the t_n coefficients:

$$\chi_F^2 = \int d\mathbf{r} |\nabla v_{\mathbf{p}}(\mathbf{r}) - \nabla v_a(\mathbf{r})|^2 \tag{6.38}$$

This yields the following system of equations:

$$\sum_{m=0}^{M-1} \sum_{|\mathbf{G}|\geq k_c} G^2 c_{m\mathbf{G}} c_{n\mathbf{G}} t_n = \sum_{|\mathbf{G}|\geq k_c} G^2 v_{\mathbf{G}} c_{n\mathbf{G}} \tag{6.39}$$

The corresponding error is given by $\chi_F^2 = \sum_{|\mathbf{G}|>k_c} G^2 |v_{\mathbf{G}} - \sum t_n c_{n\mathbf{G}}|^2$.

For stresses, the picture more complicated. Trying to use the above expressions to calculate off-diagonal elements of the stress tensor show that it is orders of magnitude more accurate than Ewald when using the same reciprocal space cutoff k_c. However, the diagonal elements fail to converge before the SVD decomposition suffers from numerical instabilities. The source of this error stems from the poor representation of $\frac{\partial \Lambda_{\mathbf{G}}}{\partial G}$ which plays a big part in calculating the stress tensor, but is absent from force and energy calculations. One can attempt to minimize $|\frac{\partial}{\partial \varepsilon_{\mu\nu}} v_{\mathbf{p}}(\mathbf{r}) - \frac{\partial}{\partial \varepsilon_{\mu\nu}} v_a(\mathbf{r})|^2$. We opted against this approach, since the equations are complex and different optimized breakup routines are required for the diagonal and off-diagonal elements. A

simplification comes from noting that in both Ewald and optimized breakup methods, the only explicit volume dependence in the long-range piece $\Lambda_{\mathbf{G}}$ comes from the $\frac{1}{\Omega}$ factor in the Fourier transform (see Eq. 6.6). When used in conjunction with Eq. 6.25, the explicit volume contribution to the strain tensor is $\delta_{\mu\nu}\Lambda_{\mathbf{G}}$. But this is recognized as the long-range part of the potential, allowing us to use the energy optimized breakup for this piece. This is almost always on-hand already, since we need it to calculate the total energy. For the remaining terms involving $\mathbf{r}\otimes\mathbf{r}/r$ and $\mathbf{G}\otimes\mathbf{G}/G$ in Eq. 6.27, we define the following $\chi^2_{\sigma_{\mu\nu}}$ function that needs to be minimized:

$$\chi^2_{\sigma_{\mu\nu}} = \int d\mathbf{r}\left[\sum_{|\mathbf{G}|>k_c} e^{i\mathbf{G}\cdot\mathbf{r}}\frac{G_\mu G_\nu}{G}\left(\frac{\partial v_{\mathbf{G}}}{\partial G} - \sum_{n=0}^{M-1} t_n \frac{\partial c_{n\mathbf{G}}}{\partial G}\right)\right]^2 \tag{6.40}$$

One can show that this leads to the following linear system of equations that must be solved for t_n:

$$\sum_{|\mathbf{G}|\geq k_c}\sum_{m=0}^{M-1}\frac{G_\mu^2 G_\nu^2}{G^2}\frac{\partial c_{m\mathbf{G}}}{\partial G}\frac{\partial c_{n\mathbf{G}}}{\partial G}t_n = \sum_{|\mathbf{G}|\geq k_c}\frac{G_\mu^2 G_\nu^2}{G^2}\frac{v_{\mathbf{G}}}{\partial G}\frac{\partial c_{n\mathbf{G}}}{\partial G} \tag{6.41}$$

The dependence on μ and ν is a bit troubling, but we can simplify this expression in the following manner. Since $v_{\mathbf{G}}$ and $c_{n\mathbf{G}}$ are spherically symmetric in reciprocal space, one can verify that reciprocal space integrals obey the following identities. If $f(G)$ is an arbitrary spherically symmetric function of G, and if $\mu\neq\nu$, then:

$$\int d\mathbf{G}\frac{G_\mu^2 G_\nu^2}{G^2}f(G) = \frac{1}{15}\int d\mathbf{G}G^2 f(G) \tag{6.42}$$

If $\mu=\nu$, we have instead the following expression:

$$\int d\mathbf{G}\frac{G_\mu^2 G_\mu^2}{G^2}f(G) = \frac{1}{5}\int d\mathbf{G}G^2 f(G) \tag{6.43}$$

Assuming that k_c is large enough that the summation can be approximated by an integral, we use both these identities to approximate the diagonal and off-diagonal breakup equations in Eq. 6.41:

$$\sum_{|\mathbf{G}|\geq k_c}\sum_{m=0}^{M-1}G^2\frac{\partial c_{m\mathbf{G}}}{\partial G}\frac{\partial c_{n\mathbf{G}}}{\partial G}t_n = \sum_{|\mathbf{G}|\geq k_c}G^2\frac{v_{\mathbf{G}}}{\partial G}\frac{\partial c_{n\mathbf{G}}}{\partial G} \tag{6.44}$$

Notice how the equations for diagonal and off-diagonal stress tensor elements are identical now. Insofar as we can approximate the sum in the above as an integral, the approximate error formula is given by:

$$\chi^2_\sigma = \sum_{|\mathbf{G}|>k_c} G^2\left|\frac{\partial v_{\mathbf{G}}}{\partial G} - \sum_n t_n\frac{c_{n\mathbf{G}}}{\partial G}\right|^2 \tag{6.45}$$

We use the t_n from this fit to calculate $\frac{\partial}{\partial r}\sigma(r)$, $\frac{\partial}{\partial G}\Lambda_{\mathbf{G}}$, and $\sigma_{\mathbf{G}=0}$. $\Lambda_{\mathbf{G}}$ is still computed with the optimized breakup for energy.

To verify that this optimized breakup approach works, we measured the ion-ion contribution to the stress in a disordered pure hydrogen system with $N_H = 64$ and r_s=1.34a_0. The ion-ion contribution was chosen because it can be quickly calculated up to machine precision, and is also calculated in other codes. We calculated reference values using the Ewald method, using $\eta = 4.5r_c$ and $r_c k_c = 80.0$. Then we computed the stress component error $\Delta\sigma_{\mu\nu}$ as $k_c r_c$ is varied. We show these results in Figure 6.1.

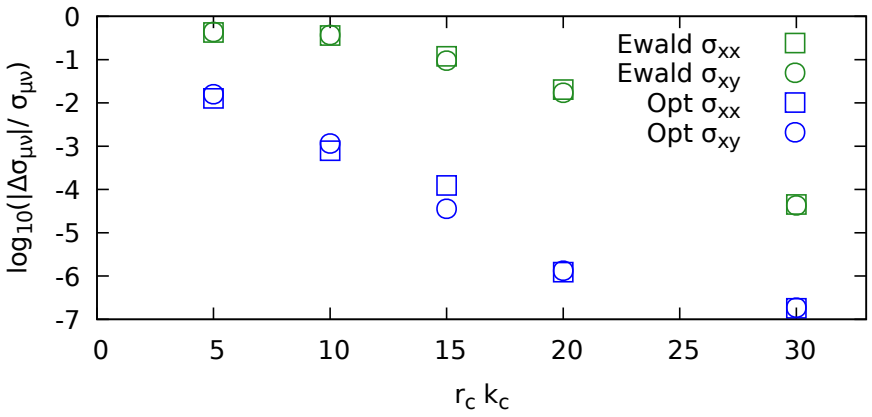

Figure 6.1: Plot of $\log_{10}(\Delta\sigma_{\mu\nu}/\sigma_{\mu\nu})$ as a function of $k_c r_c$ for both the Ewald and optimized breakup methods. Data for the σ_{xx} and σ_{xy} components are included, which represent diagonal and off-diagonal components. We note that the optimized breakup has orders of magnitude lower errors than Ewald for both stress components.

From the figure, we see that the optimized breakup scheme is approximately 2 orders of magnitude more accurate than Ewald at $k_c r_c = 5$. Increasing the reciprocal space cutoff, we see that the optimized breakup has a steeper slope than Ewald (at keast to around $r_c k_c = 30$). This indicates that in addition to the total error being lower with the optimized breakup scheme, it also converges faster than Ewald. The practical side of this is that one can use reciprocal-space cutoffs which are at least 2 times smaller than Ewald to achieve the same accuracy. Since the computational cost of computing the reciprocal space sum in Eq. 6.27 scales like $O(k_c^3)$, this amounts to at least a factor of 8 savings over Ewald to compute the stress tensor to a given accuracy.

The major disadvantage of the optimized breakup scheme stems from the solution of the system of equations. First, there is some overhead associated with building the matrices found in Eq. 6.37. Using spherical symmetry in reciprocal space can drop this cost to $O(k_c)$. Secondly, the condition number of these matrices become large as k_c is increased. Eventually, increasing k_c past a certain point will cause the SVD

method to zero out some nearly singular values, which will kill the accuracy of the fit [40]. This is manifested by a sudden jump in χ^2. This is not an issue for realistic calculations, as the method almost always converges to required accuracy well before numerical instabilities come into play.

6.6 Future Work

The stress estimator in its current form works. However, it suffers from a mixed estimator problem that cannot at the moment be solved by using RMC or forward-walking schemes. The problem arises from the $\boldsymbol{\sigma}_{kinetic}$ term. As a stopgap measure, one can feasibly perform RMC on the remaining contributions of the stress tensor and then use extrapolated estimates for the kinetic energy term. As a more general fix, it would be instructive to consider constructing Assaraf-Caffarel "zero-variance zero-bias" estimators for the stress [97]. This would require explicit computation $\frac{\partial}{\partial \varepsilon_{\mu\nu}}|\Psi_T\rangle$ and its Laplacian. Simpler but closely related estimators for the pressure have been developed and tested in the homogeneous electron gas [98].

In extending both the force and stress estimators to pseudopotential calculations, it would be desirable to rederive the above optimized breakup scheme when the interpolating function $\sum_m t_m h_m(r)$ is used to parameterize the long-range potential $\Lambda(r)$ [92]. Pseudopotentials will often eliminate the $1/r$ divergence, which means that we would have to use different basis functions $h_n(r)$ depending on whether we were performing all-electron or pseudopotential calculations. Such a reformulation would treat both cases on an equal footing.

Chapter 7

Finite-Size Effects

7.1 Introduction

In the previous chapter, we discussed how to evaluate energies, forces, and stresses in systems subject to periodic boundary conditions. The ultimate goal of these calculations is to estimate the properties of systems in the thermodynamic limit, or as $N \to \infty$ and $\Omega \to \infty$, such that $\rho = N/\Omega$ is constant. To this end, we seek to understand the source and magnitudes of finite-size errors. If X is an observable, the finite-size error is defined as $\Delta X_\infty = X_\infty - X_N$, where X_N is the estimate in a system with N particles, and X_∞ is the estimate for the thermodynamic limit. In this work, we will be concerned strictly with electronic finite-size errors in systems where the ionic positions are fixed, since this is the constraint we used in our benchmarking studies. Fortunately, the source of electronic finite-size errors is reasonably well understood. This often allows us to mitigate the sources of error directly in a simulation, and also calculate ΔX_∞ to reasonably accuracy.

In this chapter we begin by presenting the general theory of finite-size errors in QMC simulations. We initially present the existing theory for correcting the total energy. We then present our new generalizations of this theory to force and stress estimators. When applying the above methods to hydrogen-helium mixtures, we encountered some subtleties not discussed in the existing literature. In the last section, therefore, we present some extensive tests of the Chiesa scheme we used in hydrogen-helium mixtures against supercell calculations and other commonly used finite-size correction schemes found in the literature.

7.2 General Theory

If N_e is the number of electrons in our system, then we define the energy-per-electron for this system as $E_N = \frac{\langle \hat{H} \rangle}{N_e}$. We likewise define the kinetic and potential energy-per-electron as $t_N = \frac{\langle \hat{T} \rangle}{N_e}$ and $v_N = \frac{\langle \hat{V} \rangle}{N_e}$ respectively.

We also define the structure factor for species α and β as:

$$S_N^{\alpha\beta}(\mathbf{G}) = \frac{1}{\sqrt{N_\alpha N_\beta}} \left\langle \rho^\alpha_{-\mathbf{G}} \rho^\beta_{\mathbf{G}} \right\rangle \tag{7.1}$$

It will be useful to define a "fluctuation" structure factor. Let $\overline{\rho_{\mathbf{G}}} = \langle \rho_{\mathbf{G}} \rangle$. If $\rho_{\mathbf{G}} = \overline{\rho_{\mathbf{G}}} + \delta\rho_{\mathbf{G}}$, then the fluctuation structure factor is defined as:

$$\delta S_N^{\alpha\beta}(\mathbf{G}) = \frac{1}{\sqrt{N_\alpha N_\beta}} \left\langle \delta\rho^\alpha_{-\mathbf{G}} \delta\rho^\beta_{\mathbf{G}} \right\rangle \tag{7.2}$$

At supercell k-points incommensurate with the unit cell, the electron-electron structure factor and the "fluctuation" structure factor will equal one another. This is because the static electronic charge density $\overline{\rho^e_{\mathbf{G}}}$ vanishes at these k-points. At k-points commensurate with the supercell, $\overline{\rho_{\mathbf{G}}}$ will usually not be zero. In these cases, the distinction between the structure factor and fluctuation structure factor is important since the finite-size effects associated with each will be different.

7.3 One-Body effects

Assume for the moment that a fermionic system is reasonably approximated by a non-interacting single-particle picture, such as given by Eq. 4.5. Consider a supercell calculation made up of an $N_0 \times N_1 \times N_2$ tiling of a unit cell. For non-interacting theories in periodic boundary conditions, Bloch's theorem allows us to relate the single-particle orbitals of the supercell to those of the unit cell with the following [54]:

$$\phi_{m,\mathbf{k}}(\mathbf{r}) = e^{i\mathbf{k}\cdot\mathbf{r}} u_{m,\mathbf{k}}(\mathbf{r}) \tag{7.3}$$

Here, $u_{m,\mathbf{k}}(\mathbf{r})$ is a function which is periodic in the unit cell, m is a band-index, and $\mathbf{k}$ is a vector in the Brillouin zone. The vector $\mathbf{k}$ is often called a "twist" because as one translates the electron by one box length in any dimension, the orbital acquires a non-zero phase. The ground state is taken to be a Slater-Determinant, obtained by doubly occupying orbitals in order of ascending single-particle energy $\epsilon_{m,\mathbf{k}}$.

For the supercell described previously, the folding of everything to the unit cell creates a reciprocal space grid, defined by:

$$\mathbf{k}_{n_0 n_1 n_2} = \sum_{i=0}^{2} \frac{2n_i - N_i - 1}{2N_i} \mathbf{b}_i \tag{7.4}$$

Here, $n_i = 1, \ldots, N_i$. This is known as a Monkhorst-Pack grid [54]. The set of highest occupied states for finite N can be described by some subset of the reciprocal space grid $\{\mathbf{k}\}$ corresponding to the highest

occupied states in each direction. However, as one approaches the thermodynamic limit, the set of distinct points becomes a smooth "Fermi-surface". The representation of a smooth Fermi-surface with a discretized collection of points on a grid introduces a large and slowly converging finite-size error. This is dealt with in single particle theories by performing "Brillouin zone" integration on a Monkhorst-Pack grid which is dense enough to reasonably approximate the smooth Fermi-surface.

For QMC, the way to remove this sort of finite-size effects is to employ what's known as "twist averaged boundary conditions" [99]. For a given twist vector $\boldsymbol{\theta}$, the twisted many-body wave function is assumed to follow a similar transformation to Eq. 7.3:

$$\Psi_{\boldsymbol{\theta}}(\mathbf{r}_0 + \mathbf{L}_0, \ldots, \mathbf{r}_{N_e-1} + \mathbf{L}_{N_e-1}) = e^{i \sum_i \boldsymbol{\theta}\cdot\mathbf{L}_i} \Psi_\theta(\mathbf{r}_0, \ldots, \mathbf{r}_{N_e-1}) \tag{7.5}$$

$\mathbf{L}_i$ are integer linear combinations of the unit-cell lattice vectors, but are otherwise arbitrary. Using this class of wave functions, we generate a large number of twists $\{\boldsymbol{\theta}\}$ and average QMC expectation values with respect to the twists. This procedure is known as "twist-averaging", and is responsible for eliminating the shell effects affecting single-particle properties by approximately two orders of magnitude [99].

In all calculations performed in this work, we make two simplifications to the method outlined in the original paper. First, while the original paper suggests averaging over random twist angles $\boldsymbol{\theta}$, we deterministically average over Monkhorst-Pack grids. Before any production run, we compute orbitals corresponding to different sizes of Monkhorst-Pack grids and observe how various VMC or DMC observables converge with respect to the size of the Monkhorst-Pack grid. Secondly, we use "canonical" twist-averaging, which means that at each twist angle $\boldsymbol{\theta}$, the ground state wave function is an N_e electron wave function. This means that there will on average be occupations above the Fermi-surface, which will introduce a systematic bias. The way to correct for this effect is to use a single particle theory. Let $\nu(\epsilon)$ be the density of states. The correction is calculated by:

$$\Delta E = \frac{1}{N_e N_\theta} \sum_{\boldsymbol{\theta}} \sum_n \epsilon_{n,\boldsymbol{\theta}} - \frac{1}{\rho} \int_0^{\epsilon_F} d\epsilon \epsilon \nu(\epsilon) \tag{7.6}$$

In practice, we approximated the last integral by a very dense k-point mesh. We ignored this effect for our hydrogen benchmarking work, but accounted for this in our hydrogen-helium work. We used a $7 \times 7 \times 7$ grid to compute the second term, in contrast with the $3 \times 3 \times 3$ or $4 \times 4 \times 4$ grids used for twist averaging.

7.4 Two-Body Correlations

After shell effects, the next most important contribution to finite-size effects come from long-range electron-electron correlation effects. For conceptual simplicity, let us work entirely in reciprocal space for now. Within the optimized breakup formalism, this is equivalent to taking $\sigma(r) = 0$ and $\Lambda_{\mathbf{G}} = v_{\mathbf{G}}$.

For the potential and kinetic energy, we can write the magnitude of the finite-size correction exactly as:

$$\Delta t_N = \int \frac{d\mathbf{k}}{(2\pi)^3} \frac{1}{2} k^2 n_\infty(\mathbf{k}) - \sum_{\mathbf{k}} \frac{1}{2} k^2 n_N(\mathbf{k}) \tag{7.7}$$

$$\Delta v_N = \frac{1}{2} \sum_{\alpha,\beta} \left[\int \frac{d\mathbf{k}}{(2\pi)^3} v_{\mathbf{k}}^{\alpha\beta} \frac{\sqrt{N_\alpha N_\beta}}{N_e} S_\infty^{\alpha\beta}(\mathbf{k}) - \sum_{\mathbf{k}\neq 0} v_{\mathbf{k}}^{\alpha\beta} \frac{\sqrt{N_\alpha N_\beta}}{N_e} S_N^{\alpha\beta}(\mathbf{k}) \right] \tag{7.8}$$

Here, $n_N(\mathbf{k})$ is the momentum distribution for a system of size N_e, defined as:

$$n_N(\mathbf{k}) = \int d\mathbf{r} d\mathbf{r}' d\mathbf{r}_1 \dots d\mathbf{r}_{N-1} e^{i\mathbf{k}\cdot(\mathbf{r}-\mathbf{r}')} \Psi^*(\mathbf{r}, \mathbf{r}_1, \dots, \mathbf{r}_{N_e-1}) \Psi(\mathbf{r}', \mathbf{r}_1, \dots, \mathbf{r}_{N_e-1}) \tag{7.9}$$

We can develop the above formulas into a practical finite-size correction scheme by noting the following. First, since the ions are fixed, there are no finite-size effects associated with them. Thus, all ion-ion terms drop out of Eq. 7.8. Secondly, the average electron density $\overline{\rho_{\mathbf{k}}^e}$ converges rapidly with system size, particularly when twist-averaging is used. Not only this, but the average electron density is only defined at k-points commensurate with the unit cell. Assuming that the simulation cell is large enough such that $\overline{\rho_{\mathbf{k}}^e}$ is converged, we can cancel out terms in Eq. 7.8 depending on $\overline{\rho_{\mathbf{k}}^e}$ and $\overline{\rho_{-\mathbf{k}}^e \rho_{\mathbf{k}}^e}$. This just leaves an explicit dependence on the fluctuation structure factor $\delta S^{ee}(\mathbf{k})$. This makes intuitive sense, since it demonstrates that most of the finite-size errors affecting many-body simulations stem from the neglect of long-range correlations, instead of from electrostatics.

As we approach the thermodynamic limit, the k-space grid on which $\delta S_N^{ee}(\mathbf{k})$ is defined will approach a continuum, implying that $\delta S_\infty^{ee}(\mathbf{k})$ is a continuous function of $\mathbf{k}$. Empirically, $\delta S_N^{ee}(\mathbf{k})$ converges rapidly with system size [100], implying that we can approximate $\delta S_\infty^{ee}(\mathbf{k})$ by interpolating $\delta S_N^{ee}(\mathbf{k})$ to k-points not on the k-point grid. The $|\mathbf{k}| \to 0$ behavior is assumed to be given by the random phase approximation (RPA) of the homogeneous electron gas, which states that $\delta S^{ee}(\mathbf{k} \to 0) \propto k^2$. To generalize to anisotropic systems, we assume that $\delta S_\infty^{ee}(\mathbf{k} = 0) = 0$ and $\nabla_{\mathbf{k}} \delta S_\infty^{ee}(\mathbf{k} = 0) = 0$. We denote the interpolated structure factor subject to the proper $k \to 0$ boundary conditions $\widetilde{\delta S_N^{ee}}(\mathbf{k})$.

Assuming that $\delta S_\infty^{ee}(\mathbf{k}) \approx \widetilde{\delta S_N^{ee}}(\mathbf{k})$, we find the finite-size error for the potential is given by:

$$\Delta v_N = \frac{1}{2}\left[\int \frac{d\mathbf{k}}{(2\pi)^3} - \sum_{\mathbf{k}\neq 0}\right] v_{\mathbf{k}}^{ee}\widetilde{\delta S_N^{ee}}(\mathbf{k}) \tag{7.10}$$

This indicates that even if we are in a simulation cell where $\delta S_\infty^{ee}(\mathbf{k}) = \widetilde{\delta S_N^{ee}}(\mathbf{k})$, we will still incur an error from the approximation of the integral with a discrete sum. Fortunately, this error can be calculated either by evaluating Eq. 7.10 exactly, or by estimating the dominant contribution coming from the region near $\mathbf{k} = 0$. To facilitate explicit evaluation, we use the long-range breakup scheme from Chapter 6 to write Eq. 7.10 in terms of the potential breakup expressions:

$$\Delta v_N = \frac{1}{2}\left[\int \frac{d\mathbf{k}}{(2\pi)^3} - \sum_{\mathbf{k}\neq 0}\right] \Lambda_{\mathbf{k}}^{ee}\widetilde{\delta S_N^{ee}}(\mathbf{k}) \tag{7.11}$$

To approximate the kinetic energy expression in Eq. 7.7, one can use the RPA to rewrite the bosonic part of the kinetic energy expression in terms of the long-range Jastrow of the system: $U = \frac{1}{2\Omega}\sum_{\mathbf{k}} u_N(\mathbf{k})\rho_{-\mathbf{k}}^e\rho_{\mathbf{k}}^e$ [100, 101]. Specifically,

$$n_N(\mathbf{k}) \approx \frac{\rho}{\Omega} u_N(-\mathbf{k})u_N(\mathbf{k})\delta S_N^{ee}(\mathbf{k}) \tag{7.12}$$

The full momentum distribution can be obtained through an appropriate convolution with the Fermi-Dirac distribution, which we omit here [102].

We already stated how interpolating $\delta S_N^{ee}(\mathbf{k})$ gives an excellent approximation to $\delta S_\infty^{ee}(\mathbf{k})$. It turns out that the same arguments hold for the long-range Jastrow $u_N(\mathbf{k})$. For large enough system sizes N, the differences between $u_N(\mathbf{k})$ and $u_\infty(\mathbf{k})$ are just a result of $u_N(\mathbf{k})$ being specified on a grid. One constructs an interpolated approximation $u_\infty(\mathbf{k}) \approx \widetilde{u_N}(\mathbf{k})$ by splining $u_N(\mathbf{k})$, subject to the limiting behavior $u_\infty(\mathbf{k}) \propto k^{-2}$ as $|\mathbf{k}| \to 0$ [100]. This allows us to write the kinetic energy correction as:

$$\Delta t_N = \left[\int \frac{d\mathbf{k}}{(2\pi)^3} - \sum_{\mathbf{k}\neq 0}\right] \frac{1}{2}k^2\rho\widetilde{u_N}(-\mathbf{k})\widetilde{u_N}(\mathbf{k})\widetilde{\delta S_N^{ee}}(\mathbf{k}) \tag{7.13}$$

We will refer to the above corrections for the potential and kinetic energies as the "Chiesa" or "correlation function" corrections.

One can show from the above expressions that the leading order finite-size errors for both the kinetic and potential energy terms scale like $1/N$ [100]. This recovers the traditional "1/N extrapolation" commonly used to perform finite-size corrections.

7.5 Force Estimator

Recalling Eq. 6.19 for the electron-ion force in periodic boundary conditions, we note the only terms susceptible to finite-size effects are those involving just the electron density $\rho^e_{\mathbf{G}}$. As discussed in the previous sections, the density converges rapidly with respect to system size. Assuming twist-averaging is done on a dense enough grid, the finite-size effects associated with forces are negligible.

7.6 Stress Estimator

In contrast to the force estimator, the stress estimator is very susceptible to finite-size effects. Fortunately, it is amenable to the exact same arguments and formalism used to treat total energies. One can show that the finite-size corrections to the kinetic and potential parts of the stress tensor can be given respectively by:

$$[\Delta\boldsymbol{\sigma}_{kinetic}]_{\mu\nu} = \left(\int \frac{d\mathbf{k}}{(2\pi)^3} - \sum_{\mathbf{k}}\right) \frac{1}{2} k_\mu k_\nu \rho \widetilde{u_N}(-\mathbf{k}) \widetilde{u_N}(\mathbf{k}) \widetilde{\delta S^{ee}_N}(\mathbf{k}) \tag{7.14}$$

$$[\Delta\boldsymbol{\sigma}_{LR}]_{\mu\nu} = \left(\int \frac{d\mathbf{k}}{(2\pi)^3} - \sum_{\mathbf{k}}\right) \frac{1}{2} \left[\frac{k_\mu k_\nu}{k} \frac{\partial \Lambda^{ee}_{\mathbf{k}}}{\partial k} - \delta_{\mu\nu} \Lambda^{ee}_{\mathbf{k}}\right] \widetilde{\delta S^{ee}}_{N,\delta\delta}(\mathbf{k}) \tag{7.15}$$

7.7 Validation

In our work on pure hydrogen, we computed average finite-size corrections for ensembles of configurations. This means that from molecular dynamics trajectories corresponding to a particular temperature, density, and structure, we drew a handful of configurations (between 5 and 10) and performed 1/N extrapolations to compute the total energy, kinetic energy, potential energy, and pressure corrections. Note that since we used periodic boundary conditions in the unit cell, the ion positions did not change as we considered larger supercells. The average of these corrections was taken to be the finite-size corrections for the entire set of configurations at that density.

For our work on hydrogen-helium mixtures, we used the above correlation function based methods to compute the finite-size corrections. As we have had problems in the past applying these methods, we validated these methods against 1/N extrapolations. The unit cell was taken to be a disordered liquid snapshot with r_s=1.10a_0, $N_e = 64$, $N_H = 56$, and $N_{He} = 4$. The supercell was taken to be $2 \times 2 \times 2$ tiling of the unit cell.

The trial wave functions for the unit cell and supercell were chosen to be Slater-Jastrow without backflow. Single-particle orbitals were generated with a plane-wave cutoff of 200Ry using the PBE functional within

Name	Type	Interaction	Function	r_{cut}	Cusp	N_{knots}	Optimizable
J2	two-body	e-e (opposite spin)	b-spline	3.546	Yes	10	Yes
	two-body	e-e (like spin)	b-spline	3.546	Yes	10	Yes
J1L	one-body	e-H	b-spline	3.546	No	8	Yes
	one-body	e-He	b-spline	3.546	No	8	Yes
J1S	one-body	e-H	b-spline	1.000	Yes	8	Yes
	one-body	e-He	b-spline	1.000	Yes	8	Yes

Table 7.1: Summary of the Jastrow factors included in the trial wave function.

PWSCF. We used a $4 \times 4 \times 4$ Monkhorst-Pack grid with an offset in the unit cell, which we "unfolded" to generate a $2 \times 2 \times 2$ grid in the supercell. Troullier-Martin pseudopotentials [103] were used for both the H and He atoms, which we generated with the PBE functional in the OPIUM code. The real space cutoff for both pseudopotentials was $0.37a_0$.

To investigate the sensitivity of the finite-size correction schemes to choice of wavefunction, we considered two types of Jastrow factors. The first type is entirely short-ranged, built up from spherically symmetric, fully optimizable b-splines for the electron-ion and electron-electron functions. We summarize all the Jastrow factors we used in Table 7.1. This is representative of the Jastrow factor used in our hydrogen and hydrogen-helium simulations, except that r_c for "J1L" and "J2" are set to be $L/2$. We will henceforth refer to the Slater-Jastrow wave function built with this Jastrow as "wave function 1". The second type augments the short-ranged Jastrow with a long-range Jastrow $U = \frac{1}{2\Omega}\sum_{\mathbf{k}} u_N(\mathbf{k})\rho^e_{-\mathbf{k}}\rho^e_{\mathbf{k}}$. $u_N(\mathbf{k})$ was assumed to be spherically symmetric in reciprocal space and had a reciprocal space cutoff of 7 k-shells. Otherwise, it was assumed to be fully optimizable. The wave function built from this Jastrow is called "wave function 2". These two types of wave functions are also used in the supercell calculation. However, k_c is reduced by a factor of 2, and the cutoff for "J1L" and "J2" are increased to $L/2$ in the supercell.

For wave function 1, we used 1024 walkers in both the VMC and DMC simulations. We used particle-by-particle moves for both VMC and DMC. A time step of $\tau = 0.5Ha^{-1}$ and $\tau = 0.01Ha^{-1}$ were used for the VMC and DMC simulations respectively. The same parameters were used in the supercell.

For wave function 2, we used a time step of $\tau = 0.1Ha^{-1}$ and 1024 walkers for VMC. In the supercell, we used $\tau = 0.2Ha^{-1}$. RMC was used to calculate mixed and pure observables in both the unit and supercell. In the unit cell, we used a projection time of $\beta = 5.16Ha^{-1}$. We used two time steps, $\tau = 0.0075Ha^{-1}$ and $\tau = 0.00375Ha^{-1}$, to extrapolate all observables to the $\tau \to 0$ limit. In the supercell, we used a projection time of $\beta = 4.0Ha^{-1}$ and $\tau = 0.0075Ha^{-1}$.

In Table 7.2, we show the finite-size corrections obtained from 1/N extrapolations based on wave functions 1 and 2. All values are twist-averaged, and the single-particle corrections discussed at the end of Section 7.3 are included. Notice that the RMC and DMC finite-size corrections for the total energy differ by less

WF	Method	N	ΔE	Δv_N	Δt_N	Δv_N^{ee}	$\Delta V_N^{ee}(MPC)$	ΔV_N^{ei}
1	VMC	64	0.012145(4)	0.04460(9)	-0.03245(9)	0.00544(1)	0.00685(1)	0.0391(1)
	DMC	64	0.00803(1)	0.0254(1)	-0.01740(9)	0.00537(4)	0.00618(3)	0.0200(1)
	EXTR	64	–	0.0063(2)	0.0017(2)	0.00530(7)	0.00551(6)	0.0009(2)
2	VMC	64	0.01534(1)	0.0388(3)	-0.0228(1)	0.02775(5)	0.00585(2)	0.0111(1)
	RMC	64	0.00816(3)	0.0164(2)	-0.0072(2)	0.01452(7)	0.00557(5)	0.0012(2)
	EXTR	64	–	-0.0074(4)	0.0085(4)	0.0014(1)	0.00529(5)	-0.0087(4)
	PURE	64	–	0.0069(9)	0.0014(5)	0.0066(2)	0.00538(8)	0.0005(7)

Table 7.2: Summary of finite-size corrections taken from 1/N extrapolation data on wave functions #1 and #2. All units are in Ha/N. Single-particle kinetic energy corrections have been included.

than 0.16mHa/atom, which is small but statistically significant. In contrast, the extrapolated finite-size corrections for the kinetic and various potential pieces differ wildly between the two wave functions. For example, the kinetic energy correction is $6.3(2) mHa/N$ for wave function 1, but is $-7.4(4) mHa/N$ for wave function 2. As one can see by looking at the pure estimates in the last line of the table, the difference is attributed to residual mixed estimator bias in wave function 2. Interestingly, wave function 1 agrees with the pure RMC estimates to within error bars.

Now that we have a baseline, we compute the correlation function finite-size corrections. For the potential energy correction, we calculated the full $\delta S_N^{ee}(\mathbf{k})$ fluctuation structure factor for $\mathbf{k}$ vectors commensurate with the unit cell. This was done using both VMC and DMC, using wave function 1. Using the extrapolated estimate of the fluctuation structure factor, $\delta S_N^{EXT}(\mathbf{k}) = 2\delta S_N^{DMC}(\mathbf{k}) - \delta S_N^{VMC}(\mathbf{k})$, we performed a 1D cubic spline interpolation on a spherically averaged $\delta S_N^{EXT}(\mathbf{k})$, subject to the constraint that $\delta S_N^{EXT}(|\mathbf{k}|) \to \alpha k^2$ as $|\mathbf{k}| \to 0$. With the splined form of $\delta S_N^{EXT}(|\mathbf{k}|)$ in hand, we were able to numerically calculate the potential energy integration error.

For the kinetic energy correction, the procedure we described requires an optimized k-space Jastrow factor to capture the long-range electron correlations. As the Jastrow factors of wave function 1 are short-ranged, the leading order Chiesa scheme would yield no correction to the kinetic energy. To get around this, we compare the difference between the potential energy corrections obtained using the extrapolated structure factor $\delta S_N^{EXT}(\mathbf{k})$ and the mixed estimator $\delta S_N^{DMC}(\mathbf{k})$. The difference is associated with the magnitude of the kinetic energy correction [101]. This is because while $\delta S_N^{EXT}(\mathbf{k})$ produces the correct potential energy correction, we could just as well compute the potential energy correction for the mixed distribution by using $\delta S_N^{DMC}(\mathbf{k})$. Since the total energy correction must come out the same in both cases, the difference between the mixed and pure estimates must be associated with an incorrect apportioning of the finite-size corrections between the potential and kinetic terms. Since the short-ranged Jastrow yields a negligible finite-size correction at the mixed-estimator level, we associate the potential difference with the kinetic energy correction, at least to leading order.

Method	N	ΔE_N	Δv_N	Δt_N	ΔV_N^{ee}	ΔV_N^{ei}
SS	64	0.00816(3)	0.0069(9)	0.0014(5)	0.0066(2)	0.0005(7)
KZK	64	0.00682	-	-	-	-
Chiesa	64	0.00735	0.0059	0.00143	0.0059	0.000
MPC	64	0.00538(8)	0.00538(8)	-	0.00538(8)	-

Table 7.3: Summary of finite-size corrections from supercell (SS), KZK, Chiesa, and MPC. Columns 3-7 show the total energy, potential, kinetic, electron-electron, and electron-ion finite-size errors respectively. Units are in Ha/N. For methods that cannot compute a certain component, we leave the cell blank. Wave function #1 was used for everything except the supercell calculations. We see that the Chiesa scheme produces the best estimate of the total energy and all energy components.

We also used the long-range Jastrow in wave function 2 to compute the kinetic energy correction by the original Chiesa method. By fitting our long-range Jastrow to the RPA form, we used the fitted parameters to obtain the leading order kinetic energy correction [100, 101]. We found this to be statistically indistinguishable from the structure factor method described in the previous paragraph. Thus, we used the structure factor method in our hydrogen-helium work.

In Table 7.3, we compare the Chiesa and supercell finite-size corrections against two other commonly used finite-size correction schemes. The first is the Kwee, Zhang, Krakauer method, which is an LDA based finite-size correction scheme for the total energy [104]. The second is the model periodic coulomb (MPC) method, which is a hybrid DFT/QMC method which seeks to correct the finite-size truncation of the exchange-correlation hole [105, 106]. The correction is defined as $\Delta v_N^{MPC} = \frac{1}{N_e}\left(\langle V^{MPC}\rangle - \langle V^{ee}\rangle\right)$.

We find that the Chiesa scheme described previously is the most accurate for not only the total energy, but also for the kinetic and potential energy corrections as well. Taking the $1/N$ extrapolation as an "exact" reference, the Chiesa correction is within 0.81mHa (27σ, where σ is the standard deviation) for the total energy estimate, 1mHa (1σ) for the potential energy, and 0.5mHa (1σ) for the kinetic energy. The MPC correction does fairly well for predicting Δv_N^{ee}, however the error is larger than the Chiesa correction. The KZK correction also performs fairly well, although the error is noticeably higher: 1.3mHa for KZK as opposed to 0.8mHa for Chiesa.

In hydrogen-helium mixtures, we are interested in finite-size corrections for liquid snapshots over a range of helium concentrations and densities. While we have tested our finite-size correction scheme on a single disordered configuration, the most pressing question is how well our finite-size correction scheme works over a range of configurations. To this end, we considered snapshots at densities given by r_s=1.10a_0 and r_s=1.34a_0. At each density, we considered 14 different helium concentrations. For each density and helium concentration, we chose two random configurations and performed supercell calculations. We then calculated the Chiesa corrections for all configurations and compute the error relative to the supercell calculations.

In Table 7.4, we show the average error and mean absolute deviation (MAD) of the finite-size correction

Density	Quantity	ΔE_N^{SS}	ΔE_N^{Ch}	$\Delta E_N^{Ch} - \Delta E_N^{SS}$
1.10	Mean	8.52	7.33	-1.20
1.34	Mean	6.36	5.39	-0.97
1.10	MAD	0.38	0.14	0.50
1.34	MAD	0.22	0.17	0.35

Table 7.4: Mean and mean absolute deviation (MAD) of the supercell energy correction (ΔE_N^{SS}), Chiesa energy correction (ΔE_N^{Ch}), and Chiesa correction error, all in mHa/N units.

scheme relative to the supercell calculations. Though we see in the last column that the total finite-size error is approximately 1 mHa/N, these errors will largely cancel (to within 0.23mHa/N) when considering differences between configurations. Secondly, though the MAD seems large (between 0.35 and 0.5 mHa/N), one should keep in mind that this is calculated across all considered helium concentrations at a given density. Deviations within a particular density and helium configuration are expected to be significantly smaller.

Chapter 8

DFT Benchmarks of Hydrogen

8.1 Introduction

In this chapter, we present the results of our published benchmarking study on solid and liquid hydrogen under extreme pressures [107]. We begin by discussing the construction of *ab initio* test sets. We then define several different types of errors we can compute using our test sets. After presenting the results of our benchmarking work in hydrogen, we conclude by showing how the results of benchmarking can be used to improve quasi-harmonic ground state calculations in dense hydrogen.

8.2 Motivation

Despite the major advancements in methodologies and computational power, the phase diagram of hydrogen is still difficult to treat theoretically. This is because the energy scales relevant for determining important molecular dissociation and insulator-to-metal transitions are well under 1mHa/atom. This demand for sub-chemical accuracy requires a reexamination of all errors introduced by cost-saving approximations. The two largest sources of error are the treatment of electronic exchange-correlation effects through the use of an approximate density functional, and the treatment of nuclear quantum effects. Assuming that the Born-Oppenheimer approximation is still valid, nuclear quantum effects can be treated exactly within the PIMD framework, so we will not focus on this source of error for now.

This leaves the choice of density functional as the largest uncontrolled source of error. While one can dispense with DFT entirely and use QMC-based CEIMC for finite temperature properties [108], our approach is to judiciously use QMC to extend the applicability of DFT [107, 1]. After all, if we can establish ahead of time that DFT is accurate enough for a particular observable, we can save ourselves the great expense of having to do a many-body calculation.

We do this by using QMC to benchmark density functionals. Understanding the magnitude and trends of various errors incurred by a functional allows us to do three things. First, it allows us to quickly assess

whether or not there are any functionals that are accurate enough for a given application. It could be that there are none, in which we would have to fall back to a more accurate theory. However, even though LDA or PBE might not give the required accuracy, it is possible that there might exist another functional that could. We will see that for calculating energy differences, it is possible to reduce DFT errors by up to a factor of four by choosing a non-traditional functional. Secondly, if the errors are well enough behaved, we can often construct corrections. We will see that the pressure errors fall into this category. Lastly, understanding the magnitude and trends of errors potentially allows us to locate the sources of errors, which is a necessary step for constructing better functionals.

8.3 Constructing Test Sets

We are interested in benchmarking density functionals in two important regions of the phase diagram. First is in the vicinity of the liquid-liquid phase transition. We focus on densities between r_s=1.30a_0 and r_s=1.60a_0 at a temperature of T=1000K. These densities were chosen to straddle the transition. In the solid phase, we are most concerned with the atomic-to-molecular transition. At zero-temperature, this is believed to occur above 300GPa and below 500GPa. Due to the difficulty associated with correctly describing the energetics of the H_2 bond, we focus on benchmarking functional performance near the transition, but within the molecular phase. We will construct test sets corresponding to various solid phases at P=200GPa and P=300GPa.

We define a test set S as a collection of M proton configurations $S = \{\mathbf{R}_1, \mathbf{R}_2, \ldots, \mathbf{R}_M\}$ representing bulk hydrogen at a particular temperature, density, and structure (either liquid, or a particular solid phase). We demand that these configurations be uncorrelated and "physically reasonable". "Physically reasonable" means that the configurations should in some way sample the part of phase space in which we are interested. Similar in spirit to "importance sampling", we want to test functionals wherever the system is most likely to be used. This is in contrast to drawing configurations from a uniform distribution, which would produce configurations unlikely to be witnessed except near the infinite temperature limit.

To produce "physically reasonable" configurations, we performed used PI+GLE with the PBE functional in both the solid and liquid phases. For the liquid, we used a cubic unit cell with $N_H = 54$ hydrogen atoms. Configurations were generated at T=1000K using three different densities: r_s=1.30a_0, 1.45a_0, and 1.60a_0. For each density, we sampled 100 configurations, ensuring that the simulation time between each sample well exceeded the energy autocorrelation time. For the solids, we considered four different proposed hydrogen structures: $C2/c$, $Cmca$, $Cmca-12$, and $Pbcn$. We used supercells with $N_H = 96$ atoms. We used

two densities for each structure, corresponding to PBE optimized ground state structures at a pressures of 200GPa and 300GPa. Samples were generated at T=200K. Due to the increased computational cost associated with the larger simulation cells, we only used 20 configurations per structure per density for the solids.

With the ionic test sets in hand, we computed reference total energies and pressures for each ionic configuration using QMC. For solid and liquid configurations, we used Slater-Jastrow backflow wave functions. The single-particle orbitals were generated with PWSCF [109] using the PBE functional. An energy cutoff of 120Ry was used in the plane-wave calculations. To remove the electron-ion cusp, we used an all-electron Troullier-Martins hydrogen pseudopotential with a cutoff radius of $r_c = 0.5a_0$. The Jastrow factor had a similar form to that described in Table 7.1. The backflow transformation was built using optimizable short-ranged b-spline functions for the electron-ion, like electron spin, and opposite electron spin interactions. With this choice of wave function, we were able to use DMC time steps of $\tau = 0.025Ha^{-1}$ for the solid configurations and $\tau = 0.05Ha^{-1}$ for the liquid configurations to ensure total energies and pressures were converged to within 0.02mHa/atom and 0.2GPa respectively.

Single-particle finite-size effects were handled using twist-averaged boundary conditions. We used canonical twist averaging with $3 \times 3 \times 3$ and $6 \times 6 \times 6$ Monkhorst-Pack grids for the liquids and solids respectively. The many-body finite-size effects were handled using the ensemble correction described in the previous chapter.

QMC pressures were computed using the virial theorem [54], which relates the pressure to the potential and kinetic energies with the following formula:

$$P = \frac{1}{3\Omega}(2T + V) \tag{8.1}$$

For practical reasons, we chose to use the equivalent form for the pressure estimator: $P = \frac{1}{3\Omega}(E + T)$. This was because the total energy E is estimated without a mixed-estimator bias. The kinetic energy is then estimated using an extrapolated estimate.

8.4 DFT Details

All DFT calculations were performed at zero temperature. For both solid and liquid configurations, we computed DFT energies and pressures within PWSCF using the following functionals: LDA, PBE, vdW-DF, vdW-DF2, and HSE. We used a plane wave cutoff of 200Ry. A hard Troullier-Martins pseudopotential with a cutoff radius of $0.5a_0$ was used to remove the coulomb singularity [110].

For the solids, we used VASP [111, 112] to calculate the following additional functionals: vdW-optPBE, vdW-optB88, vdW-optB86b [113], and vdW-TS [114]. Since these calculations are within the projector-augmented wave (PAW) formalism, a significantly reduced 58.8Ry plane wave cutoff was used. Additionally, we used a PAW consistent hydrogen pseudopotential with a real space cutoff of $1.1a_0$.

To handle electronic finite size effects, we used a $6\times6\times6$ Monkhorst-Pack grid with offset. The systematic errors associated with both the DFT and QMC results are expected to be less than 0.01mHa/atom for energies and 0.3GPa for pressures.

8.5 Benchmarking Methods

After generating DFT estimates of energies and pressures for all configurations in our test sets, the next step is to calculate the DFT errors. Let the observable X for a configuration $\mathbf{R}_i$ be $X(\mathbf{R}_i)$. The DFT error for this configuration is defined as $\delta X^{DF}(\mathbf{R}_i) = X^{DF}(\mathbf{R}_i) - X^{QMC}(\mathbf{R}_i)$, where DF denotes the density functional used to calculate X.

For a test set S of size M, we can define an "average error" in the usual way:

$$\left\langle \delta X^{DF} \right\rangle_S = \frac{1}{M} \sum_{\mathbf{R}_i \in S} \delta X^{DF}(\mathbf{R}_i) \tag{8.2}$$

We will also use absolute values of the error given by the following form:

$$\left\langle \widetilde{|\delta X^{DF}|} \right\rangle_S = \frac{1}{M} \sum_{\mathbf{R}_i \in S} |\delta X^{DF}(\mathbf{R}_i) - c^{DF}| \tag{8.3}$$

One can define different classes of error measures depending on how c^{DF} is chosen. For example, setting $c^{DF} = 0$ recovers the traditional "mean-absolute error". Choosing c^{DF} to minimize $\left\langle \widetilde{|\delta X^{DF}|} \right\rangle_S$ recovers the "mean-absolute deviation" of the set.

When calculating energetic errors, we find it helpful to distinguish between two types of errors, which we call "global" and "local" energetic errors. Global energetic errors refer to how well a functional captures energy differences between different structures. This is important in situations such as establishing which phase is thermodynamically stable at a given temperature and volume. We define this error measure by choosing c^{DF} in the following manner. We build an aggregated test set S' for a particular density by including configurations from all structures at that density. The c^{DF} is then chosen to minimize $\left\langle \widetilde{|\delta E^{DF}|} \right\rangle_{S'}$ over the aggregated test set. The resulting global energetic error on the test set S will then be denoted as $\left\langle \widetilde{|\delta E^{DF}|} \right\rangle_{S,global}$.

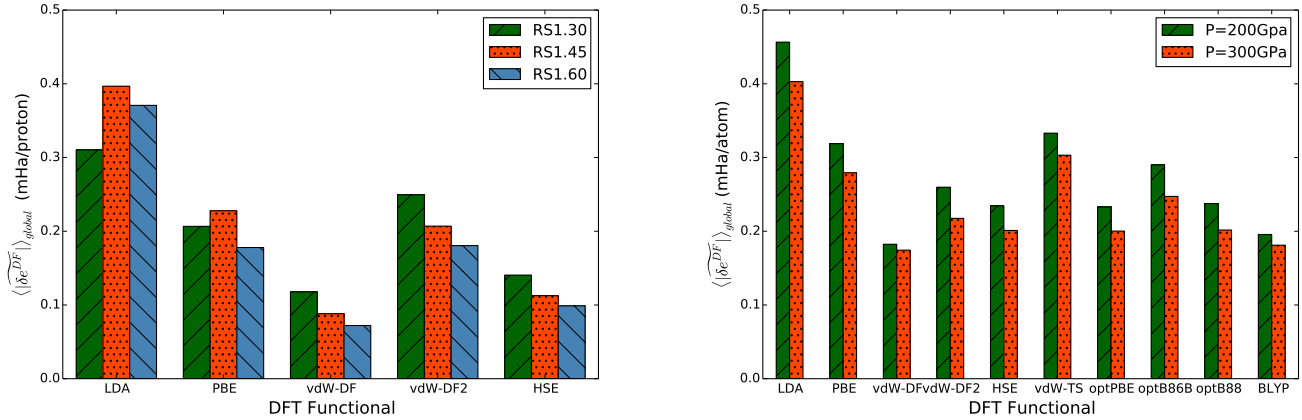

Figure 8.1: (Left) Global energetic errors of DFT functionals in liquid hydrogen at densities $r_s = 1.30, 1.45, 1.60$. (Right) Global energetic errors of DFT functionals in solid hydrogen at densities corresponding to P^{DF}=200GPa, 300GPa. All units are in mHa/atom

Local energetics refer to how well a given density functional identifies and approximates the local minima of a potential energy surface. To this end, for each test set corresponding to a particular density and structure, we choose c^{DF} to minimize $\left\langle|\widetilde{\delta E^{DF}}|\right\rangle_S$. We will denote this error measure as $\left\langle|\widetilde{\delta E^{DF}}|\right\rangle_{S,local}$. This error measure is not valid for the liquid phase, since the system does not spend most of its time around a local minima as in the solid case.

8.6 Results

8.6.1 Energetics

In Figure 8.6.1, we plot the global energetic error for both liquid (left) and solid hydrogen (right). For the solids, we plot $\left\langle|\widetilde{\delta E^{DF}}|\right\rangle_{global}$, which is constructed by computing $\left\langle|\widetilde{\delta E^{DF}}|\right\rangle_{S,global}$ for each structure at a given density, and then averaging over the structures. We see see that PBE incurs global energetic errors between 0.2mHa/atom and 0.3mHa/atom. While not the worst, it is possible to reduce the errors by a factor of a third or a half by using a functional like vdW-DF or BLYP.

In Figure 8.2, we plot the average local energetic errors, constructed by averaging the local energetics for all structures at a fixed density. The striking feature here is that while LDA and PBE achieve only modest reductions in the magnitude of the errors (between a quarter and a third), some functionals like the vdW-DF and BLYP functionals have local energetic errors that are roughly four times smaller than their corresponding global energetic errors.

As we discussed in Chapter 4, most GGA's are designed to give more accurate descriptions of bonding

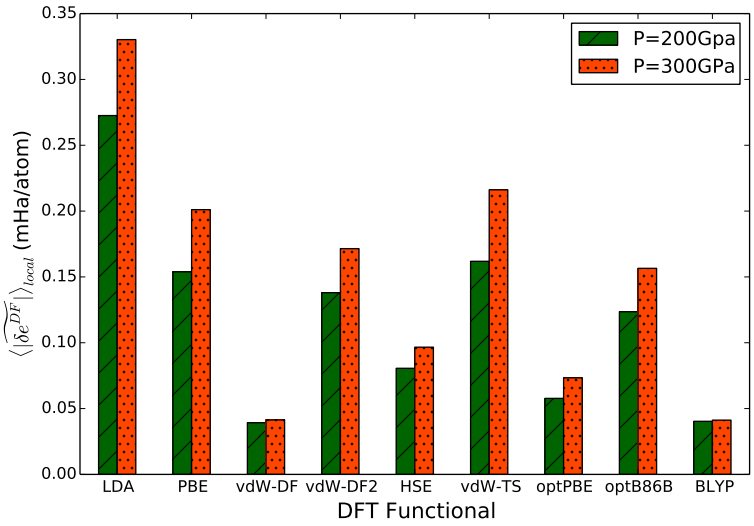

Figure 8.2: Averaged local energetic errors in solid hydrogen for a range of functionals, computed at two different densities.

over LDA. Given the energetic importance of the H_2 bond in all test sets except the liquid at $r_s = 1.30$, the improved performance of PBE over LDA, and BLYP over PBE, shouldn't come as a surprise. What was somewhat surprising is why the vdW-DF type functionals would perform so well. While it was originally suspected that van der Waals type interactions might be important in these dense systems [115, 15], we discuss in the hydrogen-helium chapter how the enhanced performance of vdW-DF is due more to its improved description of exchange than its inclusion of van der Waals interactions.

8.6.2 Pressures

In Figure 8.3, we plot the average pressure errors of density functionals on the liquid test sets (left) and solid test sets (right). We see that the functionals which were previously identified as having low energetic errors now have large pressure errors and visa versa. For example, LDA was one of the worst performing functionals energetically, but is the second best functional for estimating pressures among those we evaluated.

Interestingly, we found that in contrast to the energetic errors, the pressure errors have a statistically insignificant mean absolute deviation for any given test set. This implies that the pressure error depends more on the type of structure and density, rather than the particular details of the ionic coordinates. The highly systematic nature of these errors opens up the possibility of fitting the errors to simple functional forms and correcting them in post-processing.

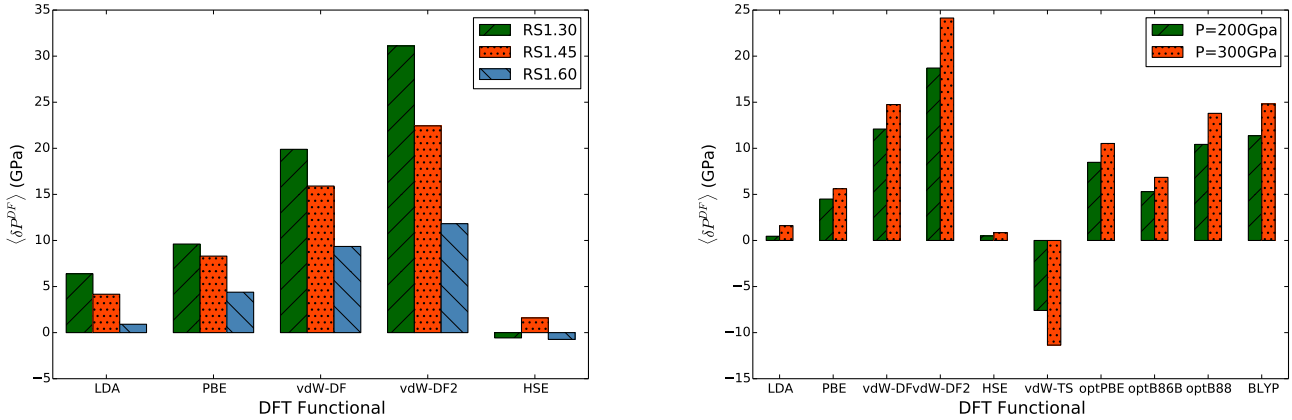

Figure 8.3: Average density functional pressure errors for (left) liquids at r_s=1.30, 1.45, and 1.60. (Right) Solids at densities corresponding to P^{DF}=200GPa, 300GPa.

8.7 Discussion

Now that we have quantified the magnitudes and trends of density functional errors for both energies and pressures, our goal is to try to use this information to predict how functionals can improve the accuracy of realistic equation of state calculations. To this end, we investigate the workflow of computing the ground state structures of hydrogen within the quasi-harmonic approximation, and how one can mitigate the errors stemming from the choice of approximate exchange-correlation functional.

8.7.1 Ground State Structures

Due to hydrogen's small x-ray scattering cross-section, x-ray diffraction studies have so far been unable to resolve any of the crystal structures of hydrogen above 150GPa. This means that a theoretical prediction of the atomic-to-molecular transition in dense solid hydrogen at zero temperature has to rely on structures identified in *ab initio* random structure searching (AIRSS) studies [116, 117]. For each identified structure, we calculate the enthalpy $H = E + P\Omega$ as a function of pressure (also known as a "cold curve"), and use this to read off the lowest enthalpy structure at any pressure. The largest density functional errors obviously enter through the calculation of P and E. However, even before calculating the energy and pressure, one needs to optimize the ionic coordinates and box geometry with some functional. This introduces a secondary source of DFT error through the ground state structure.

In Figure 8.4, we show DMC cold curves for several proposed ground state structures of hydrogen. The time step, number of walkers, number of atoms, and Monkhorst-Pack grid are identical to what was used in the benchmarking section. Finite-size corrections were done via 1/N extrapolations using $1 \times 1 \times 1$ and

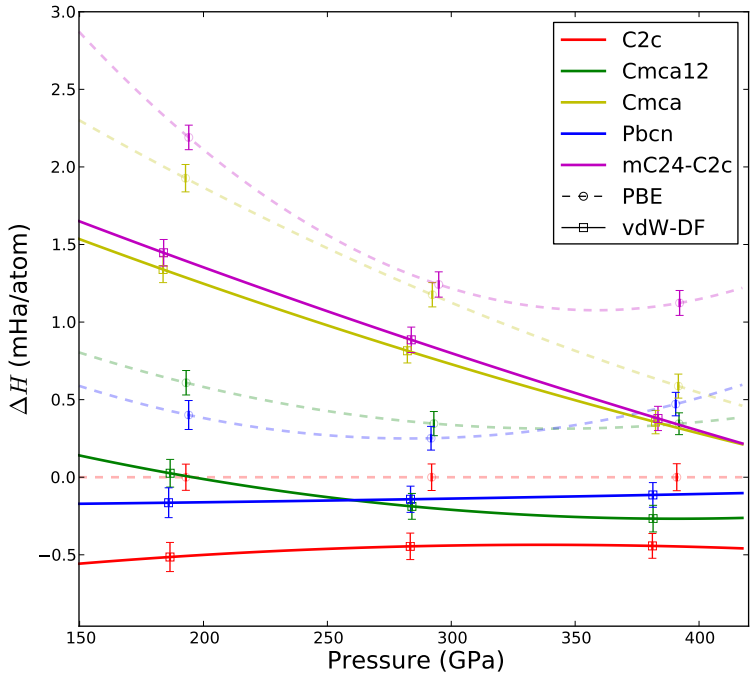

Figure 8.4: Relative DMC enthalpy as a function of pressure for several proposed ground state hydrogen structures. The colors denote the ground state structure, whereas the marker symbols denote the functional used to calculate the ground state structure. All enthalpies are computed relative to the PBE $C2/c$ structure.

$2 \times 2 \times 2$ supercells. The colors indicate the different structures, whereas the solid/dashed lines represent the density functional used to optimize the ground state structure. Structures were optimized at P^{DF}=200, 300 and 400GPa. We find that even when we use DMC to calculate the ground state enthalpies of candidate structures, there is a large sensitivity to the choice of functional used to optimize the structure. Structures optimized using vdW-DF produce ground state enthalpies that are at least 0.5mHa/atom lower than those optimized with PBE. While some have argued that error cancellation between different phases will render this energetic effect unimportant, we see from this figure that the assertion is incorrect [118]. For example, the DMC cold curve calculated using PBE structures indicates that the enthalpy difference between the $Cmca$ and $mC24 - C2/c$ structures vanishes near P=400GPa, wheras the DMC cold curve with vdW-DF structures indicates a 0.5mHa/atom difference between these two phases at P=400GPa.

Of course, we don't know that vdW-DF produces the correct structures. In this case, we have to rely on a variational principle for the enthalpy of ground state structures. We might not know if we have the correct answer, but we certainly know which functionals give us better or worse structures by comparing the enthalpies. Until we can perform structure optimization directly within QMC, screening density functionals for use in structure optimization is one way to significantly reduce systematic errors.

8.7.2 Vibrational Properties

To compute the nuclear zero-point energy within the quasi-harmonic approximation, two things are required. First, the minimum energy structure from DFT must be as close to the true minimum as possible. This was discussed in the previous section. Secondly, the force constant matrix needs to be as accurate as possible. These two allow us to accurately compute the normal modes of the system, and therefore the nuclear zero-point energy contribution to the enthalpy. Intuitively, we would expect functionals with smaller local energetic errors to give us better vibrational properties and correspondingly better zero-point energies. Lets see how this holds in practice.

For each molecular solid structure, we introduced a scaling factor into the bond length. This was used to either lengthen or shorten all H_2 bonds while preserving the overall symmetry of the structure. We used correlated sampling within RMC (via the BOPIMC code [119, 120, 121]) to compute the energy difference between the original configuration and configurations with scaled bond lengths. A time step of $\tau = 0.01 Ha^{-1}$ and a projection time of $\beta = 1.0 Ha^{-1}$ were used. Twist averaging was performed over on a $4 \times 4 \times 4$ Monkhorst-Pack grid.

The above allows us to construct a function $E^{QMC}(\ell)$, where ℓ is the bond length, and $E^{QMC}(\ell)$ is a one dimensional function corresponding to the QMC energy of a structure as we vary the H_2 bond length ℓ.

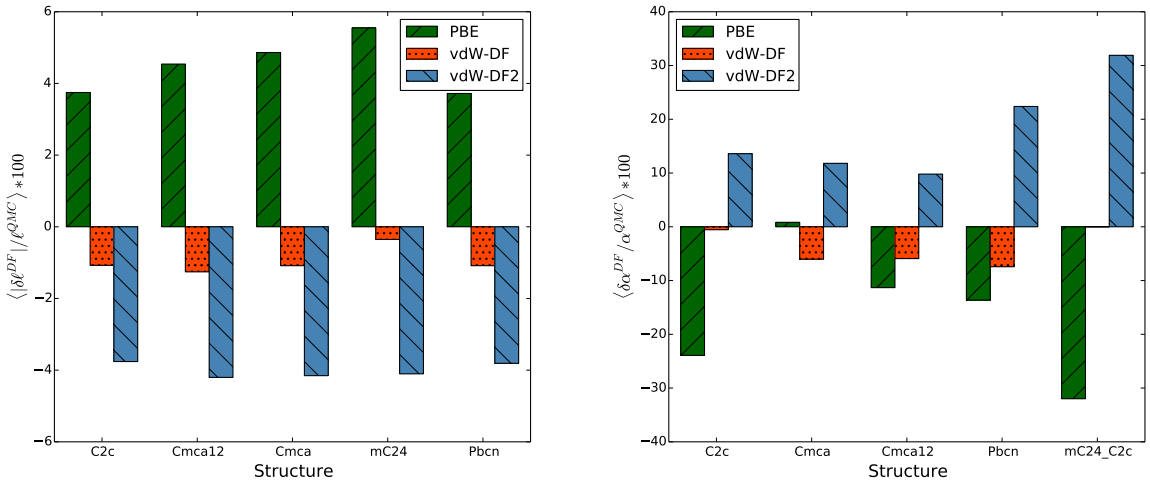

Figure 8.5: (Left) Relative error in H_2 bond length ℓ measured relative to QMC optimized value. The x-axis denotes the structure, and colors denote the functional used to relax the initial structure. (Right) Relative error in the second derivative of $E(\ell)$, evaluated at the QMC optimized ℓ. In both plots, the x-axis denotes the symmetry of the structure and the colors represent the density functionals used to optimize the initial structure. The data in both figures average over pressures.

From this fit, we can compute the estimated QMC bond length ℓ^{QMC} by finding the minimum of E^{QMC}. We can also compute the curvature of $E^{QMC}(\ell)$, which is defined as $\frac{d^2}{d\ell^2} E^{QMC}(\ell)|_{\ell=\ell^{QMC}}$. Analogous definitions are used for the different density functionals.

In Figure 8.5, we plot the errors in the equilibrium bond length (left) and curvatures (right) associated with several different hydrogen structures. For simplicity, we only compare three functionals: PBE, vdW-DF, and vdW-DF2. Considering the errors in bond length first, we see that vdW-DF underestimates the bond length by approximately 1%, whereas vdW-DF2 underestimates it by approximately 4%. PBE overestimates it by approximately 5%. While vdW-DF overbinds the H_2 molecules, vdW-DF2 does so more strongly, whereas PBE greatly underbinds the H_2 molecules. This finding is encouraging, since it is consistent with the previous section which found that the vdW-DF functional produced ground state structures with lower enthalpies than PBE or vdW-DF2.

Turning now to the errors in the curvature, we find that vdW-DF on average is the most accurate with an average error of approximately 5%. The sign indicates that the curvature is slightly smaller than QMC would predict. As one expects from the discussion on bond lengths, PBE predicts a significantly lower curvature than QMC, whereas vdW-DF2 predicts a significantly larger curvature. The unsigned error for both of these functionals ranges between 10% and 20%. The error incurred here is particularly important, since the curvature is closely related to the zero-point energy associated with the H_2 vibron. By using

vdW-DF to optimize the structures and calculate vibrational properties, one can dramatically reduce the error relative to PBE.

Chapter 9

Molecular-to-Atomic Transition in H

9.1 Introduction

Synthesizing solid metallic hydrogen in a diamond anvil cell has attained the status of "holy grail" in high pressure physics since Wigner and Huntington predicted its existence in 1935 based on scaling arguments [10]. While these scaling arguments are still valid, experimentalists have found no robust signature of metallic hydrogen in solid hydrogen up to pressures of 420GPa.

DFT-only calculations based on PBE and the quasi-harmonic approximation disagree noticeably with experiment regarding the structural transitions in dense hydrogen, as well as the insulator-to-metal transition. Calculations based on PBE predict a transition from phase III to the $Cmca-12$ structure around 280GPa. Since $Cmca-12$ is metallic at these pressures, this implies a structure driven insulator-to-metal transition, something which has not been observed in practice. The treatment of nuclear quantum effects at finite temperature via PIMD drives this transition to even lower pressures [16].

We attempt to reconcile theory with experiment by focusing on the atomic-to-molecular transition in solid hydrogen. Specifically, we seek to answer if phase III of hydrogen transitions directly into an atomic phase, or whether one or more intermediate molecular phases with different symmetries emerge between phase III and the atomic phase. Establishing the correct phases are a necessary prerequisite for answering the following questions: is the insulator-to-metal transition in solid hydrogen coincident with the molecular-to-atomic structural transition, or does the band-gap close within some molecular phase before the onset of molecular dissociation?

In this chapter, we present our published prediction for the atomic-to-molecular transition in zero-temperature solid hydrogen [1]. On the surface, our approach follows the traditional procedure for calculating a quasi-harmonic zero-temperature equation of state. Where we differ from previous methods is our painstaking attempt to estimate, control, and mitigate the major sources of error that enter into these calculations. For example, we use quantum Monte Carlo to compute the energies, pressures, and enthalpies of the most energetically favorable structures proposed so far for hydrogen. In situations where we could not

use QMC directly due to computational cost, we used insights from our QMC benchmarking work to reduce the error arising from DFT. We will conclude by comparing our predictions against recent experimental results.

9.2 Computational Details

All enthalpies in this work were computed using DMC energies and pressures at zero temperature. All simulations used the Slater-Jastrow trial wave functions described in the previous chapter. Time steps and population sizes were adjusted to insure that the energy and pressure errors were less than 0.01mHa/atom and 0.2GPa respectively. Finite size effects were handled through twist averaging and 1/N extrapolations. The atomic unit cells contained 4 atoms, so we used a $24 \times 24 \times 24$ Monkhorst-Pack grid. The 1/N extrapolation was performed using $2 \times 2 \times 2$, $3 \times 3 \times 3$, and $4 \times 4 \times 4$ supercells. The molecular phases all had 96 atoms in the simulation cell. We used a $6 \times 6 \times 6$ Monkhorst-Pack grid for twist-averaging. $1 \times 1 \times 1$ and $2 \times 2 \times 2$ supercells were used for the 1/N extrapolation. We expect the statistical errors arising from the finite-size correction to be the dominant error, which is between 0.07-0.1mHa/atom for the enthalpy.

For the atomic structures, we only considered the $\beta - Sn$ and $Cs - IV$ structures identified in previous structure searching work [122], since these were the only structures found to have competitive enthalpies under 1TPa. We chose several volumes corresponding to a pressure range of between 450GPa and 700GPa. Since the only free parameter to describe these structures is the c/a ratio, we were able to optimize the c/a ratio at each volume "by hand". This was done by calculating the DMC energy using several different c/a values, and then finding the minimum.

For the molecular phases, we considered the $C2/c$, $Cmca$, and $Cmca-12$ structures at pressures between 200-800GPa. From our hydrogen benchmarking study, we determined that the vdW-DF density functional was the most accurate functional available for optimizing the ground-state structures.

The nuclear quantum effects were computed within the quasi-harmonic approximation. We used the frozen-phonon method [54] implemented in the code Phonopy [123]. The force constant matrix was computed in VASP using the vdW-DF functional. To control for finite-size effects, the ion-displacements were performed in supercells of 768 and 432 atoms for the molecular and atomic phases respectively. Convergence of the zero-point energy and vibrational density of states were checked against supercells of 2592 and 1600 atoms for the molecular and atomic cells respectively.

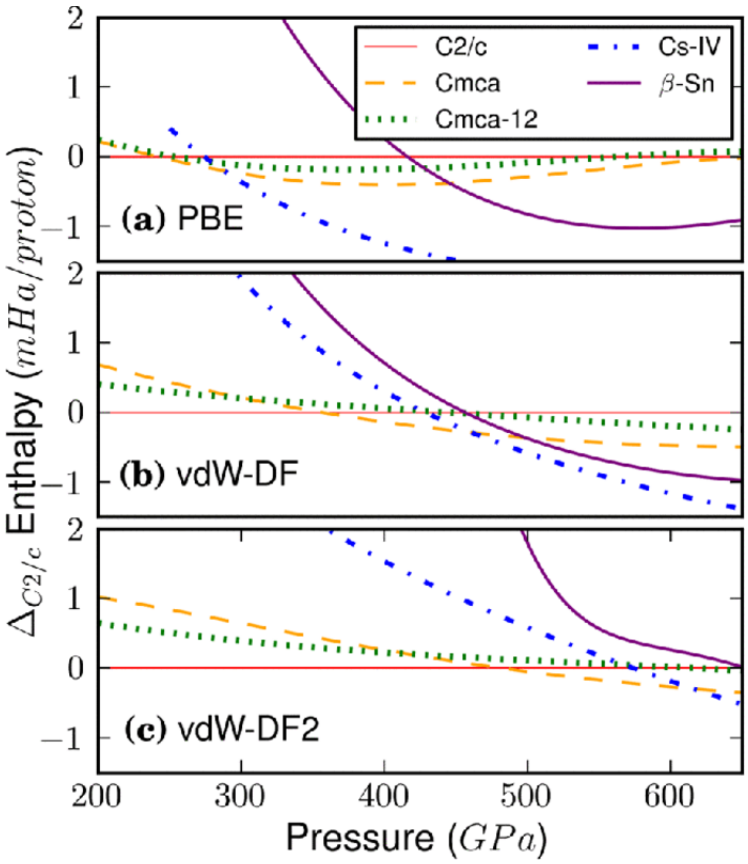

Figure 9.1: Plots of DFT enthalpy relative to $C2/c$ structure for likely atomic and molecular solid structures. Structures, energies, pressures, and zero-point corrections were computed using the a) PBE functional, b) vdW-DF functional, and c) vdW-DF2 functional. Figure from [1].

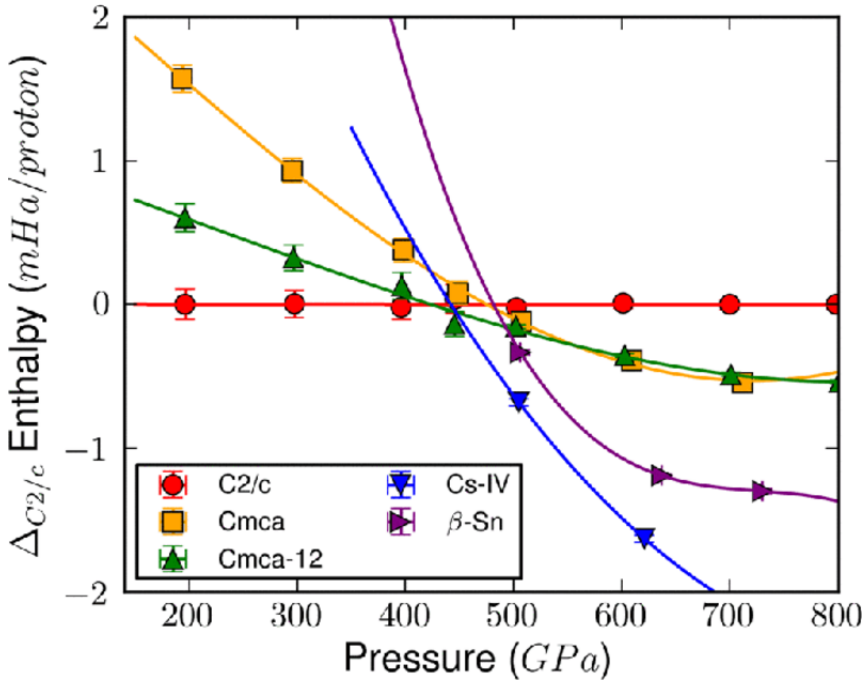

Figure 9.2: QMC enthalpy relative to $C2/c$ structure for likely atomic and molecular phases. Energies and pressures were computed with DMC, whereas the structures and zero-point corrections were computed with vdW-DF. Figure from [1].

9.3 Results

In Figure 9.1, we show the relative DFT enthalpy (with zero-point corrections) as a function of pressure for the various candidate atomic and molecular structures. The enthalpy, ground-state structures, and zero-point corrections were computed with PBE, vdW-DF, and vdW-DF2. We find that all density functionals qualitatively agree on the zero temperature ordering of phases as a function of pressure. As the pressure is increased, we find that hydrogen undergoes the following progression of phase transitions from phase III, which is believed to be the $C2/c$ structure, to the atomic phase: $C2c \rightarrow Cmca \rightarrow Cs-IV$. Thus, DFT predicts an intermediary molecular phase ($Cmca$) before molecular disassociation. Quantitatively, there are significant differences between the functionals. Using the $C2/c \rightarrow Cmca$ transition as an example, one can place this transition anywhere between 250GPa and 500GPa by changing the functional. If we decide to trust vdW-DF on the basis of our benchmarking study, it predicts a $C2/c \rightarrow Cmca$ transition at ∼350GPa, and then a $Cmca \rightarrow Cs-IV$ transition at ∼450GPa.

In Figure 9.2, we show the relative QMC enthalpies with vdW-DF based zero-point corrections. We see both quantitative and qualitative differences when comparing against the DFT results. QMC predicts the following sequence of phases from the observed to the atomic phase: $C2/c \rightarrow Cmca-12 \rightarrow Cs-IV$. Interestingly, $Cmca-12$ is predicted to be stable over a pressure range of 24(4)GPa, which though statistically

significant, is very small. The atomic-to-molecular is therefore predicted to be at 447(3)GPa using our QMC based approach.

9.4 Discussion

There are several reasons why we expect our calculations to be significantly more accurate than other predictions of the atomic-to-molecular transition to date. First, we explicitly mitigated errors arising from the generation of ground state structures, both through choosing more accurate functionals to optimize the molecular phases, and through direct QMC optimization of the atomic phases. We showed in the previous chapter how by not doing this, one can introduce non-cancelling errors of up to 0.5mHa/atom. Secondly, we improved the accuracy of the quasi-harmonic zero-point energies by choosing the most accurate functionals we could find. From the previous chapter, we expect the relative error in the zero-point energies to be at most 5%, whereas PBE can underestimate the energy by $10-20\%$. Lastly, we used 1/N extrapolations to perform the many-body finite-size corrections. Other works typically use the LDA based KZK finite-size correction, which by comparing with the 1/N extrapolations, we estimate incurs energy errors of approximately $\pm 0.5 mHa/atom$ [124].

A major approximation of our work is our neglect of anharmonic effects. Other groups have recently performed estimates of this, and have found that the anharmonic corrections to the $Cs-IV$ structure are approximately $-0.3 mHa/atom$. In contrast, the corrections to the molecular phases are between $+0.15 mHa/atom$ and $+0.3 mHa/atom$ [125]. This means that anharmonic effects will destabilize the molecular phases relative to the atomic phase, pushing the atomic-to-molecular transition towards lower pressures. A uniform shift of the molecular phases in Figure 9.2 upward by $0.6 mHa/atom$ would yield a molecular-to-atomic transition somewhere in the ballpark of 400GPa. The authors who originally computed the anharmonic corrections neglected to compute them for the $C2/c$ phase, but if it is comparable to the $Cmca-12$ anharmonic correction, this should eliminate the intermediary $Cmca-12$ phase, implying that the atomic-to-molecular transition will be direct from $C2/c \rightarrow Cs-IV$.

When these results were published, they seemed to square very well with what was then known about the low-temperature phase diagram of hydrogen. Specifically, diamond anvil cell experiments had gone up to pressures of 320GPa at cryogenic conditions and found that hydrogen remained in phase III [126]. By measuring the absorption edge and extrapolating the direct gap to zero as a function of pressure, this group made the prediction that solid hydrogen would metallize around 450GPa. We did not put forth an authoritative prediction of the insulator-to-metal transition in this work, since that would have required

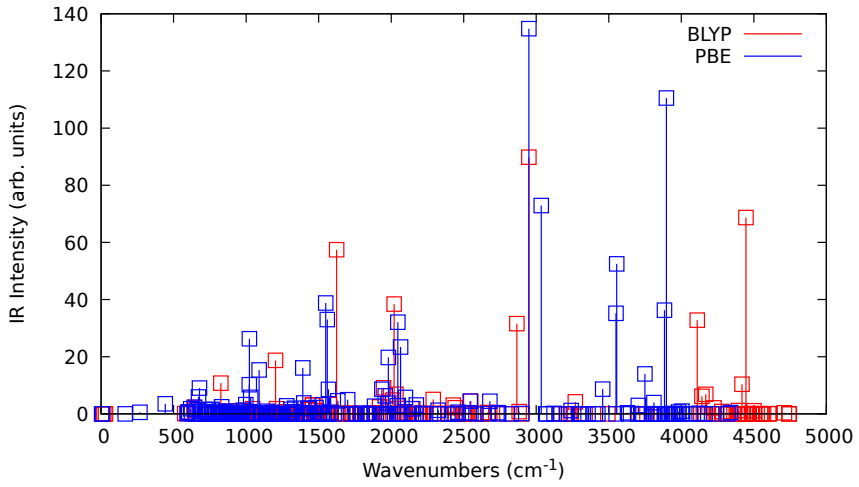

Figure 9.3: Infrared absorption spectrum for $Cmca-12$ structure, calculated within the quasi-harmonic approximation. Red and blue symbols denote spectra calculated with BLYP and PBE respectively.

carefully grappling with several technical points. However, noting that the static lattice direct band gap of $C2/c$ is more than 1eV at 500GPa and zero for all other molecular and atomic structures considered, our results would imply an abrupt insulator-to-metal as soon as hydrogen transitions out of the $C2/c$ phase. This would be around 425GPa, which is significantly better than the PBE estimates of 250GPa.

Recently, a study by Dias et. al has reached pressures up to 420GPa using a diamond anvil cell [127]. They found a transition at 355GPa from phase III to a non-metallic phase. This was identified by the sudden onset of three peaks in the infrared absorption spectrum between $2750-4500cm^{-1}$ and a disappearance of the vibron mode near $4000cm^{-1}$. This is a bit troubling from a theoretical point of view, since none of the likely candidate structures considered here or in other works are non-metallic in this range of pressures. This highlights a major approximation in *ab initio* calculations of hydrogen–we assume that we have constructed and considered all possible phases. It is possible that hydrogen might have a structure which has not previously been identified.

To explore the properties in this pressure range, we computed the infrared absorption spectra for the $C2/c$, $Cmca-12$, $Cmca$, and $Pbcn$ phases at a pressure of 350GPa. We used the PBE functional and BLYP to compute the phonon modes and dielectric tensor within density functional perturbation theory. BLYP was chosen because it is very similar to vdW-DF energetically and was one of the few functionals implemented for IR absorption calculations. We show the IR absorption spectrum for $Cmca-12$ in Figure 9.3. We found that only the $Cmca-12$ structure has 3 infrared active modes in the $2750-4500cm^{-1}$ window to qualitatively match what this group found. Quantitatively, Dias found the following three IR modes at 350GPa: $2875cm^{-1}$, $3375cm^{-1}$, and $4375cm^{-1}$. Using the BLYP functional, we find that the $Cmca-12$

modes should be at $2900cm^{-1}$, $4110cm^{-1}$, and $4430cm^{-1}$. Using PBE, we find the modes at $2990cm^{-1}$, $3550cm^{-1}$, and $3890cm^{-1}$. It seems as though either functional quantitatively predicts two out of three modes: BLYP predicts the lowest and highest modes relatively well, whereas PBE predicts the lowest and middle modes.

9.5 Conclusion

From our calculations of the infrared absorption spectrum of $Cmca-12$, it is possible that there is a molecular-molecular transition from phase III into a non-metallic $Cmca-12$. However, the agreement between the calculated and measured spectra is not good enough to establish a definite identification. At the very least, we need to wait until the Raman spectrum of this new phase is measured. If $Cmca-12$ is the correct ground-state phase at 355GPa, it is possible that the discrepancy between our results and the experimental results could be due to the neglect of anharmonic effects, as well as to residual errors in the treatment of electron-correlation.

It is possible that the new phase of hydrogen could be the result of some systematic experimental errors. To reach these extreme pressures, experimental groups either have to employ tricks to delay the hydrogen embrittlement of the diamonds, or resign themselves to replacing the diamonds whenever they break (which is often). The experiment by Dias *et al.* takes the former approach by placing coating of alumina on the diamonds to prevent hydrogen diffusion [127]. While this does not invalidate the results, it invites several questions to which there are not satisfactory answers at this time. Specifically, what is the solubility of alumina, copper, or other coatings in hydrogen at high pressures? If the coatings allow for the diffusion of impurities into hydrogen, how can this affect the structure and optical properties of hydrogen? In 2011, a group using similar techniques claimed to have synthesized metallic hydrogen in a diamond anvil cell, a claim which was not reproducible [128, 129].

Chapter 10

Hydrogen-Helium Benchmarking

10.1 Introduction

Though the phase diagram of hydrogen-helium mixtures has not had the same level of attention as that of pure hydrogen, an accurate phase diagram for hydrogen-helium mixtures is crucial for constructing models of Jovian planets and brown dwarfs. These objects are over 90% hydrogen, with helium concentrations on the order of 10%. While the helium concentrations are relatively small, whether or not is is able to mix with hydrogen has profound implications on the mass distribution, mass transport, and energy dissipation mechanisms in Jovian planets [18]. It is expected that major phase boundaries in the hydrogen/helium equation of state should be accurate to better than 1% to be predictive in planetary models [5].

Unfortunately, current *ab initio* phase diagrams for hydrogen-helium have not yet reached the required level of accuracy to be predictive. The two limiting sources of error for these systems are the treatment of the entropy of mixing and the treatment of exchange correlation effects. Nearly all simulations of hydrogen-helium mixtures treat the entropy approximately using the "ideal mixing approximation". It is possible to eliminate this approximation through the use of thermodynamic integration. It has been shown that doing so produces qualitative differences from ideal mixing results, as well as as quantitative differences amounting to approximately 1000K in the demixing transition at higher pressures [19, 21, 20]. In contrast, the errors arising from the choice of density functional have up to now been unquantified. Nearly all recent studies have used the PBE functional, which as we saw in hydrogen, is far from optimal.

In this chapter, we will present the results of our published work [130] to quantify the errors incurred by density functionals in areas of the phase diagram relevant for hydrogen-helium immiscibility. In addition to the local/global energetic and pressure errors we studied for hydrogen, we will look at errors in relative energies, relative enthalpies, and forces. The latter quantities will be particularly important, since whether or not hydrogen and helium will phase separate is determined from plots of the difference between the Gibbs free energy of the mixture and the Gibbs free energies of the pure phases. We will conclude this chapter by discussing the insights we gained into the cause of observed trends in density functional errors.

10.2 Constructing Test Sets

Since our goal is to benchmark the errors incurred by density functionals in areas of the phase diagram relevant for the immsicibility transition in Jovian planets, we chose a temperature of T=7000K and densities of r_s=1.10a_0, 1.25a_0, and 1.34a_0 to construct our test sets. We define the helium molar fraction as:

$$x_{He} = \frac{N_{He}}{N_{He} + N_H} \tag{10.1}$$

We consider systems with helium fractions ranging between $x_{He} = 0 - 20.7\%$ and $x_{He} = 100\%$. We use $N_e = 64$ for all simulations and adjust the number of hydrogen and helium atoms based on the concentration and charge neutrality constraint.

Using the above parameters for our simulation cells, we constructed the test sets by taking statistically uncorrelated samples from PBE molecular dynamics simulations in the NVT ensemble. Each test set corresponding to a given density and helium concentration contains at least 20 configurations.

To obtain the QMC reference values, we used single Slater-Jastrow wave functions without backflow of the form described in Chapter 7. For the single particle orbitals, we used PWSCF with the PBE functional. We chose a plane wave cutoff of 200Ry, and used Troullier-Martins pseudopotentials to eliminate the hydrogen and helium coulomb divergences.

Energies, pressures, and the fluctuation structure factor were computed using VMC and RMC. For target error bars of 0.008mHa/electron and 0.3GPa, we found that we needed a time step of $\tau = 0.0075 Ha^{-1}$ and projection time of $\beta = 4.5 Ha^{-1}$ for all configurations except where $x_{He} = 1$. For $x_{He} = 1$, we ran simulations with $\tau = 0.0075 Ha^{-1}$ and $\tau = 0.00375 Ha^{-1}$ in order to extrapolate all observables to $\tau = 0$. The projection time remained the same.

Forces were computed for each configuration using the Chiesa scheme described in Chapter 6. Forces were computed using DMC with $\tau = 0.01 Ha^{-1}$ and 512 walkers. Extrapolated estimates were used to reduce the mixed-estimator bias. We used a real-space cutoff of $\mathcal{R} = 1.0 a_0$ and polynomial degree $M = 3$. Between the statistical error bars, real-space grid, mixed-estimator bias, and finite-size effects, we expect the forces on the hydrogen atoms to be accurate to within 2mHa/bohr. We found that this resolution was sufficient to distinguish between different choices of functionals.

Single-particle finite size effects were handled by twist averaging on a $4 \times 4 \times 4$ Monkhorst-Pack grid. We included the single-particle Fermi surface correction described in Chapter 7. Additionally, we used the correlation function method described in Chapter **??** for all finite-size corrections.

10.3 DFT Details

In this study, we dramatically enlarged the set of functionals we tested. For semilocal GGA's, we considered LDA, PBE, BLYP, revPBE, PBEsol, and Wu-Cohen. For non-local vdW functionals, we considered vdW-DF, vdW-DF2, vdW-DF-C09, vdW-DF2-C09 [77], vdW-DF-CX [76], vdW-DF-optB88 [78], and vdW-DF-optB86b [131]. The only hybrid functional tested was HSE. We also branched out and tested two metaGGA functionals: TPSS and M06L [132, 133].

Due to the high densities in this work, we used PWSCF for all functionals except HSE, since we were able to generate and use hard all-electron Troullier-Martins pseudopotentials for both H and He atoms. The H and He atom pseudopotentials had cutoffs of $r_c = 0.37a_0$ and $r_c = 0.5a_0$ respectively. We used a plane wave cutoff of 800Ry and a $7 \times 7 \times 7$ Monkhorst-Pack grid with offset for all PWSCF functional calculations.

For the HSE functional, we had to make some compromises at the expense of accuracy to be able to run on the available computers. Due to poor parallelization of PWSCF for exact-exchange calculations, we used VASP instead. This unfortunately limited us to rather large PAW pseudopotentials which tend to lose accuracy as the potentials overlap. The largest Monkhorst-Pack grid we could afford was a $5 \times 5 \times 5$ grid, using a plane wave cutoff of 1500eV and 96 bands. We were also unable to run at the highest density because of numerical instabilities with VASP. We assessed the errors incurred by these cost-saving measures by comparing a VASP PBE calculation at r_s=1.25a_0 and r_s=1.34a_0 using the same Monkhorst-Pack grid, plane wave cutoff, and number of bands as the HSE calculation against the fully converged PBE calculations in PWSCF. We found that we introduce an error as large as 1.5mHa/atom for total energies and 1GPa for pressures at r_s=1.25a_0 by using the reduced Monkhorst-Pack grid and energy cutoff. The errors are significantly reduced at r_s=1.34a_0.

10.4 Error Measures

All methods used to quantify density functional errors for energies and pressures are nearly identical to the ones used in our hydrogen benchmarking study. The only difference is a slight redefinition of the terms "global" and "local" energetic errors. In hydrogen-helium mixtures, we choose the c^{DF} for global energetic errors by building an aggregated test of all helium concentrations at a particular density. For local energetic errors, different c^{DF} values are chosen for each test set at a particular density and helium concentration.

In addition to the error measures we defined in the hydrogen benchmarking study, we had to devise new error measures to deal with the large amount of data coming from the forces. Let $\mathbf{f}_i$ denote the force on ion i, and let $\mathbf{F} = \{\mathbf{f}_0, \ldots, \mathbf{f}_{N-1}\}$. The first error we define is an ensemble mean absolute force error, given by

$\langle|\delta\mathbf{f}^{\alpha}|\rangle_S$. Here, $\delta\mathbf{f}_{i_\alpha} = \mathbf{f}_{i_\alpha}^{DFT} - \mathbf{f}_{i_\alpha}^{QMC}$ and α denotes the ionic species. It is assumed that the mean absolute force errors for all atoms of the same species are averaged.

With a bit of care, we can also define consistent mean force errors. Let $\mathbf{r}_{i_\mu j_\nu} = \mathbf{r}_{i_\mu} - \mathbf{r}_{i_\nu}$. We define the mean force error between atoms of species μ and ν with the following:

$$\langle \delta f_{\mu-\nu}^{DF}(r)\rangle = \frac{\int d\mathbf{R} e^{-\beta E^{PBE}(\mathbf{R})}\delta(r - r_{i_\mu j_\nu})\,\hat{\mathbf{r}}_{i_\mu j_\nu}\cdot\delta\mathbf{f}_{i_\mu}^{DF}}{\int d\mathbf{R} e^{-\beta E^{PBE}(\mathbf{R})}\delta(r - r_{i_\mu j_\nu})} \tag{10.2}$$

$E^{PBE}(\mathbf{R})$ is the PBE potential energy surface, which is the distribution that the test sets were sampled from. By definition, the above error measure is positive if it overbinds the $\mu-\nu$ interaction, and negative if it underbinds.

Intuitively, we expect that force errors will change the local structure of hydrogen-helium mixtures. If the $H-H$ interaction is overbound, for example, we would expect the average $H-H$ separation to be smaller than in the correct answer. This intuitive reasoning can be made rigorous through the "potential of mean force" $w(r)$ [134]. It is defined as $g_{\mu\nu}(r) = \exp(-\beta w_{\mu\nu}(r))$, where $g_{\mu\nu}(r)$ is the $\mu-\nu$ pair correlation function. If we replace $E^{PBE}(\mathbf{R})$ with $E^{QMC}(\mathbf{R})$, the density functional errors could be related to the errors in the potential of mean force with the following:

$$\langle \delta f_{\mu-\nu}^{DF}(r)\rangle_{QMC} = -\frac{\partial}{\partial r}\delta w_{\mu\nu}^{DF}(r) \tag{10.3}$$

10.5 Results

10.5.1 Energetics

Plotted in the left of Figure 10.1, we show the global energetic errors averaged over helium concentration for all tested functionals. For the most part, we see similar qualitative trends as were previously noted in the hydrogen benchmarking work. Functionals like LDA and vdW-DF2 perform poorly, whereas functionals such as vdW-DF and BLYP perform well. The inclusion of far more functionals allows us to speak more reliably about trends in families of functionals. The functionals designed for computing accurate lattice constants and bulk moduli in solids, like PBEsol and Wu-Cohen, are some of the least accurate functionals for energetics. In contrast, functionals which were designed to capture accurate atomization energies are among the most accurate. For example, revPBE is found to be comparable to BLYP in terms of accuracy. Surprisingly, the non-local van der Waals functionals failed to exhibit such clear trends. In particular, vdW-DF-C09 and vdW-DF2-C09 use different functionals for the non-local correlation energy, yet are nearly indistinguishable

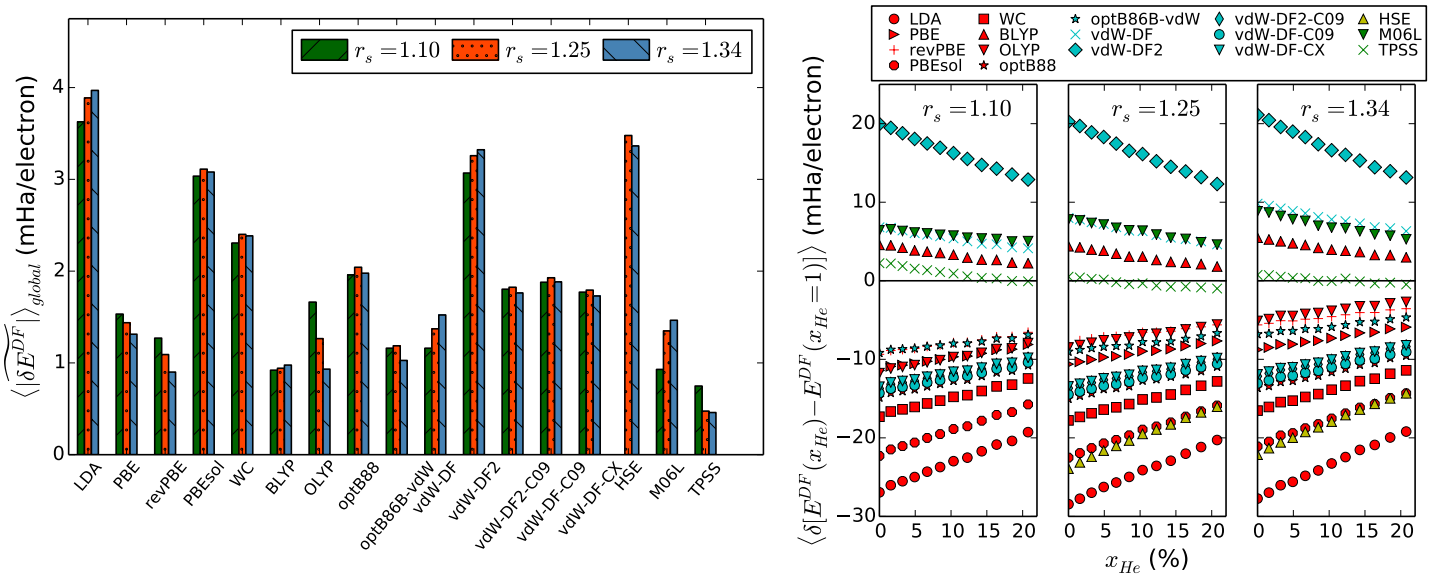

Figure 10.1: (Left) Plot of global energetic errors for all tested functionals, averaged over all helium concentrations. (Right) Mean error of $E(x_{He}) - E(x_{He} = 1)$ as a function of helium concentration. From left to right, the densities are r_s=1.10a_0, 1.25a_0, and 1.34a_0. The colors and markers denote the functional class and particular functional respectively. Red is GGA, blue is non-local vdW, green is metaGGA, and yellow is hybrid.

here. This seems to suggest that most of the variance between the different non-local functionals arises from the choice of exchange-enhancement factor used in the "outer functional".

In addition to helping understand the trends between different families of functionals, this figure also allowed us to flag the metaGGA class of functionals as a potentially more accurate alternative to non-local vdW and hybrid functionals. We see that the TPSS functional in particular has half the global energetic error of BLYP, which would otherwise have been the best performing functional for these systems.

In the right of Figure 10.1, we show how the mean error in $E(x_{He}) - E(x_{He} = 1)$ varies as we change the concentration of helium. The smoothness of the mean energy error as a function of helium concentration is surprising. Additionally, with the exception of the TPSS errors, which crosses the x-axis at least once, all functionals seem to have errors that are either monotonically increasing or decreasing towards 0 as $x_{He} \to 1$. This seems to suggest that we could easily fit these errors to some low-order polynomial and correct the energetics in post-processing.

10.5.2 Pressures

In the left side of Figure 10.2, we plot the relative mean pressure error averaged over all helium concentrations for all tested functionals. We show the results for three different densities. As we saw in the hydrogen benchmarking work, the pressure errors are strongly anti-correlated with the energetic errors. PBESol,

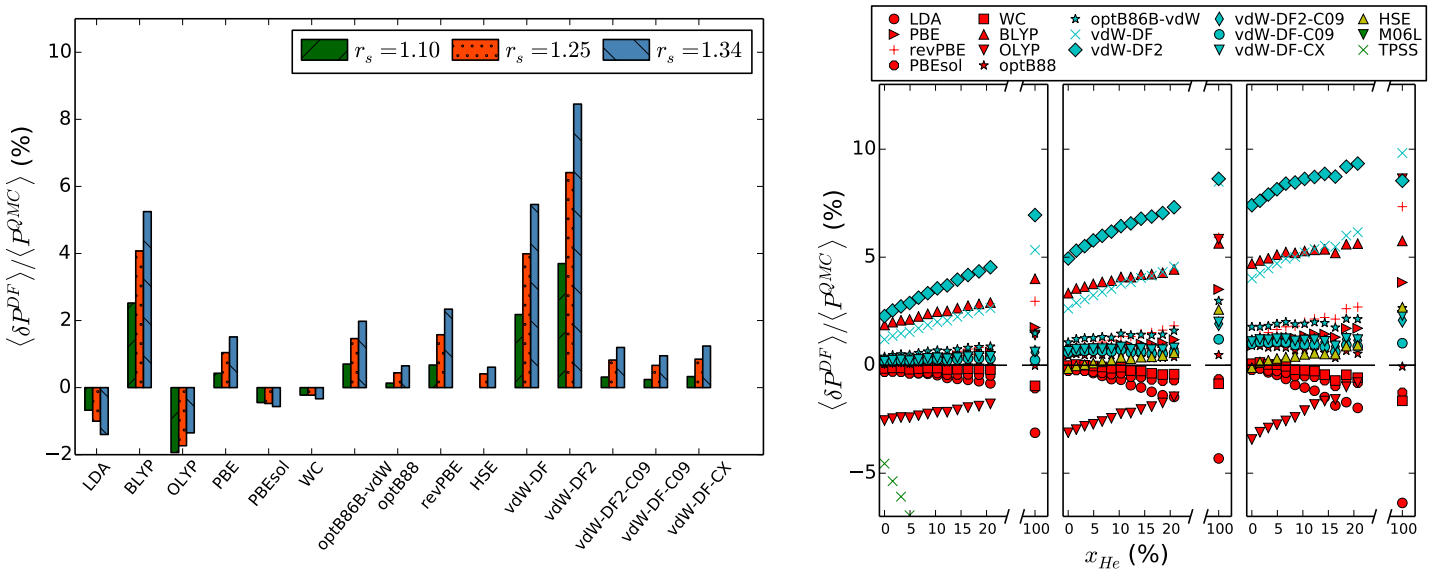

Figure 10.2: (Left) Mean pressure errors for all tested functions, averaged over all helium concentrations. (Right) Mean pressure error as a function of helium concentration at fixed density. From left to right, the densities are r_s=1.10a_0, 1.25a_0, and 1.34a_0. The colors and markers denote the functional class and particular functional respectively. We use the same layout and marker convention as in Figure 10.1.

Wu-Cohen, HSE, and LDA seem to be the best performing functionals, whereas vdW-DF, vdW-DF2, and BLYP are the worst performing ones pictured. We did not include the TPSS and M06L functionals on this plot since their errors were -17% and -34% respectively. While we expect the trade-off between energies and pressures for GGA and non-local vdW functionals, it is not obvious that the metaGGA's should suffer similarly.

In the right side of Figure 10.2, we show how the relative pressure errors change as a function of helium concentration. While still somewhat smooth as a function of helium concentration, the error trends are a bit more unpredictable. PBEsol and Wu-Cohen are more accurate than nearly all functionals at all helium concentrations, but they both perform measurably better at smaller helium concentrations than at larger ones. While not the most accurate, vdW-DF-C09 exhibits surprisingly consistent errors, being nearly flat across all helium concentrations.

10.5.3 Enthalpies

In Figure 10.3, we plot the error in the relative enthalpy $H(x_{He}) - H(x_{He} = 1)$ for all tested functionals as a function of helium concentration. While this might seem redundant given that we have already discussed energy and pressure errors, our purpose here is to investigate to what extent these functionals benefit from error cancellation. We find that functionals like vdW-DF, LDA, and HSE can experience up to a

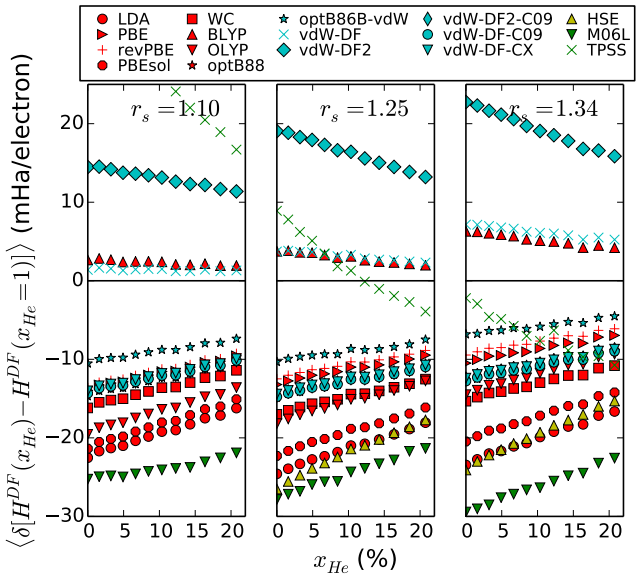

Figure 10.3: Mean error of $H(x_{He}) - H(x_{He} = 1)$ for all considered functionals. From left to right, the results at r_s=1.10a_0, 1.25a_0, and 1.34a_0 are shown. We use the same layout and marker convention as in Figure 10.1.

3-4mHa/electron reduction in the enthalpy errors relative to the energy errors, whereas some functionals like PBE and OLYP actually suffer from error *addition*.

10.5.4 Forces

In this section, we forgo discussing the mean absolute force errors, since the statistical noise is significant and is almost entirely consistent with our findings for the global energetics. We instead focus on how the mean force error $\langle \delta f^{DF}_{\mu-\nu} \rangle$ behaves as a function of helium concentration and density.

In Figure 10.4, we show the mean PBE force error for $H-H$, $H-He$, and $He-He$ forces as a function of r/r_s. The different color markers denote different densities: blue is r_s=1.10a_0, green is r_s=1.25a_0, and red is r_s=1.34a_0. $H-H$ and $H-He$ forces were computed using helium fractions of $x_{He} = 20.7\%$, whereas the $He-He$ forces were computed in configurations with $x_{He} = 100\%$. The striking factor here is the remarkable insensitivity of the mean force errors to the density. To put this in perspective, this density range corresponds pressures between 300GPa and 1.2TPa in pure hydrogen, and between 200GPa and 800GPa in pure helium.

In Figure 10.5, we show the mean PBE force errors for $H-H$, $H-He$, and $He-He$ forces as a function of r/r_s at density of r_s=1.25a_0. The different color markers now represent different helium concentrations. Again, we see a remarkable insensitivity in the all force error components to the helium concentration. Since pure hydrogen is metallic at these conditions and helium is insulating, we could transform our system from a metal to an insulator by changing the helium concentration. In principle, we would expect PBE to have

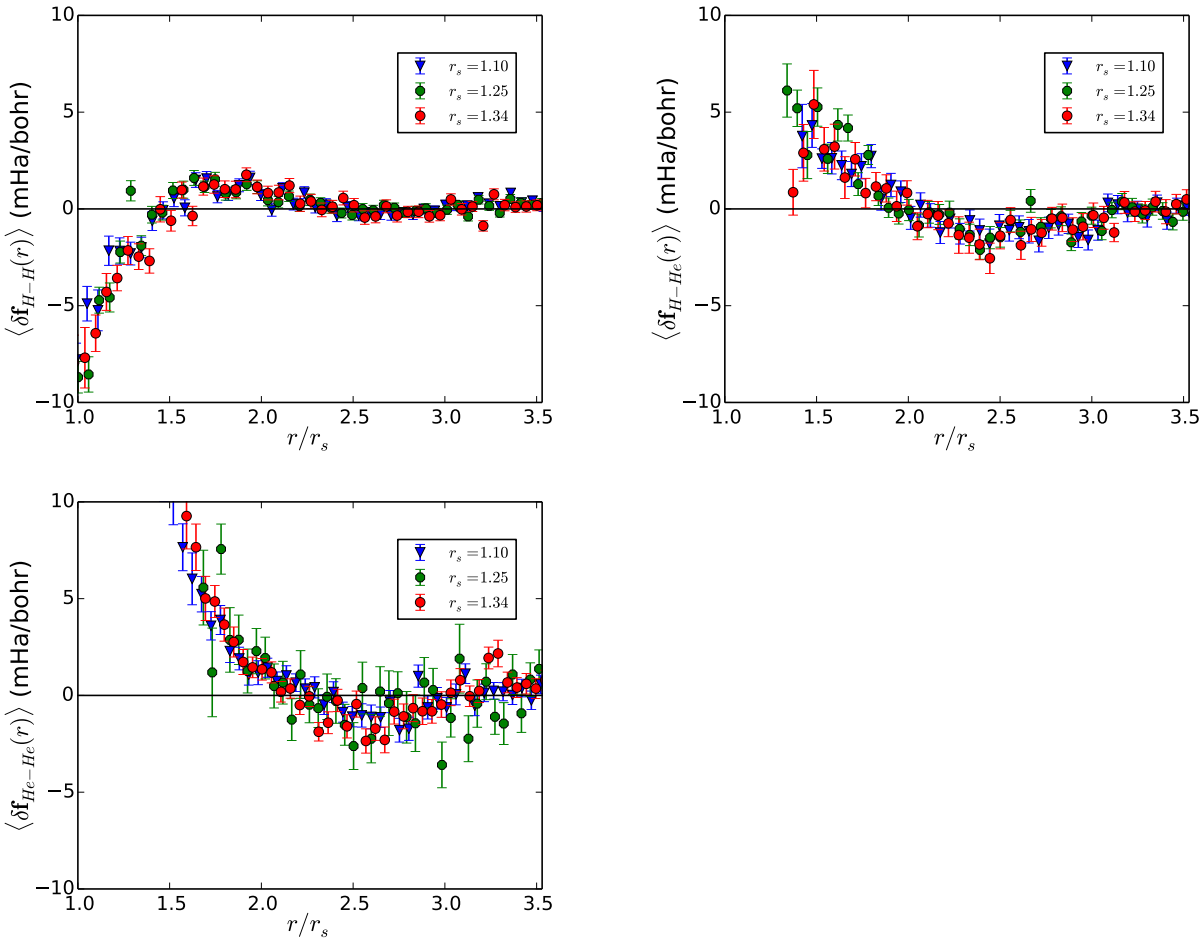

Figure 10.4: $\langle \delta f^{PBE}_{\mu-\nu}(r) \rangle$ vs. r/r_s as density is changed. The different marker colors/styles represent different densities. (Top) $\langle \delta f^{PBE}_{H-H}(r) \rangle$ calculated at $x_{He} = 20.7\%$, (middle) $\langle \delta f^{PBE}_{H-He}(r) \rangle$ calculated at $x_{He} = 20.7\%$, (middle) $\langle \delta f^{PBE}_{He-He}(r) \rangle$ calculated at $x_{He} = 100\%$

difficulties equitably describing states with such different electronic properties. Instead, the force errors seem so well behaved over both density and helium concentration that it suggests we might be able to noticeably improve molecular dynamics simulations of hydrogen-helium mixtures by fitting the $H-H$, $H-He$, and $He-He$ force errors to classical pair potentials, and then add these corrections to our DFT forces in post-processing. This would be very similar to the Grimme correction for van der Waals interactions.

Noting the above insensitivity in the force errors to helium concentration and density, we plot in Figure 10.6 the DFT force errors between all ionic species at a density of r_s=1.25a_0. To improve statistics, we use helium concentrations of $x_{He} = 1.6\%$, $x_{He} = 20.7\%$ and $x_{He} = 100\%$ for the $H-H$, $H-He$, and $He-He$ force components respectively.

In our hydrogen benchmarking study, we showed how functionals like vdW-DF and vdW-DF2 overbind

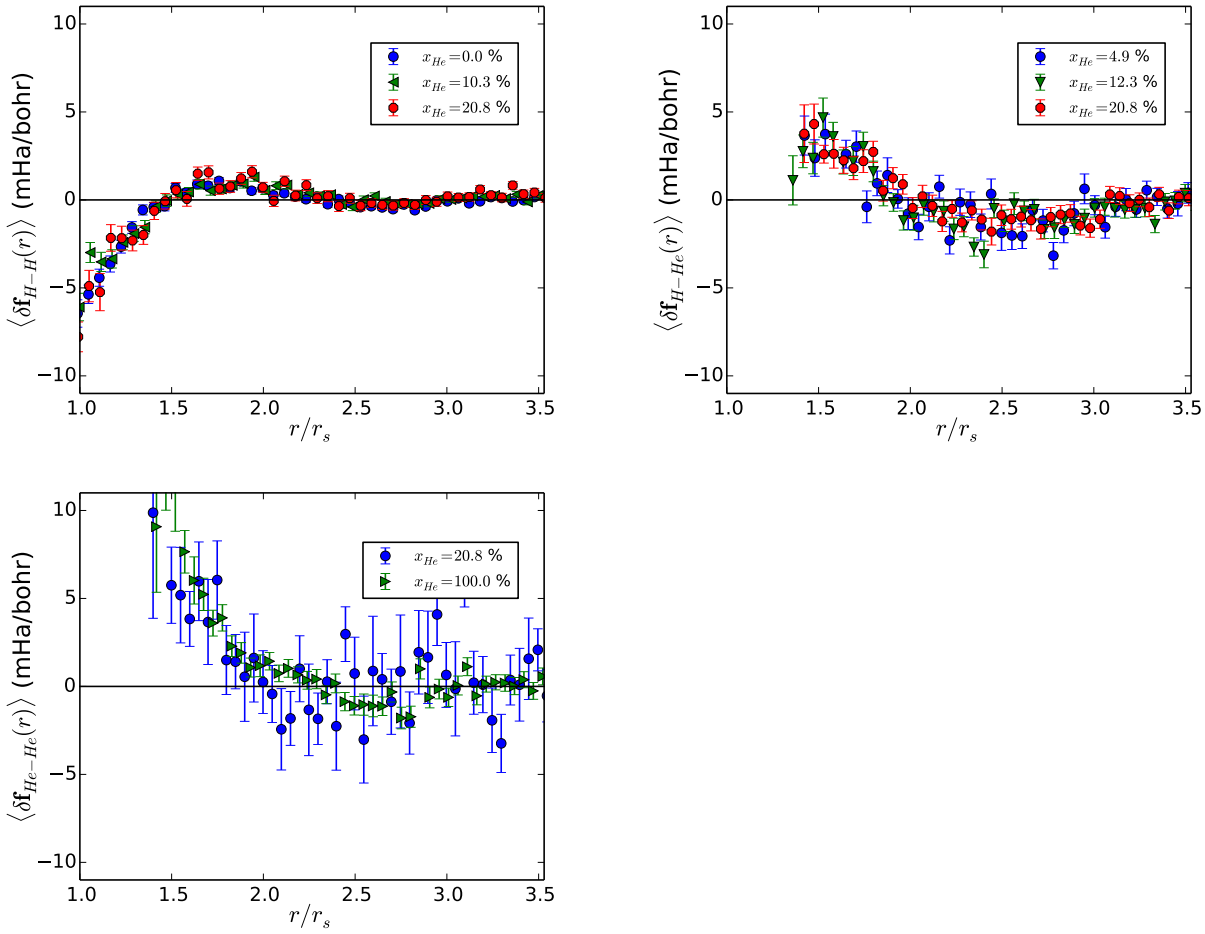

Figure 10.5: $\langle \delta f^{PBE}_{\mu-\nu}(r) \rangle$ vs. r/r_s as helium concentration is changed. The different marker colors/styles represent different helium concentrations. (Top) $\langle \delta f^{PBE}_{H-H}(r) \rangle$, (right) $\langle \delta f^{PBE}_{H-He}(r) \rangle$, (bottom) $\langle \delta f^{PBE}_{He-He}(r) \rangle$. All configurations are at a density of $r_s = 1.25$.

the $H-H$ interactions, whereas functionals like PBE underbind it. We can now see this explicitly by looking at $\langle \delta f^{DF}_{H-H}(r) \rangle$, particularly around the first nearest neighbor shell ($r/r_s \approx 1$). Notice the oscillatory behavior in the force errors. We attribute this to charge conservation–overbinding the H-H interaction indicates that the density functional is predicting larger than expected electronic charge densities between neighboring H atoms. This charge has to come from somewhere, which usually means that charge depletion in the second nearest neighbor shell will lead to these neighbors being underbound, and so on.

In contrast to the $H-H$ interaction, we see from $\langle \delta f^{DF}_{He-He}(r) \rangle$ that all functionals seem to underbind the $He-He$ interactions, albeit to differing degrees. Though the error bars are large, we see that the vdW-DF2 and vdW-DF functionals have the lowest errors for nearly all $He-He$ separations. This is encouraging, since we expect non-negligible van der Waals interactions in noble gas systems.

Lastly we look at $\langle \delta f^{DF}_{H-He}(r) \rangle$. We find that functionals which underbind the $H-H$ interaction seem to overbind the $H-He$ interaction, and visa versa. Interestingly, there are four functionals which seem to have negligible errors in describing the $H-He$ interaction: BLYP, TPSS, and HSE.

The takeaway from the force discussion is that we can extract a lot more information from simulations than we were able to with just energies and pressures. Forces give us a spatially resolved picture of how functionals perform. This will be indispensable moving into more complicated systems. Already in hydrogen-helium mixtures, we see that density functionals can provide inequitable descriptions of the different components.

10.6 Discussion

As a result of this work, we are finally in a position to understand the cause of the observed error trends.

First, we address to what extent the inclusion of non-local van der Waals effects are important for accurately describing high pressure hydrogen and helium. For systems which are mostly helium, these types of functionals are expected to be more accurate. However, most of the energetic gains we see in hydrogen with low concentrations of helium are not from the inclusion of van der Waals interactions. If the non-local van der Waals correlation were a necessary ingredient for describing these systems, a properly tuned vdW functional should perform better energetically than any GGA we could construct. Instead, we see that a properly chosen GGA like BLYP can nearly equal the best non-local vdW functionals for energies and forces. Additionally, as mentioned in the energetics section, the performance of the non-local van der Waals functionals is highly dependent on the choice of enhancement factor used in the "outer functional", and highly insensitive to the choice of non-local correlation functional. Comparing vdW-DF-C09 and vdW-DF2-C09, one sees that there are negligible differences between these functionals for estimating energies, pressures, and forces. This is in spite of them having two different forms of non-local correlation. We conclude then that the initial differences observed between vdW-DF and vdW-DF2 stem from their noticeably different choices of exchange functionals: revPBE for the former, and rPW86 for the latter.

Now we attempt to link the energetic errors to the underlying form of the exchange enhancement factor $F_X^{DF}(s)$, which was defined in section 4.4.2 of Chapter 4. We computed the reduced density gradient s on a real-space grid for a few configurations at each density and helium concentration. We found that s is bounded by $0 \leq s \leq 1.8$ for all densities and helium configurations. For pure hydrogen, this bound can be tightened to $0 \leq s \leq 0.8$.

We show in Figure 10.7 the exchange enhancement factors for several functionals over the relevant range

of s. To explain the energetic performance of the GGA's, recall that the accuracy of various GGA's ordered from best to worst was BLYP, revPBE, PBE, and PBEsol. Looking at the enhancement factors we find that for $0 < s \leq 0.8$, $F_X^{B88}(s) > F_X^{revPBE}(s) > F_X^{PBE}(s) > F_X^{PBEsol}(s)$. Recalling from section 4.4.2 that $F_X^{DF}(s) \approx \mu s^2$ in the small s limit, we note that for BLYP, revPBE, PBE, and PBEsol, μ is 0.2743, 0.235, 0.235, and 0.1234 respectively. This is not to say that one can keep increasing the value of $F_X^{DF}(s)$ to obtain better energetics. We note that BLYP and revPBE overbind and underbind hydrogen atoms respectively, indicating that the optimal exchange enhancement factor is between $F_X^{revPBE}(s)$ and $F_X^{B88}(s)$.

The interpretation of the non-local van der Waals performance is not as clean since there is a GGA exchange contribution coming from the non-local correlation functional. If we focus on underbinding vs. overbinding of the H-H interaction among DF type vdW functionals, we see that vdW-DF overbinds, optB86b-vdW underbinds slightly, and both vdW-DF-C09 and vdW-DF-CX underbind to the greatest extent. Looking at the enhancement factors, we find that $F_X^{revPBE}(s) > F_X^{optB86b}(s) > F_X^{C09}(s) > F_X^{CX}(s)$.

We discussed in Chapter 4 how the ability of a functional to accurately estimate pressures stems from its adherence to the "gradient expansion approximation" (GEA). While we originally thought that this was due to the functional obeying the correct $1 + \mu_{GEA} s^2$ behavior for small s (which PBEsol confirms), the Wu-Cohen functional stands as a counter example–recovering the GEA at larger s. In hindsight, this makes sense since the reduced density gradients for hydrogen/helium mixtures are peaked somewhere between 0.1 and 1.8 at these densities. We see that enforcing the $\mu = \mu_{GEA}$ constraint has the positive side effect of dragging down the values of $F_x^{DF}(s)$ at moderate s relative to energetically favorable functionals like B88 and revPBE. Interestingly, the non-local van der Waals functionals with the CX an C09 exchange experience significantly better pressures than vdW-DF, vdW-DF2, and optB86b-vdW counterparts. One notes that CX and $C09$ approximately obey the GEA at small s and have a similar scaling with s as PBEsol and Wu-Cohen.

10.7 Conclusion

The result of this extensive benchmarking study is that we believe we understand the dominant source of error in hydrogen and hydrogen-helium mixtures at extreme pressures. Specifically, our benchmarking results strongly suggest that the choice of the enhancement factor has the dominant contribution on the accuracy for energies and pressures, and not necessarily the choice of correlation functional. More importantly, this study helps show the limitations of the functionals we tested. For the GGA and non-local van der Waals functionals, it is highly unlikely that we will be able to improve significantly on the functionals we have

already tested. For the pressures however, it is likely that we might be able to reoptimize existing functionals to give us accurate pressures. Noting the improved consistency of the pressure errors in non-local van der Waals functionals over GGA functionals, one possible approach is to reoptimize the enhancement factor of $C09$ or the CX based functionals to give us a non-local van der Waals functional which is ideal for solids, analogous to the PBEsol and Wu-Cohen functionals.

This study also identified metaGGA functionals as a promising class of functionals for use in *ab initio* studies of high pressure systems. The energetics of TPSS are dramatically better than the best GGA and non-local van der Waals functionals we found. At the moment, it is not obvious how much more accurate one can make these functionals, but it is worth exploring. It might also be possible to simultaneously measure accurate energies and pressures with this type of functionals, since the metaGGA functional has far more degrees of freedom than the GGA's.

10.8 Figures

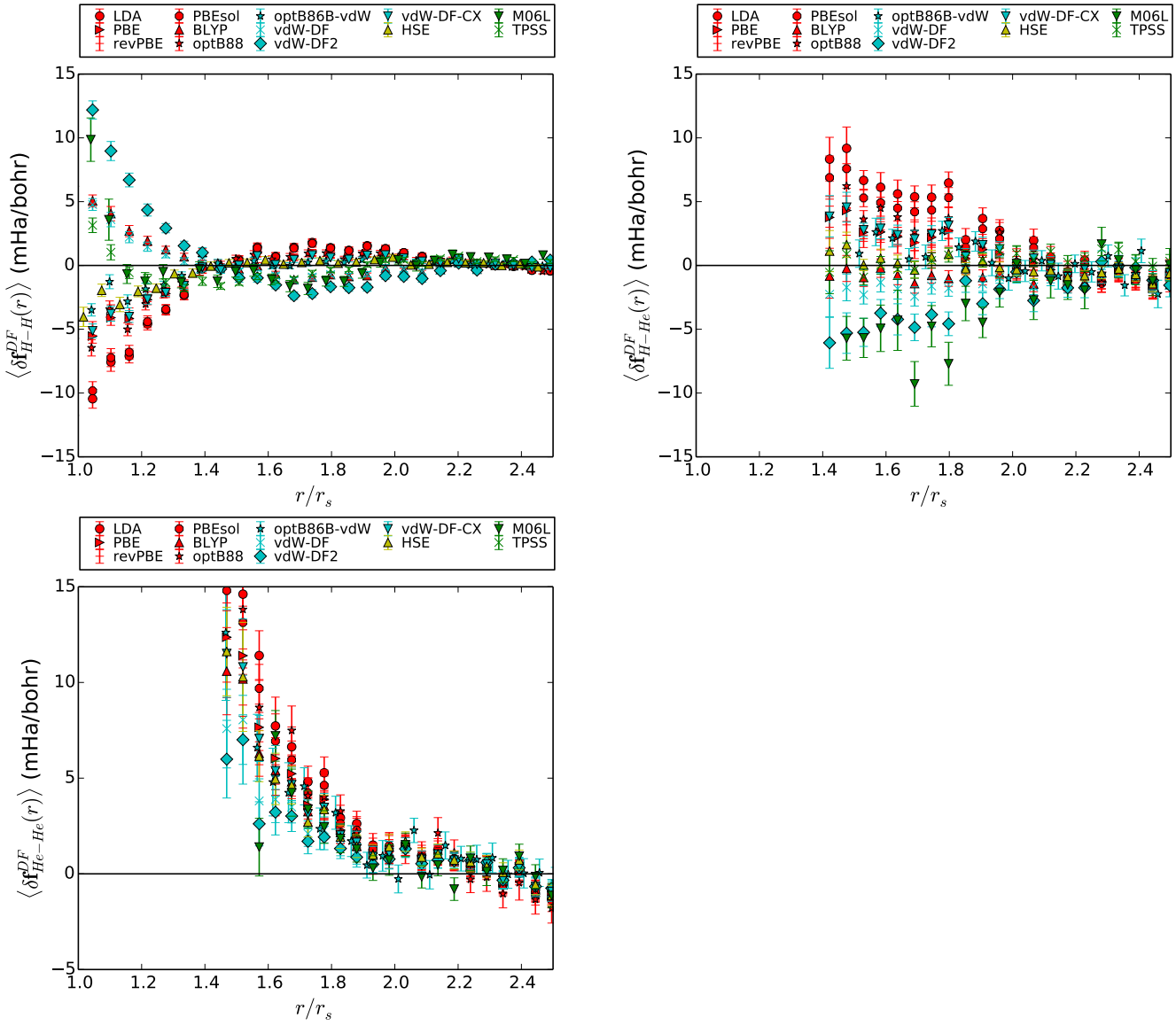

Figure 10.6: $\langle \delta f^{DF}_{\mu-\nu}(r) \rangle$ vs. r/r_s as the functional is changed. The different marker colors/styles represent different density functionals. (Top) $\langle \delta f^{PBE}_{H-H}(r) \rangle$ at $x_{He} = 1.6\%$, (right) $\langle \delta f^{PBE}_{H-He}(r) \rangle$ at $x_{He} = 20.7\%$, (bottom) $\langle \delta f^{PBE}_{He-He}(r) \rangle$ at $x_{He} = 100\%$. All configurations are at a density of r_s=1.25a_0.

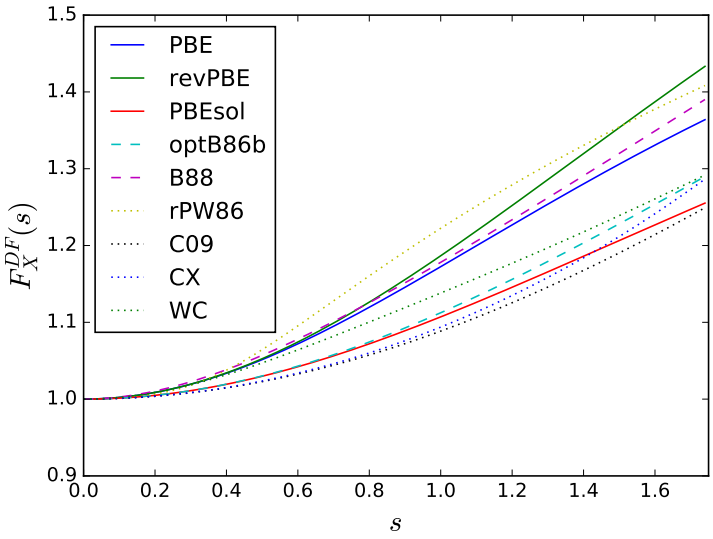

Figure 10.7: Plots of exchange enhancement factors $F_X^{DF}(s)$ versus reduced density gradient s.

Chapter 11

Immiscibility in Hydrogen-Helium Mixtures

11.1 Introduction

With our hydrogen-helium benchmarking results in hand, the most pressing question is how we can use this information to improve predictions of the immiscibility transition in hydrogen-helium mixtures. In this chapter, we attempt to study the sensitivity of the immiscibility line to the choice of density functional. We begin by presenting some basic definitions in the thermodynamics of mixtures. After discussing the computational details of our density functional and molecular dynamics simulations, we discuss the sensitivity of the energy, $P\Omega$ contribution to the enthalpy, and Gibbs free energy of mixing (within the ideal mixing approximation) to both the choice of density functional and finite-size effects. We find that a lot of our results are inconclusive, but conclude by discussing the next steps we are taking to definitively understand the impact of density functional on the immiscibility transition.

11.2 Thermodynamics of Mixtures

To establish if a specific hydrogen-helium mixture is miscible, let us begin by defining the Gibbs free energy of mixing at fixed temperature and pressure as:

$$\Delta G_{H+He}(x_{He}) = G_{H+He}(x_{He}) - [(1 - x_{He})G_H + x_{He}G_{He}] \tag{11.1}$$

$G_{H+He}(x_{He})$ is the Gibbs free energy of the mixture. G_H and G_{He} are the Gibbs free energies of pure hydrogen and pure helium respectively at the same pressure and temperature as the mixture. At helium concentrations where $\Delta G_{H+He}(x_{He}) > 0$, the mixture will phase separate into bubbles of pure helium and pure hydrogen. If $\Delta G_{H+He}(x_{He}) < 0$, this indicates that some type of mixture is stable. In the event that $\Delta G_{H+He}(x_{He})$ has one minimum in the range $0 < x_{He} < 1$, then this indicates that hydrogen and helium are miscible at all helium concentrations at this pressure and temperature. In the event there are two local minima, the mixture will phase separate into helium rich and helium depleted regions. The helium

concentrations of these regions can be found by a common tangent construction using $\Delta G_{H+He}(x_{He})$.

Pressures and energies are measured straightforwardly using molecular dynamics. The entropy contribution to the Gibbs free energy, in contrast, is commonly estimated using the ideal mixing approximation given as follows:

$$S_{id} = -k_b[x_{He}\ln(x_{He}) + (1-x_{He})\ln(1-x_{He})] \tag{11.2}$$

For what is detailed in this chapter, we will restrict ourselves to this approximation.

11.3 Computational Details

We performed all molecular dynamics simulations in a modified version of VASP. We used all electron PAW pseudopotentials for the hydrogen and helium atoms. Simulations were performed within the NPT ensemble. A Langevin thermostat was used to constrain the temperature to T=7000K. The pressure was fixed at a DFT pressure of P=500GPa by using an isotropic Berendsen thermostat [135]. This means that the box size and atomic positions were uniformly scaled to change the volume of the box dynamically. We tested the following functionals: PBE, PBEsol, revPBE, vdW-DF, vdW-DF2, and optB86b-vdW.

All simulations contained 256 electrons with 190 bands. The specific number of hydrogen and helium atoms determined by the helium concentration and constraint that the simulation cells be charge-neutral. Since this work is exploratory, we performed these simulations at the Γ-point. Production level calculations will undoubtedly require more k-points.

11.4 Density Functional Effects

In Figure 11.1, we begin by calculating the enthalpy of mixing $\Delta H_{H+He}(x_{He})$ as a function of helium concentration using all previously mentioned functionals. We see that at intermediate helium concentrations ($x_{He} = 0.2-0.8$), the enthalpy differences between various functionals can be as large as 1-2mHa/atom. From our benchmarking discussion, we expect the vdW-DF functional to produce the most accurate enthalpies here on account of decent energetics and error-cancellation from the $P^{DF}\Omega$ term.

For completeness, we look at the $P^{DF}\Omega$ contribution to the enthalpy in Figure 11.2. We note two features. First, all functionals except vdW-DF2 exhibit a flattening of the $P^{DF}\Omega$ contribution to the mixing enthalpy between $x_{He} = 0.3 - 0.6$. Secondly, calculating $P^{DF}\Omega$ with different functionals generates a noticeable spread. The difference between PBEsol and vdW-DF2 is as large as 1.5mHa/atom near $x_{He} = 0.6$.

Finally, in Figure 11.3 we compare the mixing Gibbs free energies $\Delta G_{H+He}(x_{He})$ for all tested functionals

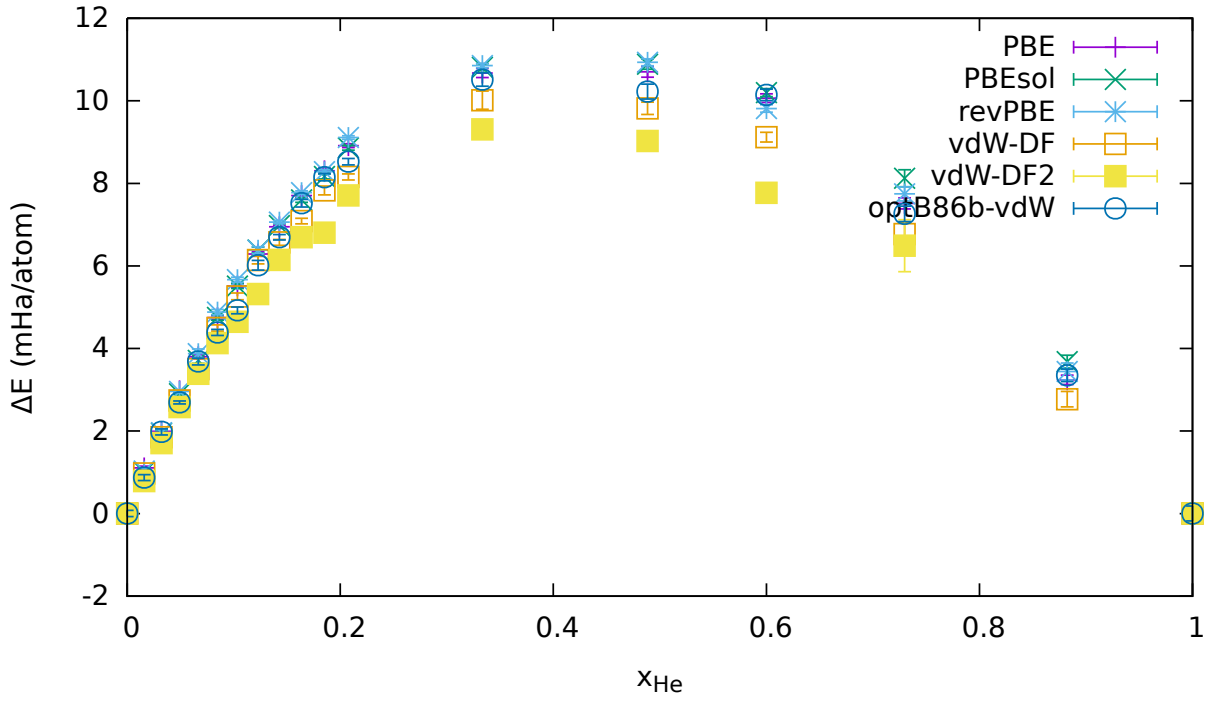

Figure 11.1: Plot of $\Delta H_{H+He}(x_{He})$ as a function of x_{He} at T=7000K and P^{DF}=500GPa. The different colors denote different density functionals. The ideal mixing approximation was used.

as a function of helium concentration. First thing to notice is that for most functionals, the noise is too large to establish if they predict immiscibility, and if so, what helium concentration the phase separated regions possess. This is most likely the result of picking a pressure and temperature already established to be very near the immiscibility transition [20, 19]. optB86b-vdW exhibits a clear signal between $x_{He} = 5 - 30\%$, predicting a helium depleted region with $x_{He} \approx 10\%$. vdW-DF2 seems to predict full miscibility. This would suggest we would estimate a higher temperature immiscibility transition with vdW-DF2 than with PBE. The others, while borderline, seem to suggest helium fractions between $x_{He} = 7 - 10\%$ based on the noise.

The second thing to notice is how much the Gibbs free energies of mixing vary with functional. Around $x_{He} = 60\%$, we see that the van der Waals functionals all have lower mixing free energies than the GGA functionals. In particular, vdW-DF2 is almost 3mHa/atom lower than all GGA's around $x_{He} = 60\%$. While we cannot accurately predict the correct helium fraction in the event of immiscibility for this pressure and temperature, the energetics seem to suggest that the van der Waals functionals render some sort of mixture more energetically favorable than the GGA would predict.

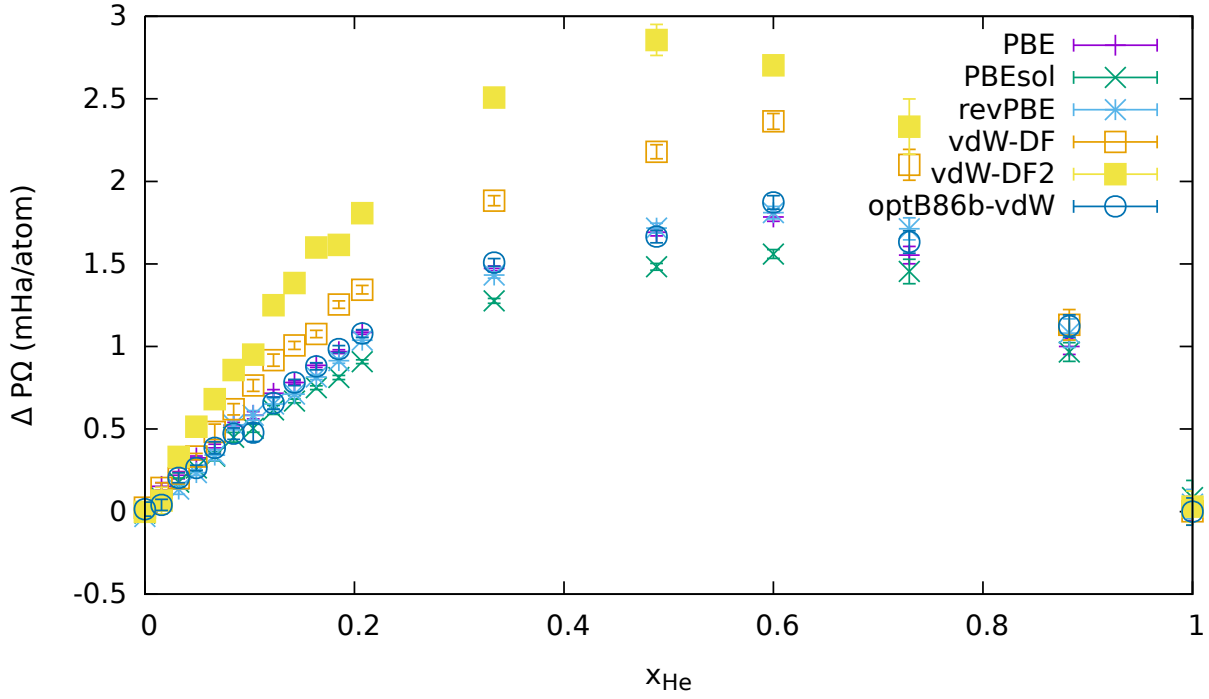

Figure 11.2: Plot of $\Delta[P^{DF}\Omega](x_{He})$ contribution to the enthalpy as a function of x_{He} at T=7000K and P^{DF}=500GPa. The different colors denote different density functionals.

11.5 Finite Size Effects

Assuming that we perform k-point integration on a large enough Monkhorst-Pack grid, we can eliminate the electronic finite size effects. Unfortunately, we still must deal with finite-size effects associated with the ions. The phase separation transition should be sensitive to the box size, but it is not yet clear to what extent. To try to estimate these effects, we considered supercells of 256, 512, and 1024 electrons. Due to the increased computational cost, we calculated these results on a reduced x_{He} grid. We show the results for the Gibbs free energy of mixing for the PBE functional in in Figure 11.4.

While the supercell calculations at $x_{He} \approx 10\%$ seem to converge to a value about 0.75mHa/atom larger than the 256 electron cell, the helium concentrations between $x_{He} = 30 - 60\%$ exhibit a disturbing failure to converge. This behavior was unexpected, but we can think of two causes for this. The first is probably an artifact of these simulations being performed at the gamma point. Without k-point averaging, we are likely seeing shell effects as were discussed in Chapter 7. Based on our validation of the HSE functional in the previous chapter, we expect that we need at least a $2 \times 2 \times 2$ Monkhorst-Pack grid in a 256 electron unit cell to converge local/global energetic errors to under 1mHa/atom. Other authors have suggested performing simulations at the Baldereschi point [20], but we need to independently verify the errors introduced with

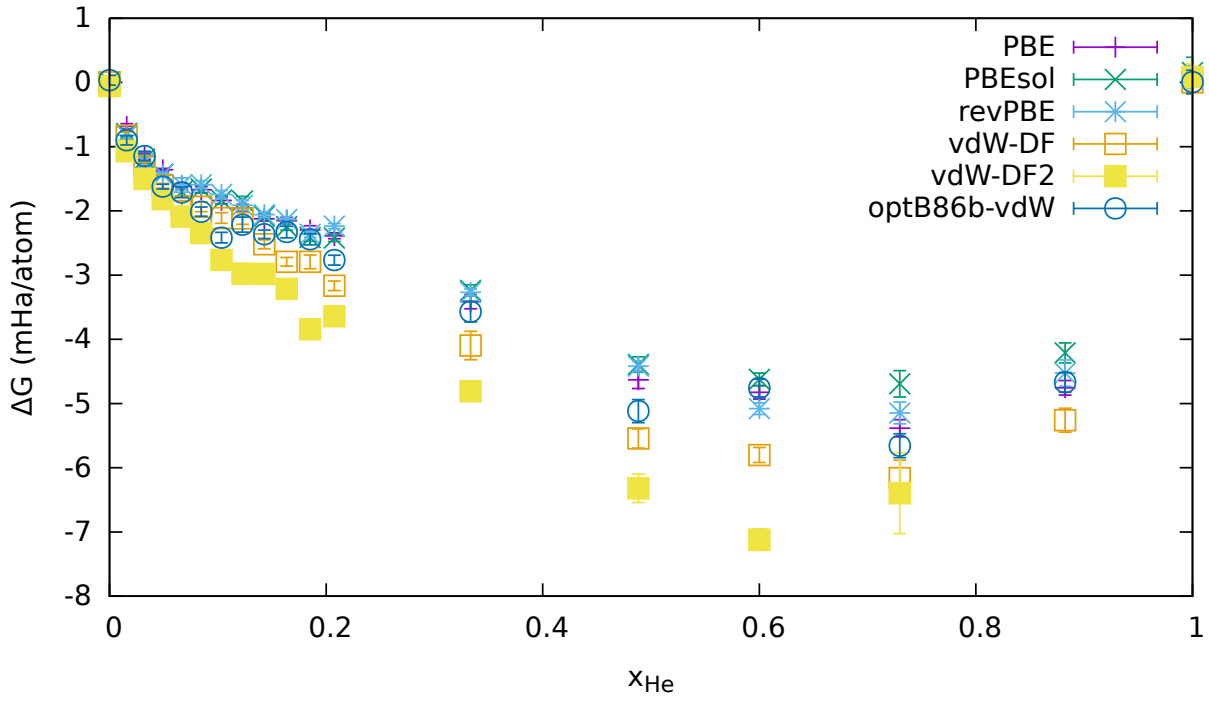

Figure 11.3: Plot of $\Delta G_{H+He}(x_{He})$ as a function of x_{He} at T=7000K and P^{DF}=500GPa. The different colors denote different density functionals. The ideal mixing approximation was used.

this method.

Another source of error could be the onset of phase-separation within our unit cells. Lorenzen *et al.* [136] observed phase separation in unit cells with 2046 electrons with a helium fraction of $x_{He} = 1/3$. While their pressures are significantly higher than ours (2000GPa), it nevertheless demonstrates that phase separation is possible in our unit cells–especially the largest ones. In the near future, our goal is to develop some heuristics to either confirm or rule out this hypothesis in our work. We hope that a signature can be found through some sort of clustering analysis.

11.6 Future Work

In this work, we confined ourselves to looking at the immiscibility transition within the ideal mixing approximation. While this does give us a feeling for the role that the energetic contributions will have in determining the immisiciblity transition, to be able to definitively answer the question of where the immiscibility transition is located, we have to establish the effect that the choice of density functional has on the entropy of mixing. This is done through the coupling-constant and thermodynamic integration methods described in Chapter 5 [19, 21].

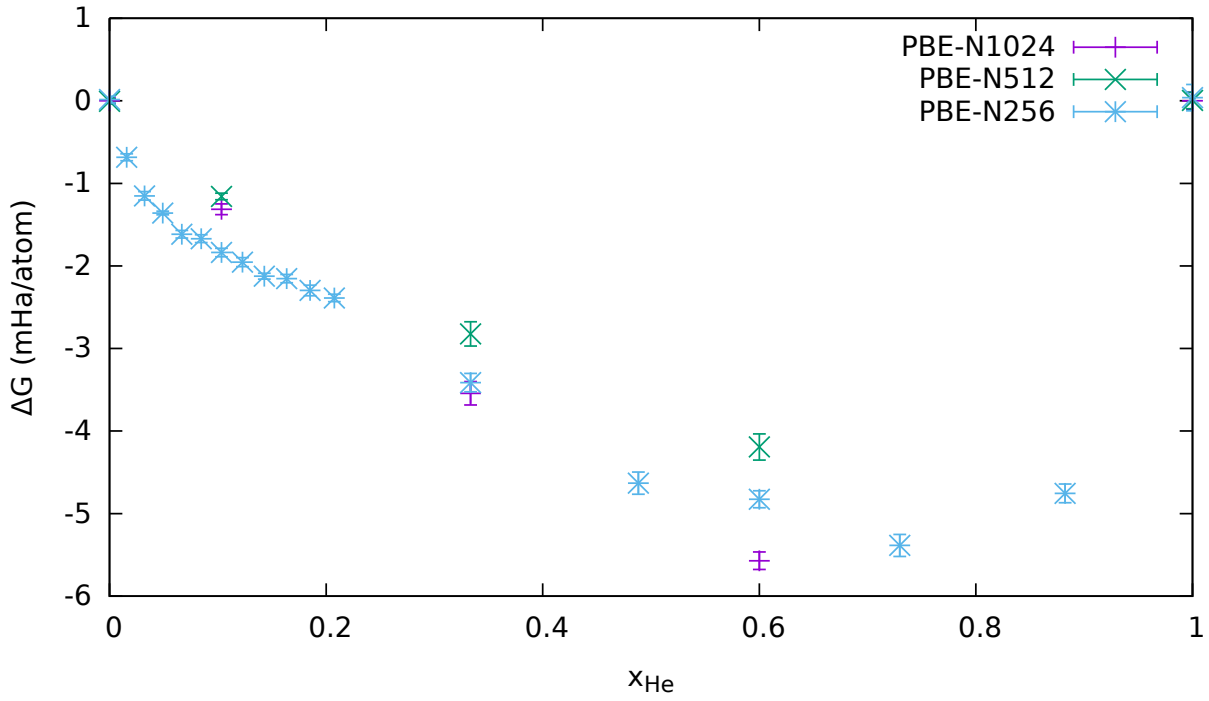

Figure 11.4: Plot of $\Delta G_{H+He}(x_{He})$ as a function of x_{He} at T=7000K and P^{DF}=500GPa. All energies are in mHa/atom. The different colors indicate different simulation cell sizes.

While conceptually straightforward, our choice of pressure and temperature complicated matters in that we are probably in a regime where hydrogen and helium are partially immiscible. This means that there will likely be issues with coupling-constant integration, as there is a phase transition between our non-interacting reference state and the physical state of the system. To get around this, we must calculate the free-energy at temperatures high enough where hydrogen and helium are miscible, and then use thermodynamic integration to calculate the free energies at lower temperatures. Since we were working within the NPT ensemble, we had to fix the volume of the simulation cells at a particular helium concentration to equal the average volume at T=7000K. We performed NVT molecular dynamics simulations T=7000K, 8000K, 9000K, 10,000K, and 11,000K on a reduced grid of helium concentrations. Coupling-constant integration was then performed for all helium concentrations at T=11,000K. At the time of writing this, the coupling-constant integration and the NVT runs had been completed for the PBE functional. We are in the process of carrying this out for PBEsol, vdW-DF, and vdW-DF2 functionals.

Chapter 12

Dense Lithium

12.1 Introduction

Very little attention has been paid to the phase diagram of lithium above 150GPa. Our understanding of the phase diagram beyond 150GPa is largely determined by two different works. The first is an *ab initio* structure searching study by Pickard *et al.* [26], which identified a slew of possible lithium structures and computed quasi-harmonic cold curves for all phases up to 600GPa. The second is from Tamblyn *et al.* [28], which found that molten lithium had a low coordination number, forming long-lived tetrahedral clusters from $P \approx 150GPa$ up to the highest considered pressure of $P \approx 800GPa$.

Currently, there are no published results predicting the melting line of dense lithium above 200GPa. This is significant because before we can ask what role nuclear quantum effects and anharmonicity have on the phase diagram, we need to roughly know where the important phase boundaries are. ^{7}Li is still light enough that these effects could be large. In hydrogen for instance, nuclear quantum effects are large enough to cause the melting line to have a negative slope at pressures above 800GPa [137]. This, coupled with a potential mismatch between the electronic structure of the liquid and solid phases, could potentially conspire to produce a melting line at low temperatures or even one with a negative slope.

Before computing the phase diagram, we conducted an exploratory study to establish the impact that nuclear quantum effects and exchange correlation functional has on the qualitative properties of the proposed liquid and solid phases of dense lithium. For example, it is currently not known to what extent the tetrahedral clusters are robust in the liquid phase to both nuclear quantum effects and choice of exchange correlation functional. It is also not known how stable the classically proposed structures would be to the inclusion of nuclear quantum effects. We begin this chapter investigating these effects. Then we compute the phase diagram of lithium between 200-600GPa using thermodynamic integration with the assumption of classical nuclei.

12.2 Computational Details

All simulations were performed using a modified version of VASP [111, 112]. DFT calculations were performed using an all electron PBE PAW pseudopotential for lithium which eliminated the nuclear cusp. Previous work has highlighted the possibility that some commonly used PAW pseudopotentials could fail at high pressures on account of a poor description of the 1s core [138]. To ensure the accuracy of our pseudopotentials, we constructed a hard-core ($r_{cut} = 0.5a_0$) PBE Troullier-Martins pseudopotential with OPIUM. Cold curves were then calculated using our PAW pseudopotential in VASP and the Troullier-Martins pseudopotential in PWSCF over the listed target pressure range. We computed the pressure as a function of volume between pressures corresponding to 200GPa and 600GPa. We found that the error in the pressure was under 3GPa at the highest densities.

To establish a reference from which to compare the impact of nuclear quantum effects and exchange correlation effects, we began by performing quantum molecular dynamics simulations in both the liquid and solid phases of dense lithium with classical nuclei. We chose a uniform grid of temperatures and pressures spanning 500-2000K and 200-600GPa. The grid spacings were 300K and 100GPa for temperature and pressure respectively. Due to its prevalence in the literature, we used the PBE exchange correlation functional within the Mermin finite temperature framework. We used the Nosé-Hoover thermostat in all classical simulations.

All QMD simulations with classical nuclei were performed at the Γ-point using 108 Li atoms. We considered the following structures for solid lithium: hcp, fcc, $Imma$, $Cmca-24$, $R\bar{3}m$, $P4_2mbc$, $Aba2$ [26]. For each structure, the unit cell was tiled in such a way as to ensure that the simulation supercell was as close to cubic as possible. These tilings produced supercells with anywhere between 72 atoms for $Imma$ and 144 atoms for $R\bar{3}m$. All solid simulations were performed at the Γ-point. To deal with the finite-size errors incurred by the lack of k-point averaging, we drew 10 snapshots at each pressure for both liquid and solid structures. We then computed the average energy and pressure of our Γ-point calculations to those on a $4 \times 4 \times 4$ Monkhorst-Pack grid. We computed ensemble finite size corrections for each structure and pressure using these "converged" energies and pressures.

To calculate nuclear quantum effects at the Born-Oppenheimer level, we used path-integral molecular dynamics (PIMD) in the NVT ensemble. Using a Langevin thermostat, we chose an imaginary time step of $\tau = 0.13$fs to propagate the ring polymers. We found that eight time slices at T=500K was enough to converge the kinetic and potential energy of ^{7}Li to within 0.2mHa/atom. As the temperature was increased, the number of time slices M was reduced to keep β/M constant. We performed these simulations on the same grid used in the classical simulations. We simulated the liquid phase and the following restricted set

of solids: $Cmca-24$, $P4_2mbc$, $R\bar{3}m$, and $Aba2$. Particle numbers and k-point sampling are identical to the classical MD runs.

12.3 Role of Exchange and Nuclear Quantum Effects

12.3.1 Exchange-Correlation Effects

Assuming classical nuclei, we first look at the role that the exchange correlation functional has in changing the local structure and dynamics of dense lithium in the liquid phase. We forego a detailed benchmark of exchange correlation functionals and instead focus on the differences between PBE and the HSE functional. While certainly not exhaustive, previous benchmarking studies in dense hydrogen and helium have indicated that HSE's improved description of exchange can result in large quantitative differences in the forces, charge localization, relative to PBE.

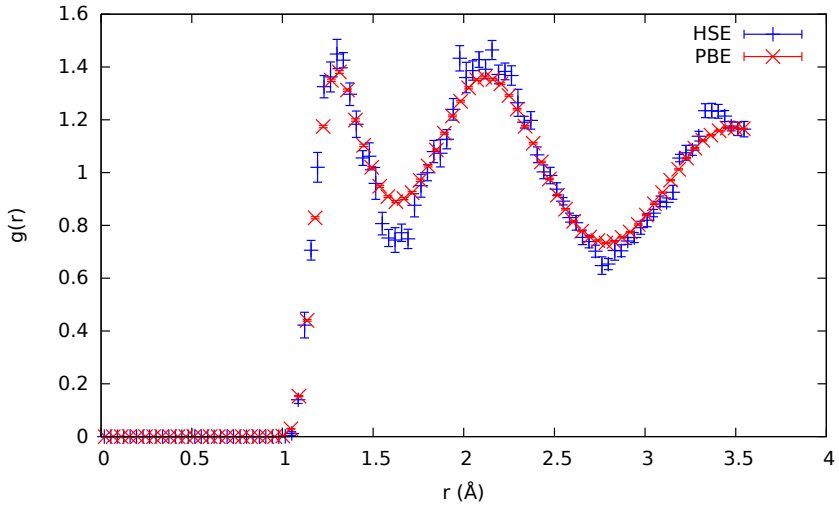

Figure 12.1: The g(r) for liquid lithium at T=1400K and P=500GPa, computed from QMD using both the PBE and HSE functionals.

In Figure 12.1, we compare the pair correlation functions in liquid lithium obtained using the HSE and PBE functionals at T=1400K and P=500GPa. We find that the differences are not qualitatively significant, although there are noticeable quantitative differences between the two functionals. HSE shows enhanced peak amplitude for the first and second coordination shells, followed by a reduction. This indicates that the low coordination clustering behavior previously observed in liquid lithium is enhanced with more accurate treatments of exchange.

In Figure 12.2, we plot the cluster survival probability $P_n(\tau)$ (probability that the $n-1$ nearest neighbors of an arbitrary lithium atom are the same after a time τ) as a function of cluster size n in the liquid phase.

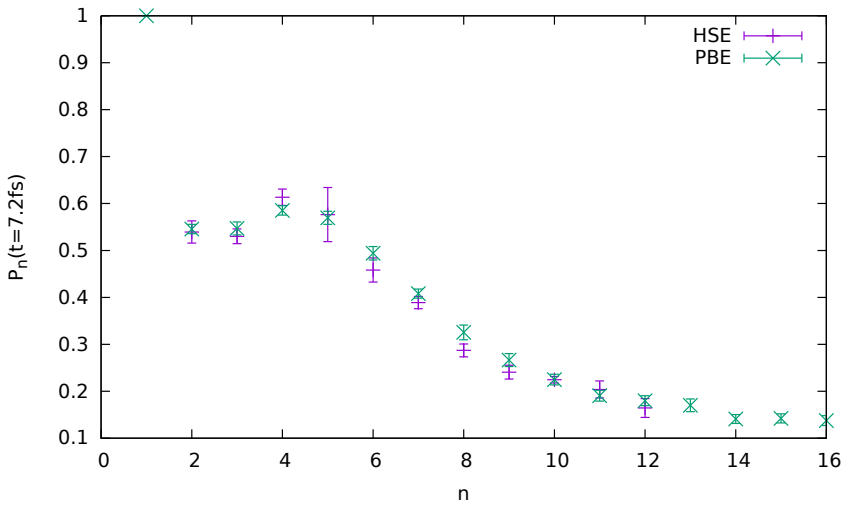

Figure 12.2: Cluster survival probability P_n for clusters of size n at time $t = 7.2fs$. Results for both the HSE and PBE functionals are shown.

We notice that to within error bars, there are no quantitative differences between simulations run using the PBE and HSE functionals. More importantly, the same clustering peak at $n = 4$ is observed, indicating that the tetrahedral clustering behavior is robust to functional choice.

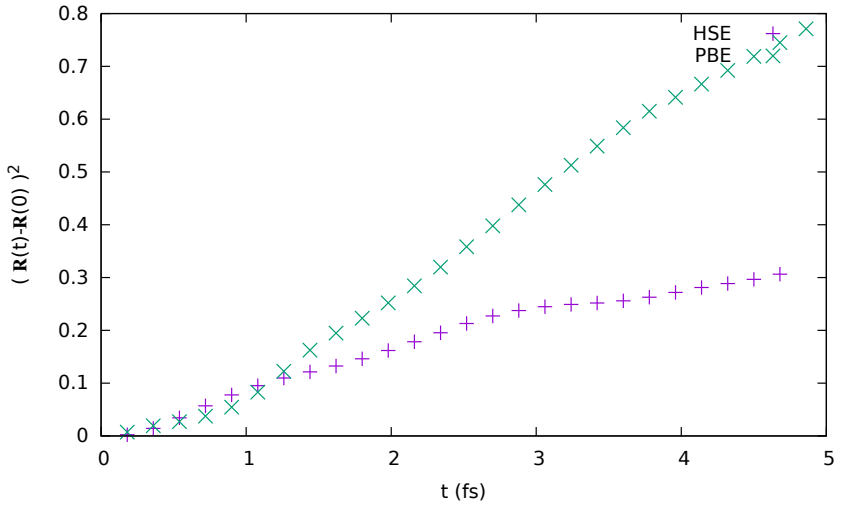

Figure 12.3: Plot of square displacement $(\mathbf{R}(t) - \mathbf{R}(0))^2$ vs. time from QMD using the PBE and HSE functionals.

Lastly in Figure 12.3, we plot the square displacement as a function of time from equilibrated QMD simulations using both the PBE and HSE functionals. By using the HSE functional, we find that the diffusion constant is reduced by a factor or 2 to 3 relative to PBE. This, combined with the changes in the $g(r)$ and the minimal changes in the cluster survival probabilities, seem to suggest that HSE predicts

enhanced bonding between the Li atoms, as the clusters seem to be more tightly arranged with greatly reduced diffusivities. This behavior in lithium would then follow the same trends observed in dense hydrogen and hydrogen-helium mixtures [107, 130], whereby HSE and other functionals that favor enhanced exchange predict stronger bonding than PBE.

12.3.2 Nuclear Quantum Effects

Local Structure

In this section, we discuss the impact that the inclusion of nuclear quantum effects has in changing the local structure of both the solid and liquid phases across a range of temperatures and pressures.

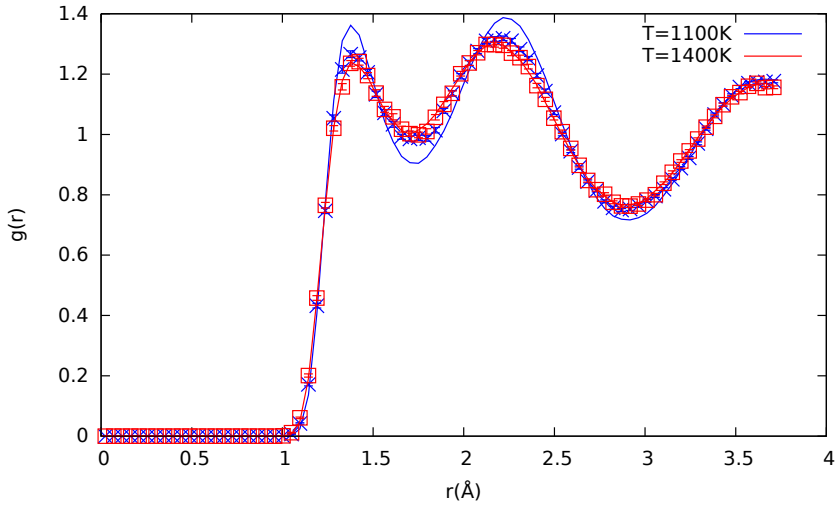

Figure 12.4: Plot of $g(r)$ in liquid ^{7}Li at P=300GPa. Solid lines correspond to classical nuclei, whereas the markers indicate quantum nuclei. Two different temperatures are shown in different colors.

In Figure 12.4, we compare the pair correlation functions obtained using classical nuclei and quantum nuclei in liquid ^{7}Li. The pressure and temperature were chosen to ensure the presence of low coordination clustering. We find that while we can detect differences in the pair correlation function at T=1100K, by T=1400K these differences disappear. What differences observed are largely consistent with the inclusion of zero-point effects: broadening of the peaks and a washing out of local structure compared to classical simulations.

In Figure 12.5, we plot comparisons of the $g(r)$ using classical and quantum nuclei in two proposed dense solid phases: $P4_2mbc$ and $R\bar{3}m$. At T=500K, both structures exhibit a noticeable reduction and broadening of the nearest neighbor peak. However, the $g(r)$ at larger distances seems surprisingly robust to the inclusion of nuclear quantum effects. By T=1100K, the differences between classical and quantum

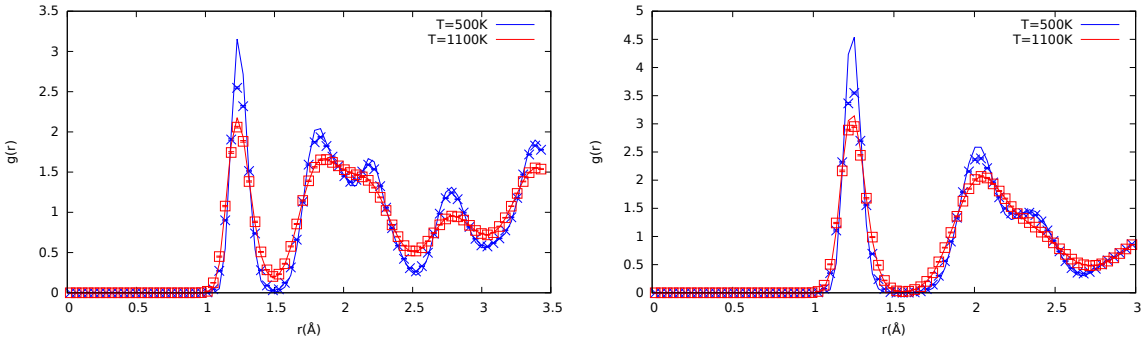

Figure 12.5: Plot of $g(r)$ in solid ^{7}Li at P=500GPa. Solid lines correspond to classical MD, whereas the markers indicate PIMD. (Left) $g(r)$ for the proposed $P4_2mbc$ structure. (Right) $g(r)$ for proposed $R\bar{3}m$ structure.

nuclei are negligible.

Energetics

In this section, we discuss how nuclear quantum effects modify the energy and pressure. In what follows, we define the quantum correction to an observable X as $\Delta X_Q = X_{PIMD} - X_{MD}$.

We begin by considering the energy correction ΔE_Q as a function of pressure for the liquid and several different proposed structures at constant temperature. In Figure 12.6, we show the total energy corrections for three different temperatures: T=500K, 1100K, and 1400K. The corrections are sizeable at 500K, increasing nearly linearly from 1.5mHa/atom at 200GPa to nearly 3mHa/atom at 600GPa. As the temperature is increased to 1100K and 1400K, the magnitude of the energy correction expectedly drops. At T=1100K, the correction increases linearly from 0.5mHa/atom to 2mHa/atom as pressure is varied from 200GPa to 600GPa. By T=1400K, the linear increase in the energy correction subsides, and does not seem to exceed 1mHa at the highest pressures.

In Figure 12.7, we consider the pressure correction from nuclear quantum effects as the pressure is increased. The pressure exhibits the same trends observed in the energy: strong linear increase with pressure at T=500K, reduced linear increase at T=1100K, and then nearly negligible contributions at T=1400K. While nuclear quantum effects contribute amount to at most a 0.5% correction to the total pressure, this yields an enthalpy correction of up to 1.7mHa/atom at T=500K and P=600GPa.

For both the total energy and pressure corrections, we found some sensitivity of the quantum corrections to the structure. For example, corrections to the $P4_2mbc$ structure become measurably larger than for the other solid structures as pressure is increased. Additionally, we see that the quantum correction for the liquid phsae at T=1100K and P=300GPa is noticeably larger than the correction in the solids. To establish

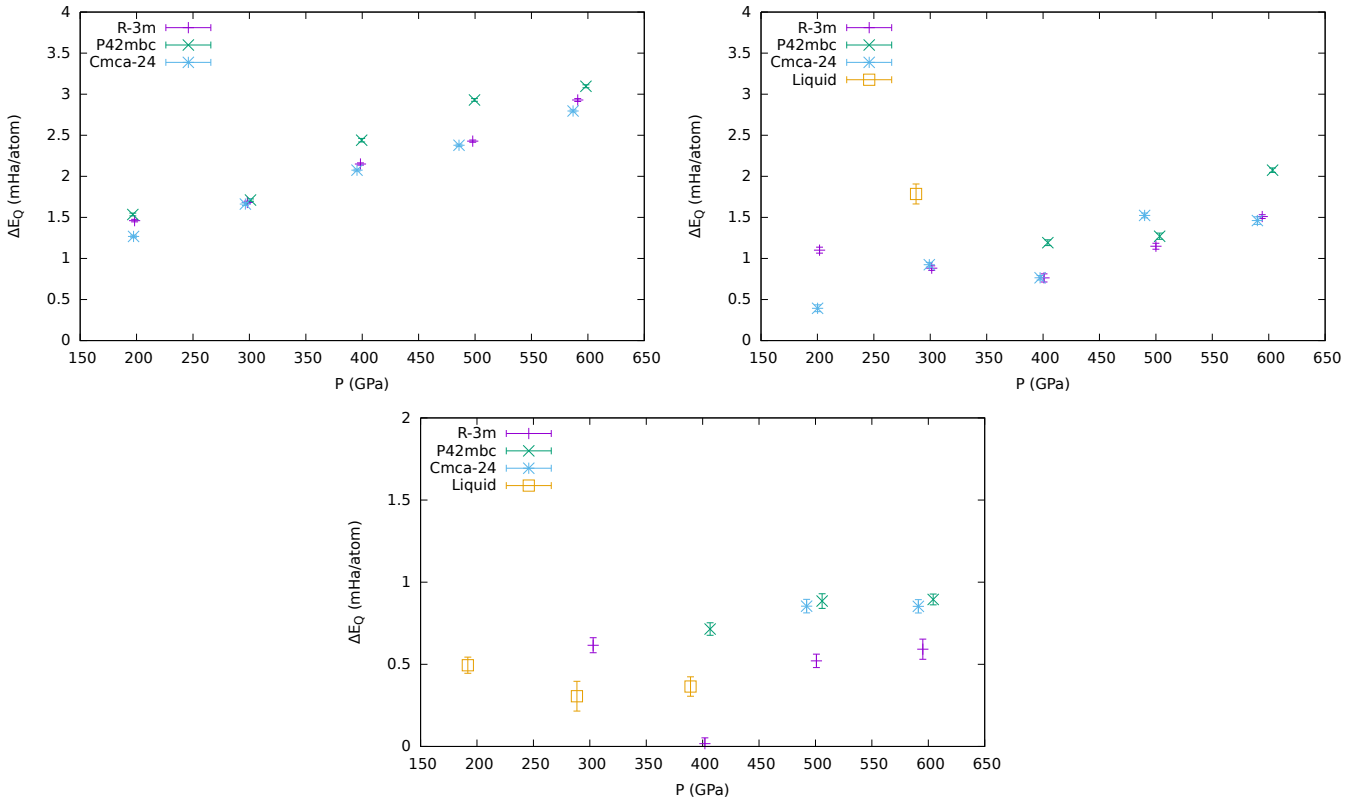

Figure 12.6: Plot of ΔE_Q vs. pressure for (top left) T=500K, (top right) T=1100K, (bottom) T=1400K. The energy correction for three proposed solid structures is shown, as well as the liquid phase when available.

the origin of this discrepancy, we plot the corrections to the nuclear kinetic energy in Figure 12.8. We find that while $P4_2mbc$ seems to acquire a larger correction than other solid structures at higher pressures (see T=500K), the differences between the various solid kinetic energy corrections is much reduced. The corrections are linear as a function of pressure, and when we look at T=1400K, the liquid corrections lie almost on an identical line as the solid corrections. We suspect that slight changes in the local structure of both the liquid and solid phase observed earlier are resulting in larger *potential energy* corrections than the well behaved kinetic energy corrections would suggest.

12.3.3 Scaling with Mass

In the previous sections, we noted the robustness of structural properties to the inclusion of nuclear quantum effects. In this section, we seek to ascertain how much of the observed behavior can be captured by a simple model.

To this end, we attempt to approximate the DFT potential energy surface with a classical pair potential. The functional form was chosen to be an optimizable b-spline with 30 knots and a cutoff radius of $r_{cut} =$

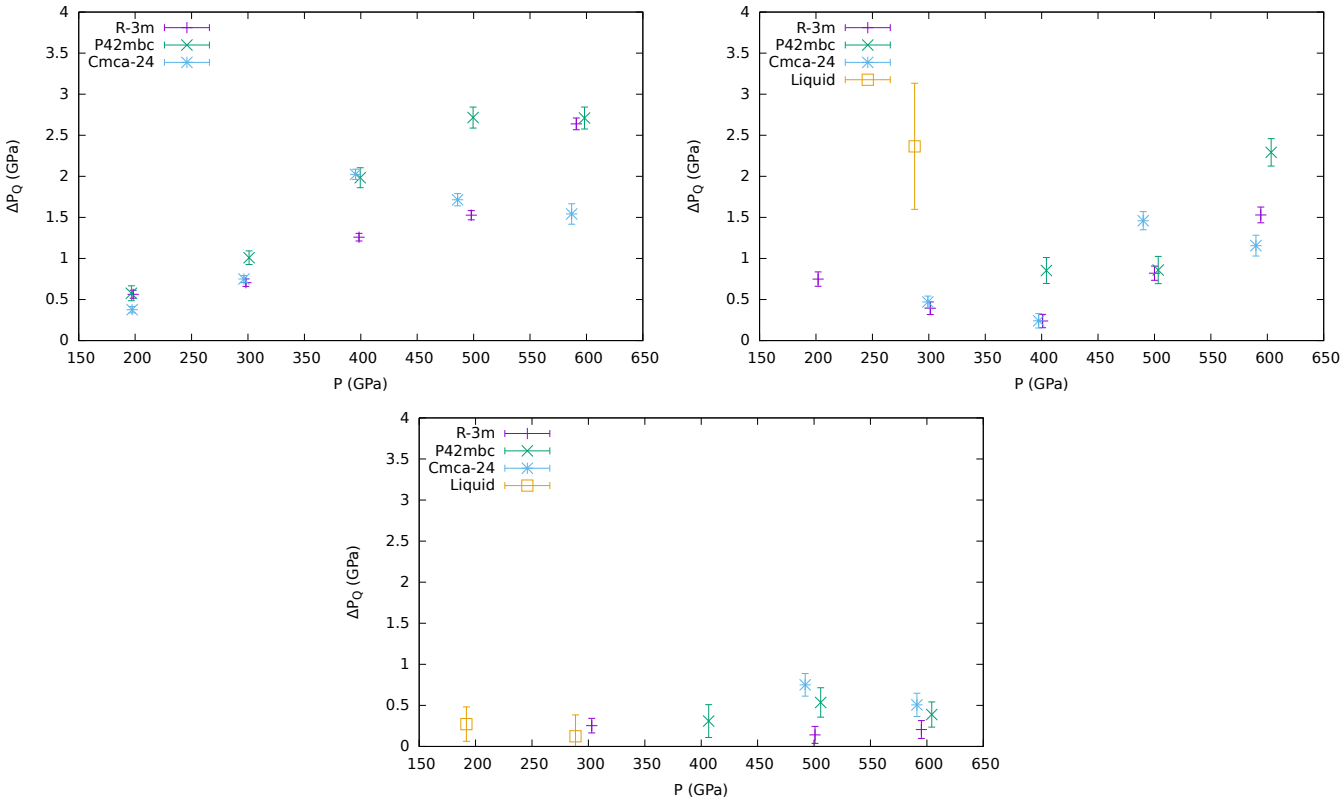

Figure 12.7: Plot of ΔP_Q vs. pressure for (top left) T=500K, (top right) T=1100K, (bottom) T=1400K. The energy correction for three proposed solid structures is shown, as well as the liquid phase when available.

7.46$\mathring{A}$. We used PotFit to perform the force matching procedure [139]. Between 50 and 100 snapshots from the liquid and various solid phases at temperatures ranging between 500K and 2000K were used to conduct the fit. We targeted a pressure of approximately 400GPa with these snapshots. Forces, energies, and stresses were included in the force matching cost function, which was then optimized using stochastic annealing. Running classical simulations in the liquid phase shows that the mean absolute error for the forces are 9 mHa/bohr, with a root-mean-square errors for energies of approximately 0.25mHa/atom. Diffusion constants are approximately 15 times larger than the original DFT simulations.

Qualitatively, this classical potential captures the behavior of the liquid phase reasonably well. In Figure 12.10, we show the $g(r)$ for the classical pair potential against the $g(r)$ calculated using DFT. While the pair correlation functions of the pair potential and DFT disagree at a fixed temperature, we notice that the low coordination liquid structure is qualitatively captured with this classical pair potential. If we compare the $g(r)$ from a pair potential with the $g(r)$ from DFT at 300K higher, we see quantitative agreement between the classical pair potential and DFT.

While the qualitative behavior of the liquid phase is captured with our classical pair potential, it's not

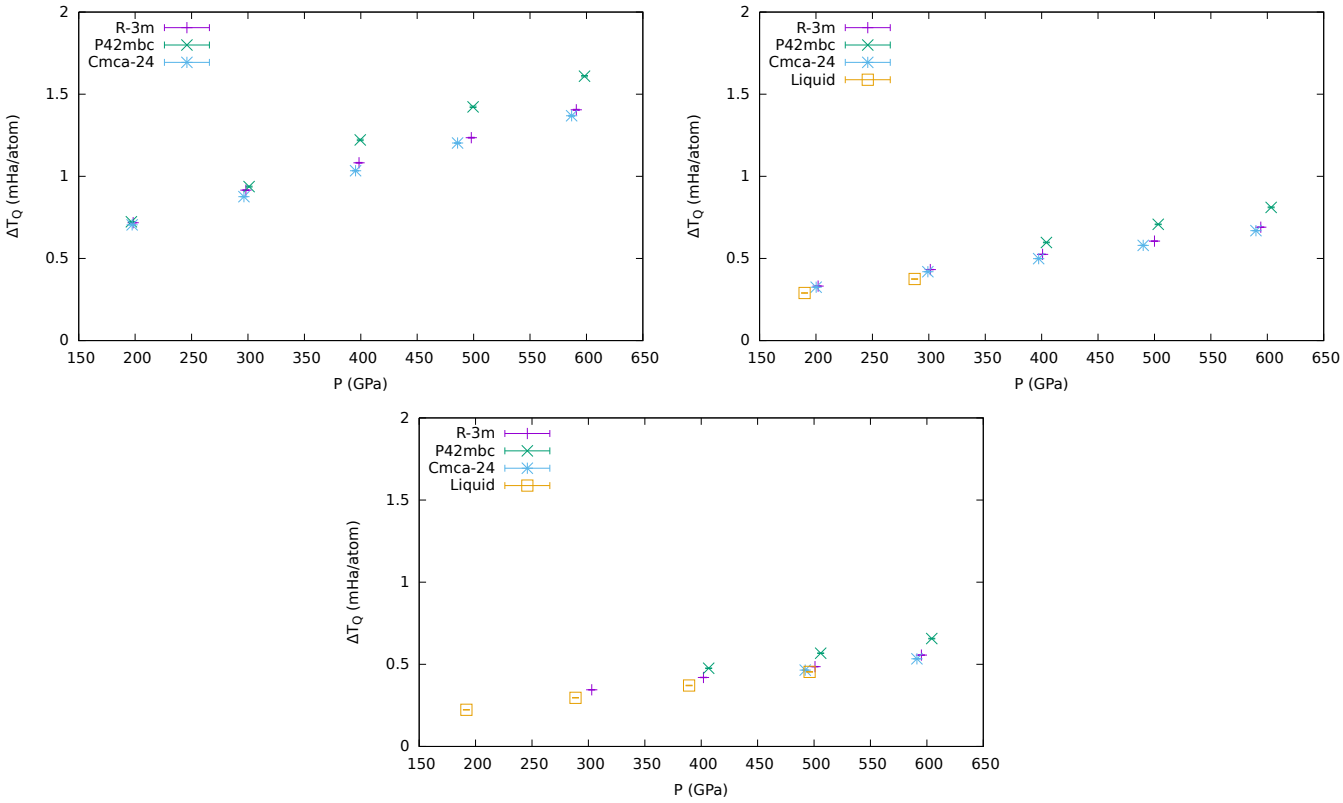

Figure 12.8: Plot of ΔT_Q vs. pressure for (top left) T=500K, (top right) T=1100K, (bottom) T=1400K. The energy correction for three proposed solid structures is shown, as well as the liquid phase when available.

necessarily true that the solid behavior will be reproduced with the same potential. Upon simulating the $Cmca-24$, $P4_2mbc$, $R\bar{3}m$, and $Imma$ phases, only Imma was found to be stable. Upon annealing a snapshot taken from a liquid simulation at the same density (but with the box geometry and number of atoms incommensurate with the $Imma$ unit cell), we found that the liquid configuration relaxed into a solid structure whose short-range local order is very similar to the $Imma$ structure. This is shown in Figure 12.10. While this is not the correct structure at this density according to DFT, it is one of the candidate structures listed by Pickard and Needs. Qualitatively, it is a low coordination phase with 4 nearest neighbors, which in this regard is similar to the lowest enthalpy DFT structures, though it does possess a higher degree of symmetry. Hence, we deem this classical pair potential adequate for understanding the qualitative behavior of lithium in both the liquid and solid phases at this density.

Having constructed a classical potential that qualitatively captures the local structure and dynamics of the liquid, and the structure of the solid, we investigate what happens when we turn on nuclear quantum effects. Using path-integral molecular dynamics with a Langevin thermostat, we ran several simulations in both the liquid and solid phases using several different fictitious nuclear masses. We show the results for

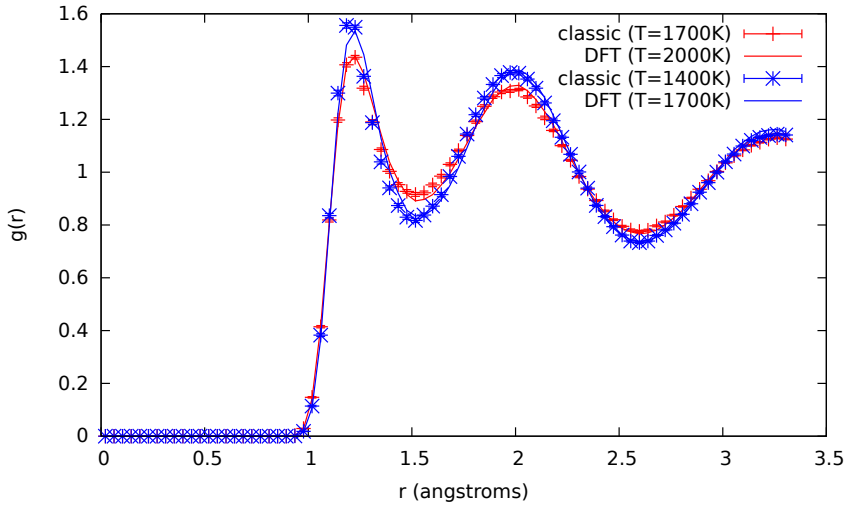

Figure 12.9: Comparisons of $g(r)$ computed using both DFT based molecular dynamics and molecular dynamics with a classical pair potential. The classical potentials are plotted at T=1700K and T=1400K, whereas the $g(r)$ for the DFT MD simulations which most closely match the classical $g(r)$ is plotted.

the $g(r)$ in the liquid and solid phases for several different nuclear masses in Figure 12.11. At T=800K, the nearest neighbor peak drops in amplitude and broadens. In spite of this difference, the structure is qualitatively the same: 4-fold coordination, with the long-range $g(r)$ behavior being largely insensitive to the inclusion of nuclear quantum effects.

Aside from qualitatively impacting the local structure of a material, nuclear quantum effects introduce subtle energetic effects which could affect phase boundaries when constructing an equation of state. Frequently, quantum corrections to the free energy of solids are obtained from the quasi-harmonic approximation, whereby the energetic corrections scale like $1/\sqrt{m}$, with m being the nuclear mass. In liquid molecular hydrogen, the presence of a strong H_2 bond again contributes significantly to the free energy. In dense lithium where clustering behavior is observed, it is not entirely clear to what extent this scaling relation will hold.

In Figure 12.12, we plot the quantum correction to the kinetic energy ΔT_Q as a function of $1/m$ for both the liquid and solid phases. Several temperatures are shown to illustrate how the mass scaling relations depend on temperature. After fitting our results to the functional form $f(m) = am^{-1/2} + bm^{-1}$, we can draw the following conclusions. First, despite the existence of tetrahedral clustering in the liquid phase, the $m^{-1/2}$ scaling predicted by quasi-harmonic based arguments is largely absent in the liquid phase. Secondly, the $m^{-1/2}$ behavior expected in the solid phase is found at low temperatures (less than 400K), but even at 200K there are significant deviations from quasi-harmonic behavior. If the melting temperature of lithium at these densities is above 1000K, we find that nuclear quantum corrections in both the solid and liquid

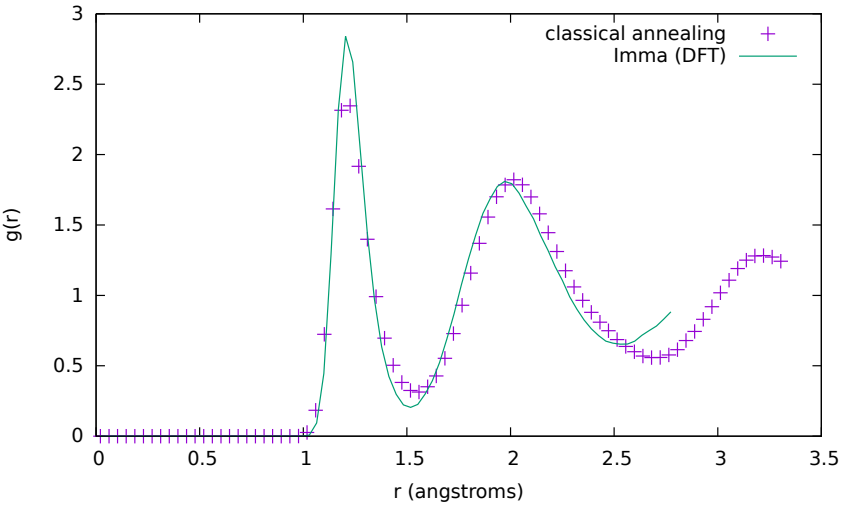

Figure 12.10: Comparisons of $g(r)$ between DFT based $Imma$ structure at T=500K and P=400Gpa and the structure obtained from annealing the classical pair potential.

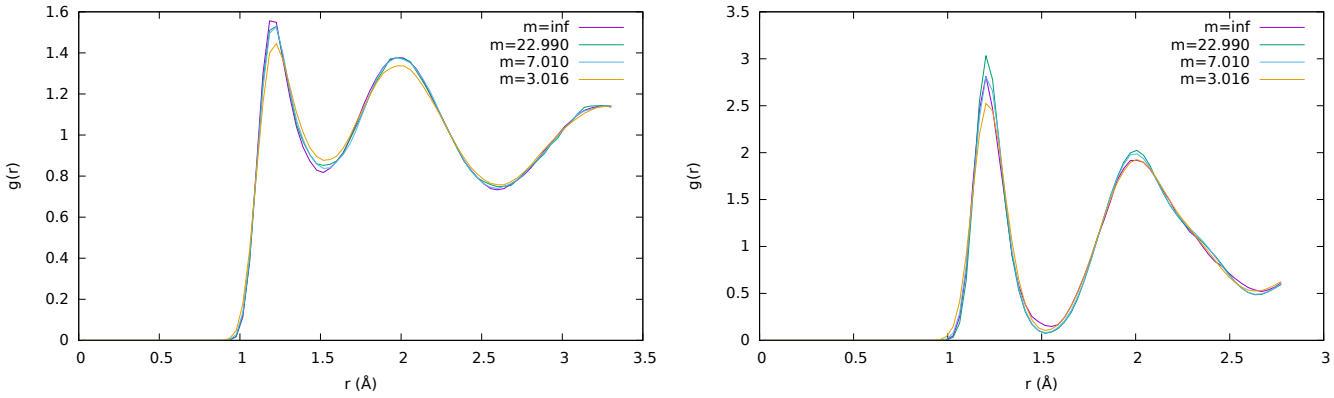

Figure 12.11: (Left) $g(r)$ in dense liquid lithium from PIMD simulations at T=1400K using a classical pair potential and several fictitious ion masses. (Right) $g(r)$ in solid $Imma$ structure at T=800K using several different ion masses.

phase are better fit to a m^{-1} scaling.

12.4 Phase Diagram

After analyzing the role of nuclear quantum effects in both the solid and liquid phases, we are now in a position to start determining the phase diagram. We began by computing the quasi-harmonic phase diagram. We considered the following structures from previous structure searching studies: $Aba2$, $Fd\bar{3}m$, $R\bar{3}m$, $Imma$, $Cmca-24$, and $P4_2mbc$. The names of each phase refer to the Hermann-Mauguin space group designation [140]. While they are somewhat hard to visualize, lithium atoms in these structures

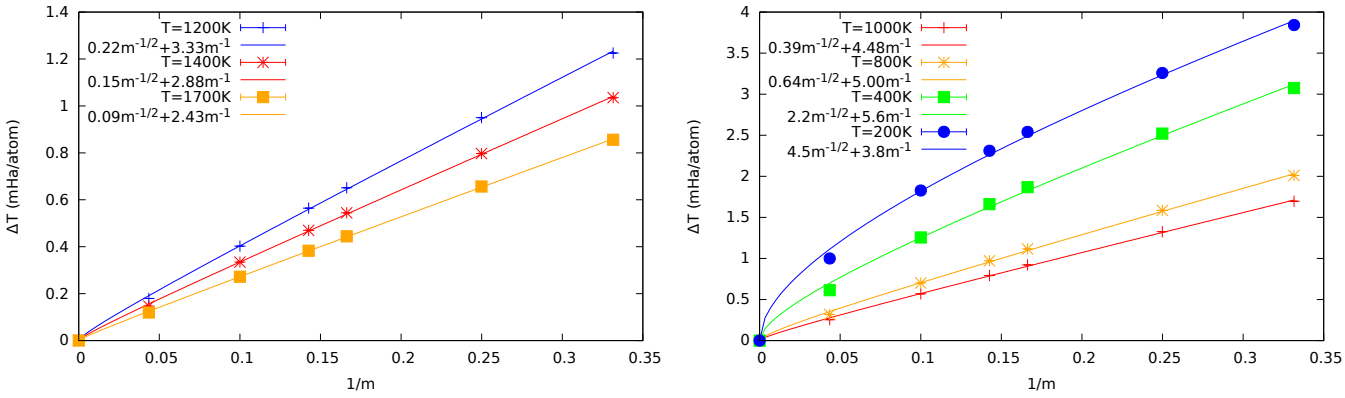

Figure 12.12: $\Delta T_Q = T_Q - T_{Cl}$ vs. $1/m$, where m is the nuclear mass in a.m.u, for (left) liquid lithium at T=1400K, and (right) solid lithium at T=200K. Density is consistent with a pressure of 600GPa.

possess 4-fold coordination. We used the frozen phonon code Phonopy [123] in conjunction with VASP to compute the force-constant matrix. The smallest unit cell we used within the frozen-phonon approach was 1500 for the $Cmca-24$ structure, and the largest was 2058 atoms for the $R\bar{3}m$ structure. We considered larger supercells, but found that these sizes reasonably converged the vibrational spectrum.

In Figure 12.13, we show the phase diagram of lithium within the quasi-harmonic approximation. At low temperatures, identifying the structure with the lowest Gibbs' free energy is reasonably unambiguous. At temperatures at and above T=1000K, we found that the $Cmca-24$ and $P4_2mbc$ structures had nearly degenerate Gibbs' free energies.

We now look to see how the phase diagram changes when we include the liquid phase of lithium and anharmonic effects. We begin by computing the free energy of reference points for the liquid and following solid phases: $Aba2$, $Cmca-24$, $P4_2mbc$, and $R\bar{3}m$. The reference point for the liquid was at T=1400K and P=500GPa, whereas all solid phases were chosen to be at T=500K and P=400GPa. We used the coupling-constant integration method discussed in Chapter 5 to compute the free energies. Then, using the molecular dynamics data from section 12.2, we used thermodynamic integration to compute the free energy at all temperature and volume points on our grid.

From the free energies on our volume/temperature grid, we were able to compute the Gibbs' free energy. Interpolating the volume grid to a pressure grid, we plotted the Gibbs' free energy at fixed pressure $G(T, P_0)$ for all solid and liquid phases. Fitting these to quadratic polynomials, we were able to calculate the temperatures and pressures of the major phase-boundaries including error bars. We show these results without finite-size corrections in Figure 12.14.

We note that the melting line increases sharply from a $Cmca-24$, $P4_2mbc$, liquid triple-point and then flattens out. At around 500GPa, there is a re-emergence of the $Cmca-24$ phase in the form of another

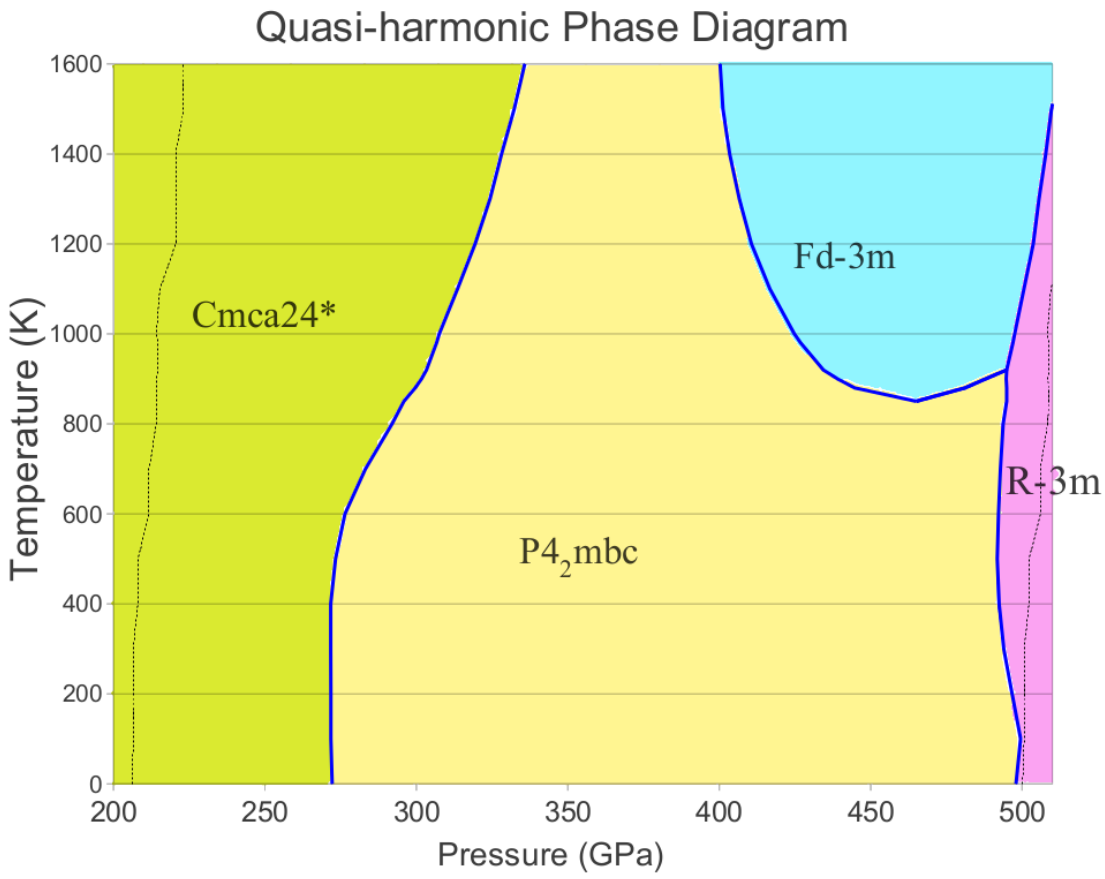

Figure 12.13: Plot of quasi-harmonic phase diagram of lithium. The asterisk indicates that above 1000K, $P4_2mbc$ and $Cmca-24$ have nearly degenerate Gibbs' free energies.

triple point. While we believe that it is unlikely that $Cmca-24$ really appears again at this higher pressure, its low Gibbs free energy in this part of the phase diagram indicates that we should conduct structure searching studies to establish if there are any new phases. Either way, some phase exists there which is more thermodynamically stable than the liquid, indicating that the melting line will continue to have a positive slope.

Regarding the solid-solid phase boundaries, the first differences we see relative to the quasi-harmonic phase diagram are in the slopes of the $Cmca-24/P4_2mbc$ phase boundary between 200GPa and 300GPa and the $R\bar{3}m/P4_2mbc$ phase boundary. Rather than being nearly vertical up to 600K, they have negative and positive slopes respectively. The negative slope of the $Cmca-24/P4_2mbc$ boundary is due to the fact that $P4_2mbc$ has a smaller unit cell. We will have to wait to see if this is robust to the inclusion of finite-size effects, but thermal expansion stemming from the anharmonic effects should be expected to produce

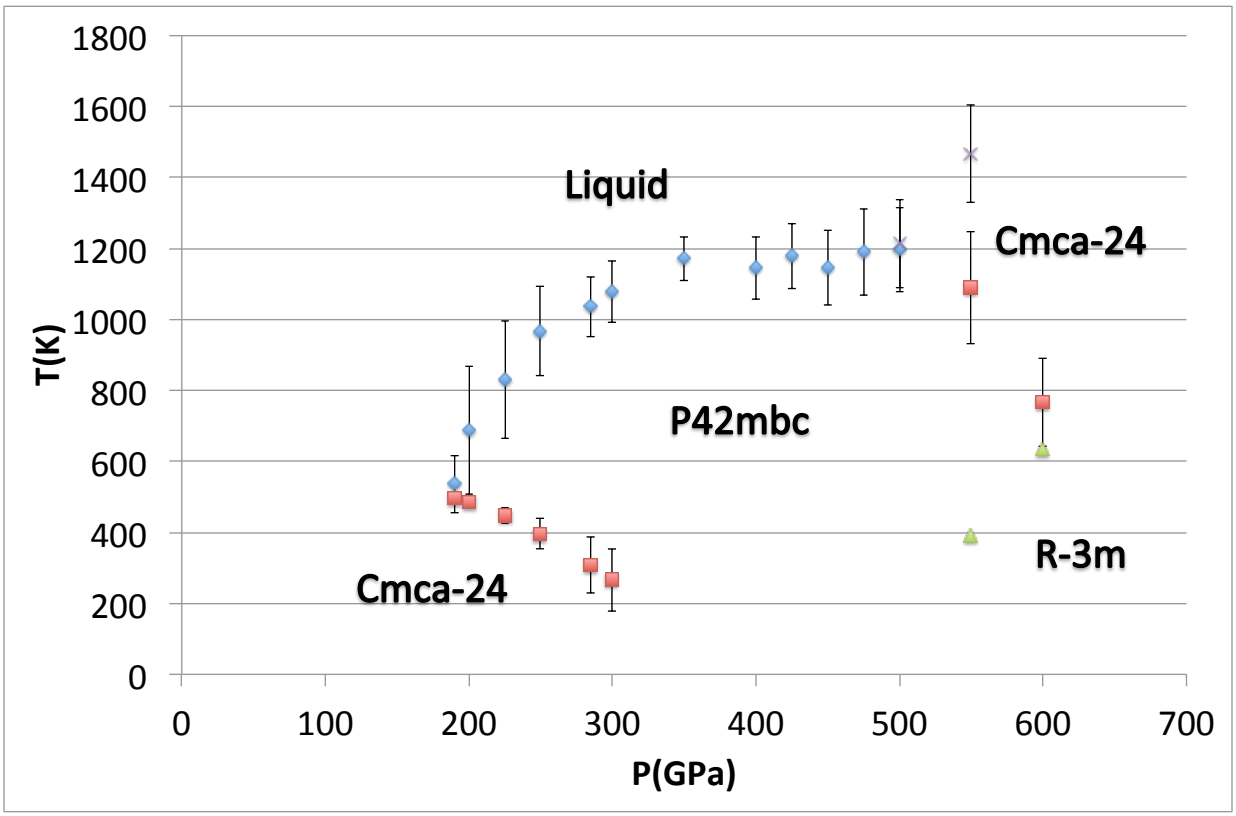

Figure 12.14: Plot of the phase diagram of lithium using classical thermodynamic integration. This phase diagram includes anharmonic effects and a more accurate estimate of the entropy than the quasiharmonic phase diagram.

noticeable deviations from quasi-harmonic results, especially at higher temperatures.

In Figure 12.15, we show the TS contribution to the Gibbs' free energy as a function of pressure at $T = 500K$. From this figure, we can deduce that the positive slope of the $R\bar{3}m$ phase boundary is due mostly to entropic effects. While $R\bar{3}m$ has a noticeably lower enthalpy than all competing structures after 500GPa, the thermodynamic integration results indicate that it also has the smallest entropy contribution. This means that as temperature is increased, $P4_2mbc$ and $Cmca-24$ will be stabilized far more than $R\bar{3}m$.

Our preliminary finite size corrections are not complete enough at the moment to correct this preliminary phase diagram, although what data we do have allows us to make the following qualitative statements. First, comparing the energy corrections for the liquid and $P4_2mbc$ phases suggests that the melting line will be lowered somewhat. Secondly, the $R\bar{3}m$ phase will be stabilized relative to the $P4_2mbc$ phase. This will move the $R\bar{3}m$ phase boundary up and to the left. Lastly $Cmca-24$ will be destabilized at low pressures, and stabilized above 500GPa relative to $P4_2mbc$.

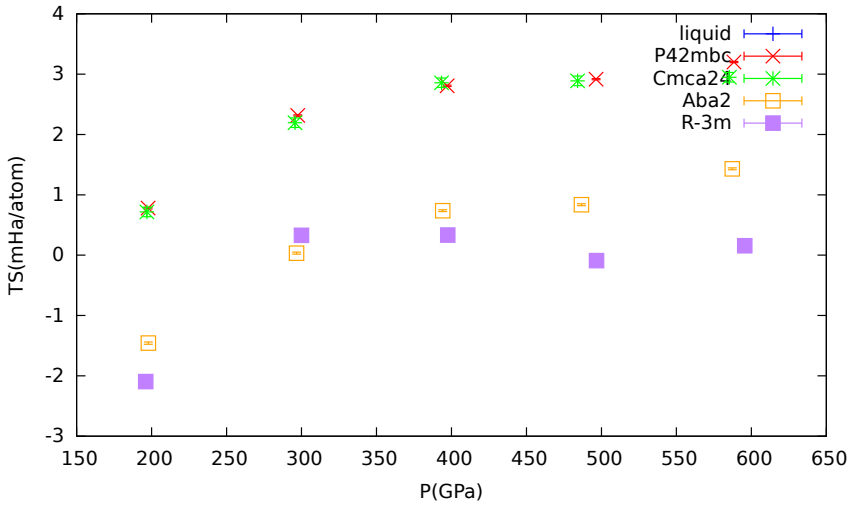

Figure 12.15: Plot of TS versus pressure for considered candidate Li structures at T=500K.

12.5 Future Work

While the work on the impact of nuclear quantum effects on the liquid and solid structures is robust, our prediction of the phase diagram of lithium between 200GPa and 600GPa is at the moment incomplete. Recently, we found a published structure that lies between the $Cmca-24$ and $P4_2mbc$ phases. The new structure has a $Cmca$ space group, but with 56 atoms in the unit cell [141]. Our immediate plan is to perform molecular dynamics simulations on this structure using the same temperature and pressure grid we used throughout this study. In the long run, we would also like to perform our own structure searching studies above 400GPa.

We also need to look at how much nuclear quantum effects change our calculated phase diagram. In the short run, we can use the raw data from our PIMD simulations to construct enthalpy corrections for quantum nuclei. This assumes that the entropy we computed in our classical simulations is a reasonable approximation to the quantum entropy. This is of course emphatically not true at low temperatures, so the correct way to calculate free energies which include nuclear quantum effects is through coupling-constant integration to correct quantum reference systems. For liquid lithium, we would integrate to a system of non-interacting particles in a box. For the solids, we would integrate to quantum Einstein solids.

Chapter 13

Conclusion

At ambient conditions, assessing the errors present in approximate theory has traditionally been done using experimental data. At thermodynamic conditions relevant for planetary physics and inertial confinement fusion, however, the sparsity of experimental data renders this approach largely inapplicable. The major contribution in this thesis is our development of *ab initio* benchmarking, whereby we self-consistently estimate the errors incurred by approximate theories by using more fundamental levels of theory. We described the first large-scale deployments of this method in Chapters 8 and 10, wherein we benchmarked various flavors of density functional theory against highly accurate QMC calculations targeting important transitions in the hydrogen and hydrogen-helium phase diagrams. In Chapters 9 and 11, we discuss how lessons learned from our benchmarking studies can shed light on the atomic-to-molecular transition in dense hydrogen, as well as the immiscibility transition in dense hydrogen-helium mixtures.

Even though our benchmarking work largely focused on identifying which density functionals had the lowest errors for a given application, the large amount of data associated with our test sets opens up the titillating possibility of greatly improving the accuracy of approximate density functionals. Future work will focus on optimizing existing GGA type functionals to reproduce QMC data as closely as possible. Longer term research will focus on constructing many-body corrections to common density functionals, similar in spirit to the Grimme correction [73]. With enough data, it should be possible to identify how well a functional captures two and three-body correlations, and to parameterize these corrections for future applications. While traditional density functional development has shied away from such semi-empirical approaches for fear of ruining the transferability of the density functional, we are freed from this constraint by being able to quantitatively evaluate density functional errors based on more fundamental levels of theory.

While the *ab initio* benchmarking method we laid out is completely general to differing levels of theory, our development and deployment of QMC force and stress estimators greatly increases the utility of QMC specifically, not only for benchmarking, but for other applications as well. These estimators were developed and described in Chapter 6, and a study of the finite-size effects associated with these estimators was performed in Chapter 7. The dramatic reduction in computational cost associated with using force and

stress estimators opens up the use of QMC to a slew of new applications: structure optimization, phonon calculations, and molecular dynamics. In the near future, it should be possible to perform QMC based structure optimization, particularly in low Z materials. This will be an invaluable capability, since for materials at extreme conditions, we need the ability to fall back on more accurate levels of theory in the event that DFT is shown to be inadequate.

The last major contribution of this work is our preliminary prediction of the phase diagram of dense lithium between 200GPa and 600GPa. At the moment, our work here represents the traditional DFT based workflow for computing these phase diagrams, which does not fit neatly within the purview of QMC benchmarking which was the primary focus of this thesis. However, it is necessary to have a qualitative picture of the relevant physics before we can start quantitative investigations. In future studies of dense lithium at these pressure ranges, the work provided in this thesis will provide the starting point for our QMC based benchmarking procedure.

References

[1] Jeremy McMinis, Raymond C. Clay, Donghwa Lee, and Miguel A. Morales. Molecular to Atomic Phase Transition in Hydrogen under High Pressure. *Physical Review Letters*, 114(10):105305, mar 2015.

[2] John Lindl. Development of the indirect-drive approach to inertial confinement fusion and the target physics basis for ignition and gain. *Physics of Plasmas*, 2(11):3933, 1995.

[3] 2015 review of the inertial confinement fusion and high energy density science portfolio: Volume i. Technical Report DOE/NA-0040, Department of Energy, National Nuclear Security Administration, May 2016.

[4] Stephen A. Slutz and Roger A. Vesey. High-Gain Magnetized Inertial Fusion. *Physical Review Letters*, 108(2):025003, 2012.

[5] Jeffrey McMahon, Miguel A. Morales, Carlo Pierleoni, and David M. Ceperley. The properties of hydrogen and helium under extreme conditions. *Reviews of Modern Physics*, 84(4):1607–1653, nov 2012.

[6] Jonathan J. Fortney and W.B. Hubbard. Effects of Helium Phase Separation on the Evolution of Extrasolar Giant Planets. *The Astrophysical Journal*, 608(2):1039–1049, jun 2004.

[7] Luke Shulenburger, Thomas R. Mattsson, and M.P. Desjarlais. Beyond chemical accuracy: The pseudopotential approximation in diffusion Monte Carlo calculations of the HCP to BCC phase transition in beryllium. *arXiv preprint arXiv:1501.03850*, 2015.

[8] Miguel A. Morales, Jeremy McMinis, Bryan K. Clark, Jeongnim Kim, and Gustavo E. Scuseria. Multideterminant Wave Functions in Quantum Monte Carlo. *Journal of Chemical Theory and Computation*, 8(7):2181–2188, jul 2012.

[9] Ross T. Howie, Philip Dalladay-Simpson, and Eugene Gregoryanz. Raman spectroscopy of hot hydrogen above 200 GPa. *Nature Materials*, 14(5):495–499, feb 2015.

[10] E. Wigner and H. B. Huntington. On the Possibility of a Metallic Modification of Hydrogen. *The Journal of Chemical Physics*, 3(12):764, 1935.

[11] N.W. Ashcroft. Metallic Hydrogen: A High-Temperature Superconductor? *Physical Review Letters*, 21(26):1748–1749, dec 1968.

[12] Egor Babaev, Asle Sudbø, and N.W. Ashcroft. A superconductor to superfluid phase transition in liquid metallic hydrogen. *Nature*, 431(7009):666–8, oct 2004.

[13] Mohamed Zaghoo, Ashkan Salamat, and Isaac F. Silvera. Evidence of a first-order phase transition to metallic hydrogen. *Physical Review B*, 93(15):155128, apr 2016.

[14] M.D. Knudson, M.P. Desjarlais, A. Becker, R.W. Lemke, K.R. Cochrane, M.E. Savage, D.E. Bliss, T.R. Mattsson, and R. Redmer. Direct observation of an abrupt insulator-to-metal transition in dense liquid deuterium. *Science*, 384(6242):1455, 2015.

[15] Miguel A. Morales, Jeffrey M. McMahon, Carlo Pierleoni, and David M. Ceperley. Nuclear Quantum Effects and Nonlocal Exchange-Correlation Functionals Applied to Liquid Hydrogen at High Pressure. *Physical Review Letters*, 110(6):065702, February 2013.

[16] Miguel A. Morales, Jeffrey M. McMahon, Carlo Pierleoni, and David M. Ceperley. Towards a predictive first-principles description of solid molecular hydrogen with density functional theory. *Physical Review B*, 87(18):184107, may 2013.

[17] D.J. Stevenson. Thermodynamics and phase separation of dense fully ionized hydrogen-helium fluid mixtures. *Physical Review B*, 12(10):3999–4007, nov 1975.

[18] D.J. Stevenson and E.E. Salpeter. The phase diagram and transport properties for hydrogen-helium fluid planets. *The Astrophysical Journal Supplement Series*, 35:221, October 1977.

[19] Miguel A. Morales, Eric Schwegler, David Ceperley, Carlo Pierleoni, Sebastien Hamel, and Kyle Caspersen. Phase separation in hydrogen-helium mixtures at Mbar pressures. *Proceedings of the National Academy of Sciences of the United States of America*, 106(5):1324–9, February 2009.

[20] Winfried Lorenzen, Bastian Holst, and Ronald Redmer. Demixing of Hydrogen and Helium at Megabar Pressures. *Physical Review Letters*, 102(11):115701, March 2009.

[21] Miguel A. Morales, Sebastien Hamel, Kyle Caspersen, and Eric Schwegler. Hydrogen-helium demixing from first principles: From diamond anvil cells to planetary interiors. *Physical Review B*, 87(17):174105, May 2013.

[22] Jonathan J. Fortney and William B. Hubbard. Phase separation in giant planets: inhomogeneous evolution of Saturn. *Icarus*, 164(1):228–243, jul 2003.

[23] William B. Hubbard, Michele K. Dougherty, Daniel Gautier, and Robert Jacobson. Saturn from Cassini-Huygens. pages 75–81, 2009.

[24] M E Cuneo, Senior Member, M C Herrmann, D B Sinars, S A Slutz, W A Stygar, R A Vesey, A B Sefkow, G A Rochau, G A Chandler, J E Bailey, J L Porter, R D McBride, D C Rovang, M G Mazarakis, E P Yu, D C Lamppa, K J Peterson, C Nakhleh, S B Hansen, A J Lopez, M E Savage, C A Jennings, M R Martin, R W Lemke, B W Atherton, I C Smith, P K Rambo, M Jones, M R Lopez, P J Christenson, M A Sweeney, B Jones, L A McPherson, E Harding, M R Gomez, P F Knapp, T J Awe, R J Leeper, C L Ruiz, G W Cooper, K D Hahn, J McKenney, A C Owen, G R McKee, G T Leifeste, D J Ampleford, E M Waisman, A Harvey-Thompson, R J Kaye, M H Hess, S E Rosenthal, and M K Matzen. Magnetically Driven Implosions for Inertial Confinement Fusion at Sandia National Laboratories. *IEEE Transactions on Plasma Science*, 40(12):3222–3245, 2012.

[25] JB Neaton and NW Ashcroft. Pairing in dense lithium. *Nature*, 498(1991):1997–2000, 1999.

[26] Chris Pickard and Richard Needs. Dense Low-Coordination Phases of Lithium. *Physical Review Letters*, 102(14):146401, apr 2009.

[27] Takahiro Matsuoka and Katsuya Shimizu. Direct observation of a pressure-induced metal-to-semiconductor transition in lithium. *Nature*, 458(7235):186–9, mar 2009.

[28] Isaac Tamblyn, Jean-Yves Raty, and Stanimir Bonev. Tetrahedral Clustering in Molten Lithium under Pressure. *Physical Review Letters*, 101(7):075703, aug 2008.

[29] B.L. Hammond and P.J. Reynolds. *Monte Carlo Methods in Ab Initio Quantum Chemistry*. World Scientific Lecture and Course Notes in Chemistry. World Scientific Publishing Co., 1994.

[30] A. Ma, M. D. Towler, N. D. Drummond, and R. J. Needs. Scheme for adding electronnucleus cusps to gaussian orbitals. *The Journal of Chemical Physics*, 122(22), 2005.

[31] P. Nozieres and D. Pines. *Theory Of Quantum Liquids*. Advanced Books Classics Series. Westview Press, 1999.

[32] D.M. Ceperley. Fermion nodes. *Journal of Statistical Physics*, 63(5):1237–1267, 1991.

[33] Yongkyung Kwon, D. M. Ceperley, and Richard M. Martin. Effects of three-body and backflow correlations in the two-dimensional electron gas. *Physical Review B*, 48:12037–12046, Oct 1993.

[34] Bryan K. Clark, Miguel A. Morales, Jeremy McMinis, Jeongnim Kim, and Gustavo E. Scuseria. Computing the energy of a water molecule using multideterminants: A simple, efficient algorithm. *The Journal of Chemical Physics*, 135(24), 2011.

[35] A. Szabo and N.S. Ostlund. *Modern Quantum Chemistry: Introduction to Advanced Electronic Structure Theory*. Dover Books on Chemistry. Dover Publications, 1989.

[36] D. M. Ceperley. Atomic scale simulations lecture notes. 2013.

[37] C.M. Grinstead and J.L. Snell. *Introduction to Probability*. American Mathematical Society, 2012.

[38] C. J. Umrigar, Julien Toulouse, Claudia Filippi, S. Sorella, and R. G. Hennig. Alleviation of the fermion-sign problem by optimization of many-body wave functions. *Physical Review Letters*, 98:110201, Mar 2007.

[39] Julien Toulouse and C. J. Umrigar. Optimization of quantum monte carlo wave functions by energy minimization. *The Journal of Chemical Physics*, 126(8), 2007.

[40] W.H. Press. *Numerical Recipes 3rd Edition: The Art of Scientific Computing*. Cambridge University Press, 2007.

[41] R.C. Grimm and R.G. Storer. Monte-Carlo solution of Schrödinger's equation. *Journal of Computational Physics*, 7(1):134–156, February 1971.

[42] D.M. Ceperley and M.H. Kalos. Quantum Many-Body Problems. In Kurt Binder, editor, *Monte Carlo methods in statistical physics*, volume 7 of *Topics in Physics*, page 145. Springer Berlin Heidelberg, 1979.

[43] P.J. Reynolds, D.M. Ceperley, B.J. Alder, and W.A. Lester. Fixed-node quantum Monte Carlo for molecules. *The Journal of Chemical Physics*, 77(11):5593–5603, 1982.

[44] J.B. Anderson. A random-walk simulation of the Schrodinger equation: H+3. *The Journal of Chemical Physics*, 63(4):1499, 1975.

[45] Roland Assaraf, Michel Caffarel, and Anatole Khelif. Diffusion Monte Carlo methods with a fixed number of walkers. *Physical Review E*, 61(4):4566–4575, April 2000.

[46] J.T. Krogel and D.M. Ceperley. Population control bias with applications to parallel diffusion monte carlo. In S. Tanaka, S.M. Rothstein, and W.A. Lester, editors, *Advances in Quantum Monte Carlo*, ACS Symposium Series. OUP USA, 2013.

[47] Stefano Baroni and Saverio Moroni. Reptation Quantum Monte Carlo: A Method for Unbiased Ground-State Averages and Imaginary-Time Correlations. *Physical Review Letters*, 82(24):4745–4748, June 1999.

[48] Carlo Pierleoni and David M. Ceperley. Computational methods in coupled electron-ion Monte Carlo simulations. *ChemPhysChem*, 6(9):1872–8, September 2005.

[49] C.J. Umrigar, M.P. Nightingale, and K.J. Runge. A diffusion Monte Carlo algorithm with very small time-step errors. *The Journal of Chemical Physics*, 99(August):2865–2890, 1993.

[50] Francesco Calcavecchia and Markus Holzmann. Fermion sign problem in imaginary-time projection continuum quantum monte carlo with local interaction. *Physical Review E*, 93:043321, Apr 2016.

[51] Matthias Troyer and Uwe-Jens Wiese. Computational Complexity and Fundamental Limitations to Fermionic Quantum Monte Carlo Simulations. *Physical Review Letters*, 94(17):1–4, may 2005.

[52] M.H. Kolodrubetz, J.S. Spencer, B.K. Clark, and W.M.C. Foulkes. The effect of quantization on the full configuration interaction quantum Monte Carlo sign problem. *The Journal of Chemical Physics*, 138(2), 2013.

[53] P. Hohenberg and W. Kohn. Inhomogeneous electron gas. *Physical Review*, 136:B864–B871, Nov 1964.

[54] R.M. Martin. *Electronic Structure: Basic Theory and Practical Methods*. Cambridge University Press, 2004.

[55] W. Kohn and L.J. Sham. Self-consistent equations including exchange and correlation effects. *Physical Review*, 140:A1133–A1138, Nov 1965.

[56] David M. Ceperley and B.J. Alder. Ground state of the electron gas by a stochastic method. *Physical Review Letters*, 45(7):566, 1980.

[57] P.R. Antoniewicz and Leonard Kleinman. Kohn-Sham exchange potential exact to first order in ρ(K)/ρ. *Physical Review B*, 31(10):6779–6781, may 1985.

[58] A.D. Becke. On the large-gradient behavior of the density functional exchange energy. *The Journal of Chemical Physics*, 85(12):7184, 1986.

[59] John Perdew, Lucian Constantin, Espen Sagvolden, and Kieron Burke. Relevance of the Slowly Varying Electron Gas to Atoms, Molecules, and Solids. *Physical Review Letters*, 97(22):223002, nov 2006.

[60] John Perdew, Adrienn Ruzsinszky, Gábor Csonka, Oleg Vydrov, Gustavo Scuseria, Lucian Constantin, Xiaolan Zhou, and Kieron Burke. Restoring the Density-Gradient Expansion for Exchange in Solids and Surfaces. *Physical Review Letters*, 100(13):136406, Apr 2008.

[61] A.D. Becke. Density-functional exchange-energy approximation with correct asymptotic behavior. *Physical Review A*, 38(6):3098–3100, sep 1988.

[62] Yingkai Zhang and Weitao Yang. Comment on Generalized Gradient Approximation Made Simple. *Physical Review Letters*, 80(4):890–890, jan 1998.

[63] Elliott H Lieb and Stephen Oxford. Improved Lower Bound on the Indirect Coulomb Energy*. XIX:427–439, 1981.

[64] Garnet Kin-lic Chan and Nicholas C. Handy. Optimized Lieb-Oxford bound for the exchange-correlation energy. *Physical Review Letters*, 59(4):3075–3077, 1999.

[65] J.P. Perdew, K. Burke, and M. Ernzerhof. Generalized Gradient Approximation Made Simple. *Physical Review Letters*, 77(18):3865–3868, oct 1996.

[66] B. Hammer, L. Hansen, and J. Nørskov. Improved adsorption energetics within density-functional theory using revised Perdew-Burke-Ernzerhof functionals. *Physical Review B*, 59(11):7413–7421, 1999.

[67] Axel D. Becke. Density-functional thermochemistry. III. The role of exact exchange. *The Journal of Chemical Physics*, 98(7):5648, 1993.

[68] John P. Perdew, Matthias Ernzerhof, and Kieron Burke. Rationale for mixing exact exchange with density functional approximations. *The Journal of Chemical Physics*, 105(22):9982, 1996.

[69] Chengteh Lee, Weitao Yang, and Robert G. Parr. Development of the Colle-Salvetti correlation-energy formula into a functional of the electron density. *Physical Review B*, 37(2):785–789, jan 1988.

[70] Jeng Da Chai and Martin Head-Gordon. Systematic optimization of long-range corrected hybrid density functionals. *Journal of Chemical Physics*, 128(8), 2008.

[71] Jochen Heyd, Gustavo E. Scuseria, and Matthias Ernzerhof. Hybrid functionals based on a screened Coulomb potential. *The Journal of Chemical Physics*, 118(18):8207, 2003.

[72] Alexandre Tkatchenko and Matthias Scheffler. Accurate Molecular Van Der Waals Interactions from Ground-State Electron Density and Free-Atom Reference Data. *Physical Review Letters*, 102(7):073005, feb 2009.

[73] Stefan Grimme. Semiempirical GGA-type density functional constructed with a long-range dispersion correction. *Journal of Computational Chemistry*, 27(15):1787–99, nov 2006.

[74] M. Dion, H. Rydberg, E. Schröder, D.C. Langreth, and B.I. Lundqvist. Van der Waals Density Functional for General Geometries. *Physical Review Letters*, 92(24):246401, jun 2004.

[75] Kyuho Lee, Éamonn D. Murray, Lingzhu Kong, Bengt I. Lundqvist, and David C. Langreth. Higher-accuracy van der Waals density functional. *Physical Review B*, 82(8):081101, aug 2010.

[76] Kristian Berland and Per Hyldgaard. Exchange functional that tests the robustness of the plasmon description of the van der Waals density functional. *Physical Review B*, 89(3):035412, jan 2014.

[77] Valentino R. Cooper. Van der Waals density functional: An appropriate exchange functional. *Physical Review B*, 81(16):161104, apr 2010.

[78] Jií Klimeš, David R Bowler, and Angelos Michaelides. Chemical accuracy for the van der Waals density functional. *Journal of Physics. Condensed matter : an Institute of Physics journal*, 22(2):022201, jan 2010.

[79] David M. Ceperley. Path integrals in the theory of condensed helium. *Reviews of Modern Physics*, 67(2):279–355, apr 1995.

[80] J. Cao and B.J. Berne. A BornOppenheimer approximation for path integrals with an application to electron solvation in polarizable fluids. *The Journal of Chemical Physics*, 99(4):2902, 1993.

[81] Carlo Pierleoni and David M. Ceperley. The Coupled Electron-Ion Monte Carlo Method (Lect. Notes), 2006.

[82] M.P. Allen and D.J. Tildesley. *Computer simulation of liquids*. Oxford science publications. Clarendon Press, 1987.

[83] D. Frenkel and B. Smit. *Understanding Molecular Simulation: From Algorithms to Applications*. Computational science series. Elsevier Science, 2001.

[84] Giovanni Bussi and Michele Parrinello. Accurate sampling using Langevin dynamics. *Physical Review E*, 75(5):056707, may 2007.

[85] Michele Ceriotti, Giovanni Bussi, and Michele Parrinello. Langevin equation with colored noise for constant-temperature molecular dynamics simulations. *Physical Review Letters*, 102(2):1–4, 2009.

[86] Michele Ceriotti, Michele Parrinello, Thomas E. Markland, and David E. Manolopoulos. Efficient stochastic thermostatting of path integral molecular dynamics. *The Journal of Chemical Physics*, 133(12):124104, 2010.

[87] Glenn J. Martyna, Michael L. Klein, and Mark Tuckerman. NoseHoover chains: The canonical ensemble via continuous dynamics. *The Journal of Chemical Physics*, 97(4):2635, 1992.

[88] Enrico Fermi, J. Pasta, and S. Ulam. Studies of non linear problems. Technical Report LA-1940, Los Alamos National Laboratory, 1955.

[89] F. Ercolessi and J.B. Adams. Interatomic Potentials from First-Principles Calculations: The Force-Matching Method. *Europhysics Letters (EPL)*, 26(8):583–588, jun 1994.

[90] D.L. Beveridge and F.M. DiCapua. Free Energy Via Molecular Simulation: Applications to Chemical and Biomolecular Systems. *Annual Review of Biophysics and Biophysical Chemistry*, 18(1):431–492, jun 1989.

[91] Carlos Vega and Eva G. Noya. Revisiting the Frenkel-Ladd method to compute the free energy of solids: The Einstein molecule approach. *The Journal of Chemical Physics*, 127(15):154113, 2007.

[92] K.P. Esler. *ADVANCEMENTS IN THE PATH INTEGRAL MONTE CARLO METHOD FOR MANY-BODY QUANTUM SYSTEMS AT FINITE TEMPERATURE*. ProQuest, 2006.

[93] R.P. Feynman. Forces in Molecules. *Physical Review*, 56(4):340–343, aug 1939.

[94] Simone Chiesa, D. Ceperley, and Shiwei Zhang. Accurate, Efficient, and Simple Forces Computed with Quantum Monte Carlo Methods. *Physical Review Letters*, 94(3):036404, jan 2005.

[95] O.H. Nielsen and R.M. Martin. Quantum-mechanical theory of stress and force. *Physical Review B*, 32(6):3780–3791, sep 1985.

[96] V Natoli and D.M. Ceperley. An optimized method for treating long-range potentials. *Journal of Computational Physics*, 1995.

[97] Roland Assaraf and Michel Caffarel. Zero-Variance Principle for Monte Carlo Algorithms. *Physical Review Letters*, 83(23):4682–4685, dec 1999.

[98] Jeremy McMinis. *Benchmark Studies Using Quantum Monte Carlo: Pressure Estimators, Energy, and Entanglement*. PhD thesis, University of Illinois at Urbana-Champaign, 2013.

[99] C. Lin, F. Zong, and D.M Ceperley. Twist-averaged boundary conditions in continuum quantum Monte Carlo algorithms. *Physical Review E*, 64(1):016702, jun 2001.

[100] Simone Chiesa, David Ceperley, Richard Martin, and Markus Holzmann. Finite-Size Error in Many-Body Simulations with Long-Range Interactions. *Physical Review Letters*, 97(7):6–9, August 2006.

[101] Markus Holzmann, Raymond C. Clay, Miguel A. Morales, Norm M. Tubman, David M. Ceperley, and Carlo Pierleoni. Theory of finite size effects for electronic quantum Monte Carlo calculations of liquids and solids. *Physical Review B*, 94(3):035126, jul 2016.

[102] Markus Holzmann, Bernard Bernu, Valerio Olevano, Richard M. Martin, and David M. Ceperley. Renormalization factor and effective mass of the two-dimensional electron gas. *Physical Review B*, 79(4):2–5, jan 2009.

[103] N Troullier and José Luriaas Martins. Efficient pseudopotentials for plane-wave calculations. *Physical Review B*, 43(3):1993–2006, January 1991.

[104] Hendra Kwee, Shiwei Zhang, and Henry Krakauer. Finite-size correction in many-body electronic structure calculations. *Physical Review Letters*, 100:126404, Mar 2008.

[105] Louisa Fraser, W. Foulkes, G. Rajagopal, R. Needs, S. Kenny, and A. Williamson. Finite-size effects and Coulomb interactions in quantum Monte Carlo calculations for homogeneous systems with periodic boundary conditions. *Physical Review B*, 53(4):1814–1832, January 1996.

[106] N. Drummond, R. Needs, A. Sorouri, and W. Foulkes. Finite-size errors in continuum quantum Monte Carlo calculations. *Physical Review B*, 78(12):125106, September 2008.

[107] Raymond C. Clay, Jeremy Mcminis, Jeffrey M. McMahon, Carlo Pierleoni, David M. Ceperley, and Miguel A. Morales. Benchmarking exchange-correlation functionals for hydrogen at high pressures using quantum Monte Carlo. *Physical Review B*, 89(18):184106, may 2014.

[108] Carlo Pierleoni, Miguel A Morales, Giovanni Rillo, Markus Holzmann, and David M Ceperley. Liquid–liquid phase transition in hydrogen by coupled electron–ion monte carlo simulations. *Proceedings of the National Academy of Sciences*, 113(18):4953–4957, 2016.

[109] Paolo Giannozzi, Stefano Baroni, Nicola Bonini, Matteo Calandra, Roberto Car, Carlo Cavazzoni, Davide Ceresoli, Guido L Chiarotti, Matteo Cococcioni, Ismaila Dabo, Andrea Dal Corso, Stefano de Gironcoli, Stefano Fabris, Guido Fratesi, Ralph Gebauer, Uwe Gerstmann, Christos Gougoussis, Anton Kokalj, Michele Lazzeri, Layla Martin-Samos, Nicola Marzari, Francesco Mauri, Riccardo Mazzarello, Stefano Paolini, Alfredo Pasquarello, Lorenzo Paulatto, Carlo Sbraccia, Sandro Scandolo, Gabriele Sclauzero, Ari P Seitsonen, Alexander Smogunov, Paolo Umari, and Renata M Wentzcovitch. QUANTUM ESPRESSO: a modular and open-source software project for quantum simulations of materials. *Journal of physics. Condensed matter : an Institute of Physics journal*, 21(39):395502, September 2009.

[110] N Troullier and José Luriaas Martins. Efficient pseudopotentials for plane-wave calculations. *Physical Review B*, 43(3):1993–2006, jan 1991.

[111] G. Kresse and J. Hafner. Ab initio molecular dynamics for liquid metals. *Physical Review B*, 47(1):558–561, January 1993.

[112] G Kresse and J. Furthmüller. Efficiency of ab-initio total energy calculations for metals and semiconductors using a plane-wave basis set. *Computational Materials Science*, 6(1):15–50, July 1996.

[113] Jií Klimeš, David R Bowler, and Angelos Michaelides. Chemical accuracy for the van der Waals density functional. *Journal of physics. Condensed matter : an Institute of Physics journal*, 22(2):022201, January 2010.

[114] Alexandre Tkatchenko and Matthias Scheffler. Accurate Molecular Van Der Waals Interactions from Ground-State Electron Density and Free-Atom Reference Data. *Physical Review Letters*, 102(7):073005, February 2009.

[115] Xin-Zheng Li, Brent Walker, Matthew I J Probert, Chris J Pickard, Richard J Needs, and Angelos Michaelides. Classical and quantum ordering of protons in cold solid hydrogen under megabar pressures. *Journal of physics. Condensed matter : an Institute of Physics journal*, 25(8):085402, February 2013.

[116] Chris J. Pickard, Miguel Martinez-Canales, and Richard J. Needs. Density functional theory study of phase IV of solid hydrogen. *Physical Review B*, 85(21):214114, June 2012.

[117] Chris J. Pickard and Richard J. Needs. Structure of phase III of solid hydrogen. *Nature Physics*, 3(7):473–476, May 2007.

[118] Sam Azadi, W.M.C. Foulkes, and Thomas D. Kühne. Quantum Monte Carlo study of high pressure solid molecular hydrogen. *New Journal of Physics*, 15(11):113005, November 2013.

[119] Miguel A. Morales, Carlo Pierleoni, and David M. Ceperley. Equation of state of metallic hydrogen from coupled electron-ion Monte Carlo simulations. *Physical Review E*, 81(2):1–9, February 2010.

[120] Elisa Liberatore, Miguel A. Morales, David M. Ceperley, and Carlo Pierleoni. Free energy methods in coupled electron ion Monte Carlo. *Molecular Physics*, 109(23-24):3029–3036, December 2011.

[121] C. Pierleoni and D. M. Ceperley. The Coupled Electron-Ion Monte Carlo Method. In Mauro Ferrario, Giovanni Ciccotti, and Kurt Binder, editors, *Computer Simulations in Condensed Matter Systems: From Materials to Chemical Biology Volume 1 SE - 18*, volume 703 of *Lecture Notes in Physics*, pages 641–683. Springer Berlin Heidelberg, 2006.

[122] Jeffrey M. McMahon and David M. Ceperley. Ground-State Structures of Atomic Metallic Hydrogen. *Physical Review Letters*, 106(16):165302, April 2011.

[123] A Togo and I Tanaka. First principles phonon calculations in materials science. *Scr. Mater.*, 108:1–5, Nov 2015.

[124] Sam Azadi, W.M.C. Foulkes, and Thomas D. Kühne. Quantum Monte Carlo study of high pressure solid molecular hydrogen. *New Journal of Physics*, 15(11):113005, November 2013.

[125] Bartomeu Monserrat, N.D. Drummond, Chris J. Pickard, and R.J. Needs. Electron-Phonon Coupling and the Metallization of Solid Helium at Terapascal Pressures. *Physical Review Letters*, 112(5):055504, feb 2014.

[126] Paul Loubeyre, Florent Occelli, and René LeToullec. Optical studies of solid hydrogen to 320 GPa and evidence for black hydrogen. *Nature*, 416(6881):613–7, apr 2002.

[127] Ranga Dias, Ori Noked, and Isaac F Silvera. New low temperature phase in dense hydrogen: The phase diagram to 421 GPa. *arXiv preprint arXiv:1603.02162*, mar 2016.

[128] M.I. Eremets and I.A. Troyan. Conductive dense hydrogen. *Nature Materials*, 10(12):927–931, nov 2011.

[129] W. J. Nellis, Arthur L. Ruoff, and Isaac F. Silvera. Has Metallic Hydrogen Been Made in a Diamond Anvil Cell? *arXiv preprint arXiv:1201.0407*, page 8, jan 2012.

[130] Raymond C. Clay, Markus Holzmann, David M. Ceperley, and Miguel A. Morales. Benchmarking density functionals for hydrogen-helium mixtures with quantum Monte Carlo: Energetics, pressures, and forces. *Physical Review B*, 93(3):1–12, 2016.

[131] Jií Klimeš, David R. Bowler, and Angelos Michaelides. Van der Waals density functionals applied to solids. *Physical Review B*, 83(19):195131, May 2011.

[132] Jianmin Tao, John P. Perdew, Viktor N. Staroverov, and Gustavo E. Scuseria. Climbing the density functional ladder: nonempirical meta-generalized gradient approximation designed for molecules and solids. *Physical Review Letters*, 91(October):146401, 2003.

[133] Yan Zhao and Donald G. Truhlar. A new local density functional for main-group thermochemistry, transition metal bonding, thermochemical kinetics, and noncovalent interactions. *The Journal of Chemical Physics*, 125(19):194101, November 2006.

[134] David L. Beveridge and F.M. DiCapua. Free Energy Via Molecular Simulation: Applications to Chemical and Biomolecular Systems. *Annual Review of Biophysics and Biophysical Chemistry*, 18(1):431–492, jun 1989.

[135] H.J.C. Berendsen, J.P.M. Postma, W.F. van Gunsteren, A. DiNola, and J.R. Haak. Molecular dynamics with coupling to an external bath. *The Journal of Chemical Physics*, 81(8):3684, 1984.

[136] Winfried Lorenzen, Bastian Holst, and Ronald Redmer. Metallization in hydrogen-helium mixtures. *Physical Review B*, 84(23):235109, December 2011.

[137] Ji Chen, Xin-Zheng Li, Qianfan Zhang, M.I.J Probert, C.J. Pickard, R.J. Needs, A. Michaelides, and E. Wang. Quantum simulation of low-temperature metallic liquid hydrogen. *Nature Communications*, 4(May):2064, 2013.

[138] Yansun Yao, John S. Tse, Zhe Song, and Dennis D. Klug. Core effects on the energetics of solid Li at high pressure. *Physical Review B*, 79(9):092103, mar 2009.

[139] Peter Brommer, Alexander Kiselev, Daniel Schopf, Philipp Beck, Johannes Roth, and Hans-Rainer Trebin. Classical interaction potentials for diverse materials from ab initio data: a review of potfit. *Modelling and Simulation in Materials Science and Engineering*, 23(7):074002, oct 2015.

[140] D.E. Sands. *Introduction to Crystallography*. Dover Books on Chemistry. Dover Publications, 2012.

[141] Jian Lv, Yanchao Wang, Li Zhu, and Yanming Ma. Predicted Novel High-Pressure Phases of Lithium. *Physical Review Letters*, 106(1):015503, jan 2011.